Characterization and Optimization of High-order Harmonics after Adaptive Pulse Shaping

Dissertation zur Erlangung des naturwissenschaftlichen Doktorgrades der Julius-Maximilians-Universität Würzburg

vorgelegt von

Jan Lohbreier

aus Wuppertal

Würzburg 2008

Eingereicht am 6. Juni 2008
bei der Fakultät für Physik und Astronomie

Gutachter der Dissertation:
1. Gutachter: Prof. Dr. C. Spielmann
2. Gutachter: Prof. Dr. J. Geurts

Prüfer im Promotionskolloquium:
1. Prüfer: Prof. Dr. C. Spielmann
2. Prüfer: Prof. Dr. J. Geurts
3. Prüfer: Prof. Dr. C. Honerkamp

Tag der mündlichen Prüfung (Promotionskolloquium): 18. Juli 2008

Doktorurkunde ausgehändigt am: _____

List of publications

Journal articles

C.Winterfeldt, J.Lohbreier, A.Paulus, T.Pfeifer, R.Spitzenpfeil, D.Walter, G.Gerber, and C.Spielmann
Adaptive spatial control of high-harmonic generation
in Ultrafast Phenomena XV, (eds. R.J.D. Miller, A.M. Weiner, P.Corkum, D.Jonas) (Springer, Berlin, 2006), Springer Series in Chemical Physics

D.Walter, S.Eyring, J.Lohbreier, R.Spitzenpfeil, and C.Spielmann
Spatial Optimization of Filaments
Appl. Phys. B **88**, 2, (2007)

D.Walter, S.Eyring, J.Lohbreier, R.Spitzenpfeil, and C.Spielmann
Two-dimensional evolutionary algorithm designed for high resolutions
(in preparation)

J.Lohbreier, S.Eyring, R.Spitzenpfeil, C.Kern, M.Weger, and C.Spielmann
Maximizing the brilliance of high-order harmonics in a gas jet
(submitted)

Conference contributions

J.Lohbreier, S. Formica, N.Mail, and C.MacDonald
Diffraction and Fluorescence Measurements with Polycapillary X-ray Optics
DPG-Spring Conference, Berlin, Germany, (2005)

J.Lohbreier, S.Eyring, A.Paulus, R.Spitzenpfeil, D.Walter, C.Winterfeldt, and C.Spielmann
High-order harmonics from shaped 10-fs laser pulses
Super-Intense Laser-Atom Interaction (SILAP) Conference, Salamanca, Spain (2006)

J.Lohbreier, S.Eyring, R.Spitzenpfeil, D.Walter, M.Weger, and C.Spielmann
Optimization of high-order harmonics by spatial shaping before the filament
DPG-Spring Conference, Duesseldorf, Germany, (2007)

J.Lohbreier, S.Eyring, R.Spitzenpfeil, and C.Spielmann
Adaptive Shaping of High-order harmonics
Atto 07, International Conference on Attosecond Physics, Dresden, Germany (2007)

J.Lohbreier, S.Eyring, R.Spitzenpfeil, and C.Spielmann
Optimization and Characterization of high-order harmonics by spatial shaping before the filament
Meeting of the SPP 1345, Munich, Germany, (2007)

J.Lohbreier, S.Eyring, C.Kern, R.Spitzenpfeil, D.Walter, and C.Spielmann
Specially parameterized evolutionary algorithm for spatial optimization
DPG-Spring Conference, Darmstadt, Germany, (2008)

Contents

Introduction

When looking scientifically at matter, sooner or later the question of resolution arises. By resolution we normally think of the smallest distance at which points can be distinctly detected. This is a very physical description but also transferred to our everyday language looking at a certain problem usually requires a specific resolution. If you want to distinguish the differences between cars, houses, faces and even opinions, you have to have a 'ruler' with a scale that allows measurement and thus comparison. And every scale we use to judge our daily problems before we tackle them has an intrinsic resolution. The better the resolution the more defined do we see the details of a certain topic - be it real or virtual.

Back to the physical aspects of resolution we mostly deal with temporal and spatial resolution. This is because we live in a three-dimensional space and have a one-dimensional time-axis which clearly orders our life. As argued before, a high resolution is always an advantage but a high 'resolution of cars' does not help when it comes to buying a house. So even better than having a high resolution in only one aspect it is more useful to look at different topics with an equally high resolution. Switching back to physics - because the resolution of car-buying or house-pricing is not scientific at all - it is enough to regard space and time. With time being one dimensional and space three dimensional that results in a four dimensional resolution problem. And we want the highest resolution possible - in every dimension.

The problems with the temporal and spatial resolution are for once the different units. While one millimeter is easy to distinguish from two millimeters and one second from two seconds, it gets a little complicated when comparing for example 2 seconds with 2 millimeters. Fortunately more than 100 years ago a fundamental relation between time and space was given by A. Einstein - with the drawback that it only holds for light. Since the fastest processes and measurements in the universe involve light as well this is a restriction that one can comply with. Now using light and looking at experiments a little closer another fundamental relation is quickly discovered: The shorter the wavelength of light (the higher the photon energy) the better the spatial resolution. Since this does not include an upper limit, it is necessary to realize that according to Heisenberg's uncertainty principle when 'measuring' with such a high energy, the result is always a sum of the experiment itself and the effect of the light. This means that the light interacts in a non-predictable way with the matter and even with vacuum. Thus using the shortest possible wavelengths comes along with a disadvantage by strongly interfering with the experiment. Additionally, Heisenberg also pointed out another interesting fact: The more accurately the wavelength of the light is measured, the less one can say about its temporal structure. Translated into everyday language this implies that a light beam with only one distinct wavelength can not be defined by beginning and end. And beginning and end is normally measured in time. So there is a link between the resolution of space - being defined by the wavelength - and the resolution of time - being defined by how exact we know the

wavelength.
Now coming to the end of this introduction one should keep in mind that there is no such thing as an endlessly high spatial and temporal resolution in the same experiment. What is demonstrated in this work and has long before been shown by scientists [1, 2] is one approach to a compromise of resolution in space and time at the same moment. This is based on the technique of high-order harmonics generation (HHG) which provides an unparalleled high temporal and a very high spatial resolution. The challenge of this radiation is the measurement of its temporal and spatial properties and exactly this characterization and optimization of high-order harmonics is the topic of this thesis.
In the first chapter the basic theoretical foundations of the physics of near-infrared (NIR) laser light will be described. Here the mathematical description of laser pulses and nonlinear optics is given as well as ways to generate, measure and change these pulses. Chapter 2 deals with different ways to further compress laser pulses in the time domain and introduces their optimization via an evolutionary algorithm in the space and time domain. In the third chapter, these short laser pulses are then used for the process of high-order harmonic generation which resembles the up-conversion of the fundamental laser pulse. The last part of this work shows methods to optimize this harmonic generation process and characterize the generated radiation in terms of spatial and temporal distribution.

Chapter 1

Laser Pulses and Nonlinear Optics

Since in this whole work ultrashort laser pulses are the main workhorse, their characteristics will be described briefly in this chapter. Laser radiation is known since the early 1960s after mainly the workgroup of Townes and Schawlow at the Bell Labs and Gould at the Columbia University worked on an "optical maser". The first coherent light source with very good beam quality was build on the basis of a solid-state flashlamp-pumped synthetic ruby crystal laser by Maiman at the Hughes Research Lab in 1960. Since then the laser of course has come a far way and today there are not only solid-state lasers but also gas-lasers and semi-conductor lasers which all have different purposes and advantages. Because the focus of this work is on ultrashort laser pulses some technical details involved in generating laser pulses are given here. As already mentioned in the introduction, Heisenberg formulated a relation between the temporal and energetic uncertainty which can be written as:

$$\tau_p \Delta\omega = 2\pi c_b \tag{1.1}$$

Here τ equals the pulse duration and $\Delta\omega$ is the spectral bandwidth corresponding to the temporal and energy uncertainty, respectively. c_b is a constant that depends on the envelope functions of the electric field of the laser pulse. It is ≈ 0.441 [3] for a Gaussian shaped field-envelope. This equation gives the shortest possible pulse duration for a given spectrum and is also called the Fourier-limited pulse duration. As shown later this is an often desired but hard-to-achieve condition.
One major difference between continuous wave (cw) lasers and pulsed lasers can be directly inferred from Equation 1.1: a pulsed laser system has to include various wavelengths that are amplified while a cw laser is nearly monochromatic. Since the mid 1960s locking of the different modes of a pulsed laser was introduced as a technique to gain very short laser pulses. More detailed information on mode-locking and other methods present in a state-of-the-art laser system will be given in 1.3.3. Regardless of their ways of operation, pulsed and cw lasers emit electromagnetic waves which will be described analytically in the following section.

1.1 Mathematical Description

Electromagnetic waves and their dynamics can be described as solutions of Maxwell's equations [4]:

$$\nabla \cdot E = \frac{\rho}{\epsilon_0} \tag{1.2}$$

$$\nabla \cdot B = 0 \tag{1.3}$$

$$\nabla \times E = -\frac{\partial B}{\partial t} \tag{1.4}$$

$$\nabla \times H = J + \frac{\partial D}{\partial t} \tag{1.5}$$

where E is the electric field, B is the magnetic flux density, H is the magnetic field, and D is the electric flux density. From these equations one can derive the general wave equation

$$\left(\frac{\partial^2}{\partial x^2} + \frac{\partial^2}{\partial y^2} + \frac{\partial^2}{\partial z^2}\right) \vec{E}(x,y,z,t) = \frac{1}{c} \cdot \frac{\partial^2}{\partial t^2}\ \vec{E}(x,y,z,t). \tag{1.6}$$

Here E is the electric field of a given wave and c is the speed of light. This differential equation holds for electromagnetic waves that travel through vacuum. For a wave propagating in a medium, the polarization P(x,y,z,t) must be added on the right side of the equation. To find a solution for vacuum, one can get away without $P(x,y,z,t)$ for simplicity reasons. Furthermore, we neglect the dependence of E on x and y - assuming a plane wave - and thus compute

$$E(z,t) = E_0\ cos(k_z z - \omega(k_z)t) = E_0\ cos(\phi(t)) \tag{1.7}$$

with k_z equaling the wave vector $\vec{k}$ in direction z, ω being the angular frequency of the field, and E_0 its amplitude. Using $\phi(t)$ is just a more convenient way of writing the phase of the electromagnetic wave according to $\phi = k_z z - \omega(k_z)t = n(t)\frac{\omega}{c}z - \omega(k_z)t$. Since the electric field is a measurable quantity, $E(t)$ is a real function. Such a monochromatic wave is endless in terms of duration because the amplitude does not change in time. What is needed for a laser pulse is an $E_0(t)$ that in this work will be referred to as the field envelope. Also, most characterization methods of electromagnetic waves (see sections 1.3.1) do not allow the exact measurement of the electric field of a pulse but only its $E_0(t)$. Transformed with the Euler equations the electric field can be written as

$$E(t) = E_0(t)cos(\phi(t)) = \frac{1}{2}E_0(t)\left(e^{i\phi(t)} + e^{-i\phi(t)}\right) \tag{1.8}$$

$$= E^+(t) + E^-(t) = 2Re(E^+(t)) \tag{1.9}$$

$$= E_0(t)e^{i\phi(t)} \tag{1.10}$$

To obtain the frequency dependent electric field $E(\omega)$ one can perform a Fourier transformation on 1.10 and gets an equivalent description of the pulse in the frequency domain. When using ω in this work the angular frequency is meant and ν stands for the real optical frequency. The relation between $E(\omega)$ and $E(t)$ is given by

$$E(\omega) = \frac{1}{\sqrt{2\pi}} \int_{-\infty}^{+\infty} E(t)e^{i\omega t}dt\ \ \wedge\ \ E(t) = \frac{1}{\sqrt{2\pi}} \int_{-\infty}^{+\infty} E(\omega)e^{-i\omega t}d\omega \tag{1.11}$$

$I(\omega)$ and $I(t)$ are considered spectral and temporal intensity of a laser pulse, respectively. From 1.11 one can see that a laser pulse can be completely characterized if the phase and intensity in one domain is known. For example, when the spectrum of a laser pulse is measured experimentally, the detector sees only the spectral intensity

$$I(\omega) \propto \mid E(\omega) \mid^2 \tag{1.12}$$

To measure the spectral phase of a pulse different methods, which will be described in section 1.3, are necessary. The temporal intensity can also be measured but this $I(t)$ then is the squared mean electric field over one optical cycle (one wavelength) which only holds for long enough pulses. This so-called Slowly-Varying Envelope Approximation (SVEA) [3] is not valid for pulses in the few-cycle regime where the pulse duration is in the regime of only a few optical cycles (one optical cycle for 800nm = 2.7fs). In this work only laser pulses longer than 10fs (roughly 4 optical cycles) are generated for experiments so this approximation can safely be used.
Even for ultra-broad bandwidth pulses, the duration of the optical cycle of the central wavelength marks the shortest possible pulse. For an 800nm-laser-system, pulses shorter than $\approx 2.7fs$ are not possible, unless one uses frequency conversion. Another practical examination leads to the additional condition, that the electric field of a laser pulse has to satisfy

$$\int_{-\infty}^{+\infty} E(t)dt = 0 \tag{1.13}$$

in order to have a physical meaning and be reasonable solution to 1.6.

1.2 Nonlinear Optics

In this section the difference between the 'normal' linear optics and nonlinear optics is described. Polarization is the reaction of matter to an incident electromagnetic field. As long as the electronic shell of the atoms is still bound to the nucleus and even the most outward valence electrons still rest in a parabolic potential the response of matter to the wave is linear $P = \epsilon_0 \chi E$. But as soon as the atoms are ionized or the atomic potential becomes distorted, the polarization gets additional terms that depend on higher orders of the electric field.

$$P(t) \propto \chi^{(1)} E(t) + \chi^{(2)} E(t)^2 + \chi^{(3)} E(t)^3 + \cdots \tag{1.14}$$

Here the χs represent the n-th order susceptibilities of the medium and the proportionality factor is the dielectric constant ϵ_0 (and ϵ_r in non-vacuum). Basically, there are various nonlinear effects that are caused by a specific χ^i and in [5] is a listing of applications and techniques based on these nonlinearities. For this work there are some very important mechanisms that are based mainly on the second (Pockels and Faraday effect) and third order (self-focusing and self-phase modulation) susceptibilities. Another way of writing the E-field dependence is to regard the index of refraction written with the Taylor expansion

$$n(I) = n_0 + n_2 I(t) + n_4 I^2(t) + \cdots \tag{1.15}$$

where n_i are the coefficients. Typically, the higher order terms of the index of refraction are relatively small so that their effect is only present when strong electric fields (high intensities) are used. Considering n_2 in terms of nonlinear polarization, it can be written as:

$$n_2 = \frac{3\chi^{(3)}}{4\epsilon_0 c n_0^2} \tag{1.16}$$

with $\chi^{(3)}$ being the third-order susceptibility and ϵ_0 being the vacuum dielectric constant.

1.2.1 Self-focusing

A well-known phenomenon of high-intensity lasers is self-focusing that takes place whenever a laser pulse propagates through dispersive media. In addition to ordinary dispersion, where the index of refraction depends on the wavelength, using high-intensity laser pulses one also sees a dependence of the refractive index on the local intensity. Regarding the spatial distribution as described in 1.2.5, a radially symmetric Gaussian intensity distribution causes different indices of refraction for different parts of the beam. This leads to a lens-like influence on the beam divergence. The self-focusing is based on the nonlinear optical Kerr effect which can be described with the following equation:

$$\Delta n(\vec{r}, t) = n_2 E^2(\vec{r}, t) \propto n_2 I(\vec{r}, t) \tag{1.17}$$

where Δn is the the change of the index of refraction depending on the local electric field. By inserting the proportionality factors in 1.16, one gets an n_2 for an 800nm laser in air of $n_2 = 3.2 \times 10^{-19} cm^2/W$ [6].
When the intensity of the beam is higher in the central part and decreases to the sides and the laser pulse is travelling through a normally dispersive material (n_2 is positive for almost all media), the laser will see a focusing lens. Knowing the laser parameters, a critical power P_{crit} can be defined above which the laser beam will start to self-focus [7].

$$P_{crit} = \frac{\lambda_0^2}{2\pi n_0 n_2} \approx 3.2 GW \tag{1.18}$$

Here $\lambda_0 = 800nm$ and n_0 and n_2 are taken for air. One can enhance the self-focusing by inserting an ordinary focusing device in the beam line to increase intensity and thus the self-focusing. Thus the region of the focus can be controlled better than in open air experiments.

1.2.2 Filamentation

If the laser pulse undergoes self-focusing and a focus in air is generated, the gas molecules are ionized and a weakly ionized plasma is created (see Fig. 1.1).

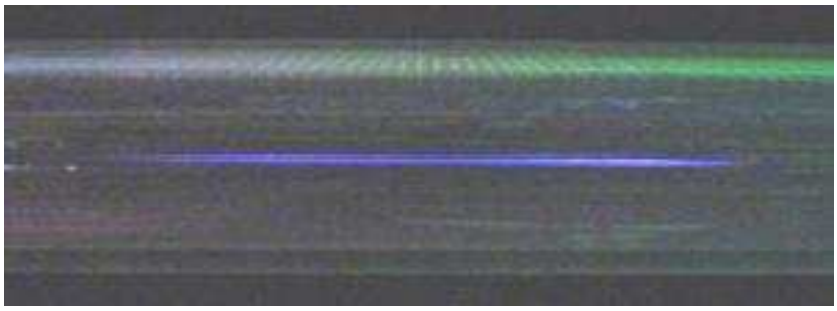

Figure 1.1: Image of a typical 20cm-filament in our gas-filled Plexiglas tube is shown. The visible radiation comes from recombination of the ionized gas.

This plasma has a much higher free electron density than the surrounding medium and the free electron density is the highest in the central part of the focus decreasing radially with intensity. The free electron density is connected to the index of refraction by [8]

$$\Delta n = -N(I)/N_{crit} \sim 10^{-4} \tag{1.19}$$

where $N(I)$ is the intensity dependent free electron density and N_{crit} is the critical density above which the plasma becomes opaque. More details on plasma dispersion can be found in section 3.2.1. As one can see, the plasma-induced change of the refractive index is always negative as opposed to the change of the index of refraction due to the Kerr effect (see Fig. 1.2). Under certain conditions, it may happen that these two mechanisms

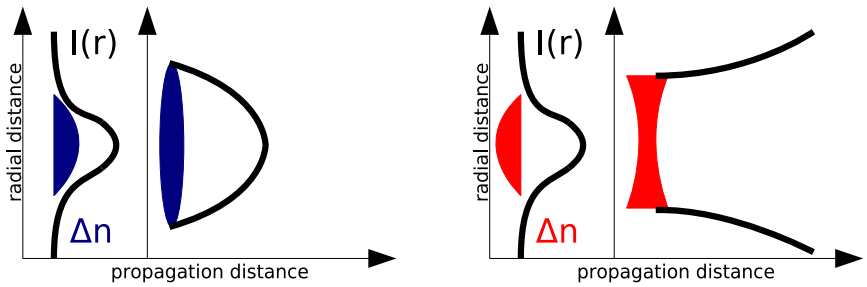

Figure 1.2: left: The effect of self-focusing is demonstrated here. The Gaussian beam profile I(t) causes a higher refractive index where the intensity is higher thus causing a lens-like focusing. right: Due to the lower index of refraction in the center part of the beam, the plasma acts like a defocusing lens and the beam diverges.

counterbalance so that a laser pulses is focused by the Kerr effect and then defocused by the created plasma and then again focused. Under certain conditions, this long array of foci forms a so-called filament that might exceed the length of the Rayleigh range by several orders of magnitude (see Fig 1.1). In this counterbalance region the laser beam travels in a plasma channel that has a diameter of about $100\mu m$ and a very low divergence after the channel. Filamentation thus provides a technique to have the laser pulse interact with a gaseous medium [9] or solid [10] or liquid [11, 12] in a very well collimated way.

What is not so clear to date is the role of the background reservoir for the filamentation process [13]. It seems that a large part of the energy of the laser pulse is propagating along with the plasma channel and provides the necessary energetic flux while only a small fraction is actually in the hot core of the filament [14, 13]. Technically more important is that the energy throughput of a filament is above 90% which makes it a very attractive nonlinear medium as will be described in more detail in Chapter 2.
Since a single plasma channel can only be stable for a certain amount of energy, for very high laser powers of more than $\approx 3-5 \times P_{crit}$ multifilamentation takes place (see Fig 1.3 and section 2.3). In this case, minor inhomogeneities in the beam profile are amplified while propagating in the nonlinear medium and multiple parallel foci form multiple filaments. This can be partially controlled for example by changing the beam parameters [15, 16] or controlling the wave front [17]. Our laser system mainly operates in the single filament regime and the gas pressure is adjusted likewise. As will be shown in Chapter 4, the beam profile of a laser pulse after filamentation can be somewhat distorted and multiple filaments produce an even worse beam profile for our experimental setup. When such a long focus is created, one also sees conical emission [18] which describes the fact that different wavelengths have different divergences. In our IR-regime and with frequency-broadened spectra this leads to a bluish outer part of the beam profile and a white inner part (see Fig 1.3).

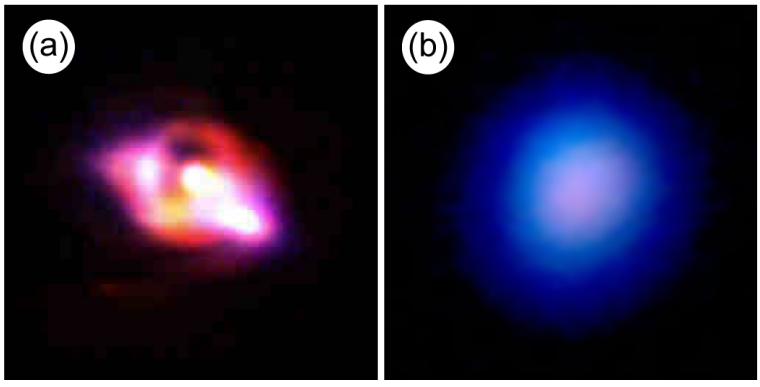

Figure 1.3: Beam profiles recorded with a color CCD camera including an IR-filter. Both pictures show the laser after exiting the gas tube. In (a) intensity inhomogeneities and spatial chirp occur due to multifilamentation within the gaseous medium. In the single filament (b) regime there is a homogeneous beam profile with a radial intensity distribution. Also clearly visible is the white light in the inner part and the bluish outer part due to conical emission.

1.2.3 Self-phase modulation

In equation 1.2.1 we already saw that the index of refraction depends not only on the wavelength but also on intensity. Now analog to the spatial intensity distribution, the temporal intensity distribution has a similar impact on the refractive index. Like in equation 1.2.1 we will assume a Gaussian-shaped temporal intensity distribution of the laser pulse (see Fig 1.4). This results in a rise of the index of refraction at the leading edge of the pulse and a lowering of the index of refraction at the trailing edge of the pulse. Thinking of the phase velocity $v_{phase} = c/n$ one sees that v_{phase} is decreasing at the leading edge of the pulses and increasing at the trailing edge. A smaller phase velocity causes longer wavelengths whereas the larger phase velocity has the opposite effect. This means that a Gaussian-shaped laser pulse will have a redshifted 'front' and a blueshifted 'rear' part as shown in Fig. 1.4.
Since these two additional frequencies are generated at the same time (meaning in one pulse) one can measure a broadened spectrum. Because the phase of the laser pulse described in 1.10 is changing in dependence of the temporal intensity, this process is called self-phase modulation (SPM). And as was mentioned in the introduction, a broader spectrum allows shorter pulses and thus SPM is a basic principle to decrease the pulse duration.
Treating SPM mathematically, we can Taylor-expand the temporal phase $\phi(t)$ from section 1.1 and get

$$\phi(t) = \sum_{i=0}^{\infty} \frac{a_i}{i!} t^i = \phi_0 + \phi_1 t + \frac{\phi_2 t^2}{2} + \frac{\phi_3 t^3}{6} + \cdots \tag{1.20}$$

Everything written here for $\phi(t)$ is equally valid for $\phi(\omega)$ since these two are linked via the Fourier transform (see 1.11). From the definition of the instantaneous frequency $\omega = d\phi(t)/dt$ and $\phi(t) = \omega(k_z)t - n(t)\frac{\omega}{c}z$ one can compute with 1.15 and 1.20

$$\omega(t) = \omega_0 - \frac{dn(t)}{dt}\frac{\omega}{c}z = \omega_0 - n_2\frac{dI(t)}{dt}\frac{\omega}{c}z \tag{1.21}$$

where ω_0 is the central frequency, $\omega/c = \vec{k}$ is the wave vector, z the direction of propagation, and $I(t)$ the time-dependent intensity of the laser pulse.

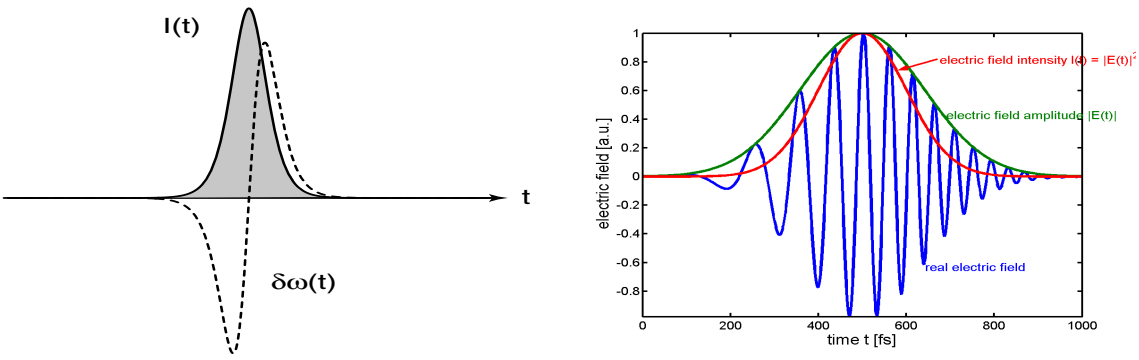

Figure 1.4: On the left the temporal intensity is plotted (grey shaded) with the changing contribution of n_2 (dashed). On the right is an up-chirped pulse (from [19]) and one can see that detecting only the intensity does not reveal the phase information of the electric field of the pulse. A highly chirped pulse has a longer duration than a laser pulse with a flat phase.

The pulse shown in Fig. 1.4 is also called 'chirped' pulse, since it resembles the acoustic analogon of birdsong. A tune that starts with a lower instantaneous frequency and ends with a higher instantaneous frequency is called up-chirped whereas the opposite is called down-chirped. This chirp is an effect of a non-flat spectral phase, more specifically of a quadratic spectral phase ϕ_2 (see 1.20). The term ϕ_0 in 1.20 is called the Carrier-Envelope-Phase (CEP, see Fig. 1.5) and describes the offset between the envelope (red, on the right in Fig. 1.4) and the carrier wave (blue, same figure). Usually this offset has a negligible influence if the pulse duration is longer than 10fs because the electric field strengths' change is comparably small from fringe to fringe.

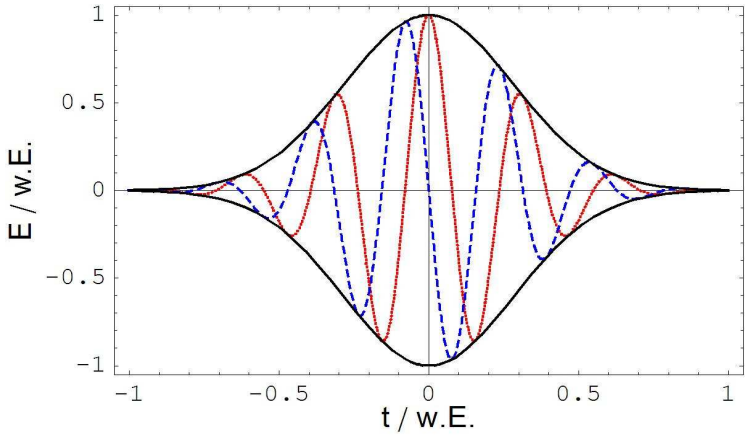

Figure 1.5: Two different electric fields of a laser pulse leading to the same envelope (black, solid). The cosine pulse (red, dotted) has its maximum field strength at $\phi = 0$ and the neighboring peaks (at opposite sign) do only have $\approx 80\%$ of its amplitude. On the other hand, the sine pulse (blue, dotted) has two opposing but equally high maxima at $\phi_1 = \frac{\pi}{2}$ and $\phi_2 = -\frac{\pi}{2}$. The latter pulse is not useful for ionization gating (3.1.3) due to having the same field strength twice per pulse.

When dealing with pulses shorter than 4-5 optical cycles (one optical cycle at 800nm = 2,7fs), it becomes important to know [20] or even control [21] this phase. Especially for high-order harmonic generation (see Chapter 3) in the sub-fs regime the CEP plays an important role [22, 23] (a review on attosecond physics can found here [24, 25, 26]). The first-order phase ϕ_1 is called linear phase because of its linear dependence on intensity and works as a temporal shift in the time domain.
One important aspect of filamentation (see 1.2.2) is that self-phase modulation in the interaction medium as well as blueshift in the plasma is changing the laser pulse spectrum [27, 28, 29]. The former is described by 1.21 and the latter can be explained by the fact, that the abrupt increase of the free electron density leads to a sudden decrease of the refractive index. Since for femtosecond laser pulses the recombination time of the electron is much longer than the pulse duration, the electron density increases monotonically throughout the laser pulse. Therefore the refractive index of the medium is constantly decreasing while the laser pulses is passing by, which causes a blueshift.

1.2.4 Chirped Mirrors

Besides the normal silver or gold mirrors used for 800nm laser pulses with normal anti-reflex coating, there are dielectric mirrors as well. They are based on the idea of a Bragg mirror [30] that consists of a sequence of alternating layers of two different optical materials. These two layers are matched so that the reflections from all interfaces interfere constructively. This way very high reflectivities for certain wavelengths and/or very broadband mirrors can be constructed. Dielectric mirrors are used wherever highest reflectivities under well-defined (angle, wavelength, bandwidth) conditions have to be realized. In the laser system in section 1.3.3 such mirrors are used as terminal mirrors in the oscillator cavity, in the amplifier stage for the seed beam, and between pump laser and amplifier always minimizing the losses by transmission

For our later described laser pulse compression setup we use a special kind of dielectric mirrors. Here the spacing between the different optical materials is not constant but changes along the lightpath in the medium (see Fig. 1.6). This has been demonstrated to perform as a low-loss compression device when used for dispersion control [31]. In Chapter 2, a chirped mirror with a specific quadratic phase ϕ_2 of $200fs^2$ per reflection is used to compensate the accumulated chirp from the filament.

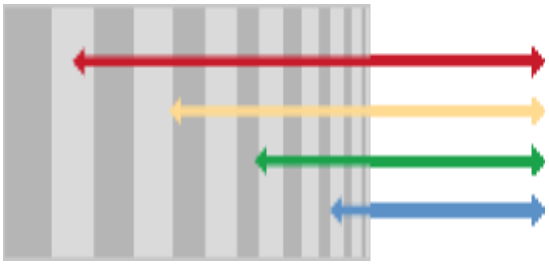

Figure 1.6: Schematic of a chirped mirror with different wavelengths being reflected most efficiently at certain 'depths' of the mirror. This leads to a specific delay between the different frequencies of the laser pulse (from [30]).

1.2.5 Spatial Beam Parameters

In 1.1 we considered the laser pulse to be a flat wave with no x and y limitations. Although this was mathematically correct, for a closer look at the spatial properties of a laser pulse all three dimensions are important while the temporal dimension can be neglected for this description. So to compute the behavior of the beam close to a focus or considering the divergence we should look at 1.7 but with a dependence on x,y,z and t:

$$E(x,y,z,t) = U(x,y,z)E_0 \; cos(k_z z - \omega(k_z)t) \tag{1.22}$$

where $U(x,y,z)$ is a scalar that gives the transversal beam profile. Assuming that $U(x,y,z)$ only changes slowly with z one can use 1.22 in the wave equation 1.6 and separate the temporal terms:

$$\left(\frac{\partial^2}{\partial x^2} + \frac{\partial^2}{\partial y^2} - 2ik_0\frac{\partial^2}{\partial z^2}\right) U(x,y,z) = 0 \tag{1.23}$$

This only holds for the paraxial approximation where $\frac{\partial^2 U}{\partial^2 z} \ll \frac{\partial U}{\partial z}$. For normal geometries of laser optics when no strong focusing element ($f \gg$ beam diameter) is employed, this

approximation is valid. One set of solutions of 1.23 is called Gaussian beams and they can be written as:

$$U(x,y,z) = \frac{U_0}{\sqrt{1+z^2/\rho_0^2}}\, e^{-i\theta(z)} e^{-ik_0(x^2+y^2)/2q(z)} \tag{1.24}$$

This solution can be plugged in 1.22 and one gets the electromagnetic field in three spatial and one temporal dimension. The beam parameter q is defined by

$$\frac{1}{q(z)} = \frac{1}{R(z)} - \frac{i\lambda_0}{\pi w^2(z)} \tag{1.25}$$

where $\rho_0 = n\pi w_0^2/\lambda_0$ is the Rayleigh range, $R(z) = z + \rho_0^2/z$ is the curvature of the beam waist, $w(z) = w_0\sqrt{1+z^2/\rho_0^2}$ is the beam waist, and $\theta(z) = arctan(z/\rho_0)$ is the Guoy-phase. Here $w_0 = w(z=0)$ is defined on the z axis where the beam waist is smallest. These formulas are only valid assuming a so-called TEM_{00} mode for the laser beam. However, one can use this theory and add a term to take care of the non-perfect mode of the laser beam:

$$w(z) = w_0\sqrt{1+(M^2\frac{z}{\rho_0})^2} \tag{1.26}$$

where M^2 is the beam quality parameter that is equal to 1 for a TEM_{00} beam and larger than 1 for all realistic laser beams. In section 2.3 a way to measure this parameter is shown as well as the M^2 values of our laser system.
This description is the basis for our later experiments for the characterization of the spatial profile of the high-order harmonic generation radiation. More details on the exact mathematical computation and experimental realization of soft X-ray wave-front analysis is given in Chapter 4. The M^2-parameter can be computed from the wave front of the beam if the spatial intensity distribution is detected along with the wave front.

1.3 Characterization and Generation of Ultrashort Laser Pulses

One problem that is always present when dealing with ultrashort laser pulses is the problem of measurement. In the introduction the temporal resolution was already introduced - though in a very abstract way. For our laser pulse, the temporal resolution becomes a very real problem because there is no electronic device such as an oscilloscope that might accurately detect sub-ps pulses. Today, the fastest electronic switches are in the regime of 100 ps. Therefore another question arises: How are these ultrashort light pulses generated? These two questions, the measurement - or more precise the temporal and spectral characterization - as well as the generating processes of femtosecond laser pulses are treated in this section.

1.3.1 Autocorrelation

An intuitive approach to measure the shortest man-made events is to use a part of the short pulse itself and measure the overlap between original and copy of the pulse. Like taking pictures with a camera, it is either possible to use a quick shutter in order to detect quick processes or the process is only illuminated for a very short time and the detector measures continuously. This is pretty much the way how an autocorrelation works.
The laser beam is split up into two parts with approximately the same intensity. One part goes through a delay line before spatially overlapping with the second part of the beam. Now one can exactly detect the signal of the two beams in dependence of the temporal delay that may be controlled very accurately. In our setup we use an piezo-driven closed-loop actuator that has a spatial resolution along its axis of motion of 2nm (Piezosystem Jena, PX100). This allows for a temporal delay precision of less than 10 attoseconds which is fully sufficient. A scheme of the setup is shown in Fig. 1.7.

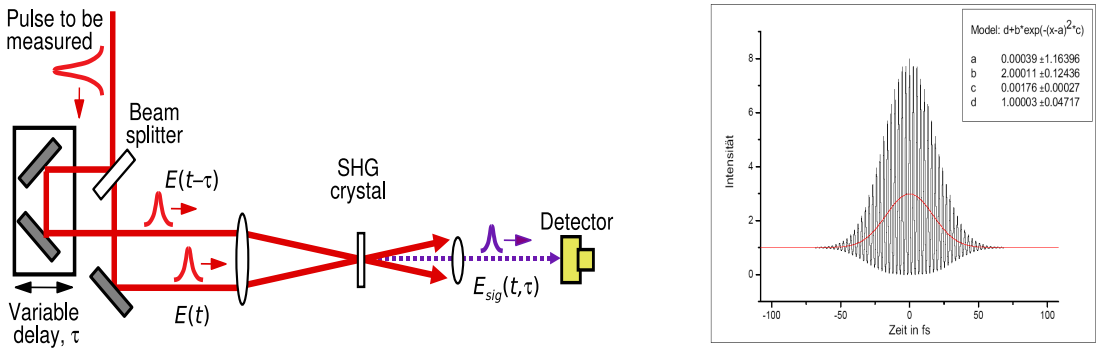

Figure 1.7: On the left is a typical setup of an interferometric autocorrelator using a nonlinear crystal for second-harmonic generation (SHG). The detector measures the intensity of the the two temporally sheared pulses. On the right is a simulated IAC signal for a 25fs Gaussian-shaped pulse.

To detect only the combined signal of both beams one can use different methods: second-harmonic generation in a nonlinear optical medium or a large-bandgap photodiode. In the first case, both beams are focused into a nonlinear crystal (eg. beta-barium borate, BBO) and only the sum-frequency of both photons is detected with a photodiode. The

alternative is to use two-photon photodiode that has a large enough bandgap so that only two-photon processes contribute to the photocurrent while the single photons' energies are below the bandgap energy. While the photodiode is easier to handle it is less sensitive because two-photon absorption is a much weaker process than sum-frequency generation in a nonlinear crystal. However, in both cases the signal from frequency-doubling or two-photon absorption depends quadratically on intensity. The overlap signal of the two E-fields is given by

$$E(t,\tau)_{res} = E(t) + E(t-\tau) \tag{1.27}$$

where t is the time and τ is the temporal delay between the two pulses. If the two laser pulses are coherent, which is generally the case, $E_{res}(t,\tau)$ is the result of destructive or constructive interference. Because this interferometric footprint in dependence of the delay is measured with the detector, this method is also called interferometric autocorrelation (IAC). The intensity of the resulting E-field is

$$I_{iac}(\tau) = \int_{-\infty}^{+\infty} \mid E_{res}(t,\tau)^2 \mid^2 dt = \int_{-\infty}^{+\infty} \mid (E(t) + E(t-\tau))^2 \mid^2 dt \tag{1.28}$$

In case $I_{iac}(\infty)$ and $I_{iac}(0)$ are computed

$$I_{iac}(\infty) = 2\int_{-\infty}^{+\infty} \mid E(t)^2 \mid^2 dt = 2\int_{-\infty}^{+\infty} E(t)^4 dt \tag{1.29}$$

$$I_{iac}(0) = \int_{-\infty}^{+\infty} \mid (2E(t))^2 \mid^2 dt = 16\int_{-\infty}^{+\infty} E(t)^4 dt \tag{1.30}$$

This ratio between the intensities at complete overlap at $\tau = 0$ and at $\tau = \infty$ gives a characteristic peak-to-background ratio of 8:1 shown on the right in Fig. 1.7.
In the graph in Fig. 1.7, the quickly oscillating part is the carrier signal that is generated by the interference of the two almost identical pulses (replica). The pulse duration can be extracted from the envelope of the I_{iac} but no evidence of the exact temporal shape is given. Thus all reconstructed pulse durations depend on the pulse shape. For example, if a $sech^2$-pulse is characterized, the ratio between τ_{iac}, the full-width at half maximum (FWHM) of I_{iac}, and τ_{pulse}, the FWHM of the real pulse duration, is given by the deconvolution factor, which in this case is ≈ 1.9. A list of more deconvolution factors for many pulse shapes can be found in [3]. From section 1.1 we know that a pulse is only completely characterized if temporal or spectral intensity and phase is known. From interferometric autocorrelation, it is only possible to guess the phase of the original pulse [32] with a very low reliability and only for the first three orders of ϕ. To detect the phase, a different method is needed and the one used in our laboratory is described in 1.3.2.

1.3.2 Spectral Interferometry for Direct Electric-Field Reconstruction

Another method to characterize laser pulses is to make use of spectral interferometry utilizing the SPIDER [33] technique. In the former setup for autocorrelation we detect the temporal interference between two replica. It is also possible to measure the spectrum of two identical pulses which propagate collinearly but have a time delay τ. Their frequency components will overlap and interfere which causes a modulation in the resulting spectrum; this is called spectral interferometry (SI). The average fringe-to-fringe distance in the

spectrum is antiproportional to the delay between the pulses. The phase difference for each spectral component is also encoded in the deviation from the periodic modulation of the spectrum.
Now we assume that the spectrum and phase of one of the two initial pulses is known whereas the second pulse undergoes some kind of unknown phase change. From spectral interferometry of the two pulses, the phase of the second pulse can be obtained from the modulation of the spectrum. The interference pattern $I_{SI}(\omega)$ can be described by

$$I_{SI}(\omega) =\mid E_1(\omega) + E_2(\omega)e^{-i\omega\tau} \mid^2 \tag{1.31}$$

$$I_{SI}(\omega) = I_1(\omega) + I_2(\omega) + E_1^*(\omega)E_2(\omega)e^{i\omega\tau} + E_1(\omega)E_2^*(\omega)e^{i\omega\tau} \tag{1.32}$$

$$I_{SI}(\omega) = I_1(\omega) + I_2(\omega) + 2\sqrt{I_1(\omega)I_2(\omega)cos(\Phi_1(\omega) - \Phi_2(\omega) - \omega\tau)} \tag{1.33}$$

because it is a superposition of two pulses with $e^{-i\omega\tau}$ being the phase delay caused by the temporal delay τ. The * indicates the complex conjugate of the E-fields. If one detects the two single spectra $I_1(\omega)$ and $I_2(\omega)$ and subtracts them from the interference term, the result is

$$S(\omega) = I_{SI}(\omega) - I_1(\omega) - I_2(\omega) \tag{1.34}$$

$$S(\omega) = E_1^*(\omega)E_2(\omega)e^{i\omega\tau} + E_1(\omega)E_2^*(\omega)e^{i\omega\tau} \tag{1.35}$$

$$S(\omega) = 2\sqrt{I_1(\omega)I_2(\omega)cos(\Phi_1(\omega) - \Phi_2(\omega) - \omega\tau)}) \tag{1.36}$$

where $\Phi_1(\omega)$ and $\Phi_2(\omega)$ are the phases of the two pulses, respectively. The difference $\Delta\Phi(\omega)$ can be computed either directly or via Fourier transform from 1.34. The reason for using the Fourier transform and extracting the $\Delta\Phi$ from $S(t)$ is that experimental noise, which adds a large error, can be filtered very effectively in the time domain.

Up to now, the reconstruction of an unknown phase $\Phi_2(\omega)$ of a pulse is only possible if the phase of the reference pulse $\Phi_1(\omega)$ is known. However, normally one wants to characterize a pulse just by itself without providing a special reference pulse. The method that was introduced by Iaconis and Walmsley in 1998 [33] shows a way out of this dilemma: They suggested using the SI-setup described above but not only with a time delay between the pulses but also with a well-defined spectral shear Ω between E_1 and E_2. In this case the SPIDER spectrum $S(\omega)$ is equal to 1.33, but with $I_2(\omega) = I_1(\omega + \Omega)$ and $\Phi_2(\omega) = \Phi_1(\omega + \Omega)$. As before the phase difference $\Delta\Phi = \Phi_1(\omega) - \Phi_2(\omega)$ can be extracted from a SI-measurement. If Ω is sufficiently small and τ can be determined exactly, one can write

$$\Delta\Phi(\omega) = \Phi_1(\omega) - \Phi_2(\omega) = \Phi_1(\omega) - \Phi_1(\omega + \Omega) \tag{1.37}$$

$$\Phi_1(\omega)' = \lim \frac{\Phi_1(\omega + \Omega) - \Phi_1(\omega)}{\Omega} \tag{1.38}$$

and get $\Phi_1(\omega)$ by simple integration. Since an infinitely small Ω is not accessible one has to keep in mind the Nyquist ratio (see 1.39) and adjust Ω accordingly to get a valid reconstruction of the phase. It is crucial that the chirped and thereby temporally stretched pulse is much longer than the two replica so that each of them has a quasi-constant frequency. On the other hand the two replica need to be temporally close enough, so that the fringes recorded with a spectrometer can be detected separately. This is also formulated in the Nyquist limit of sampling, which says that the maximal measurable frequency is half the sampling frequency. Thus the spectrometer resolution $\delta\omega$ needs to be better than

$$\delta\omega = \frac{\pi}{\tau} \tag{1.39}$$

in order to sample the spectral fringes completely. The setup used for our SPIDER measurements is depicted in Fig. 1.8.

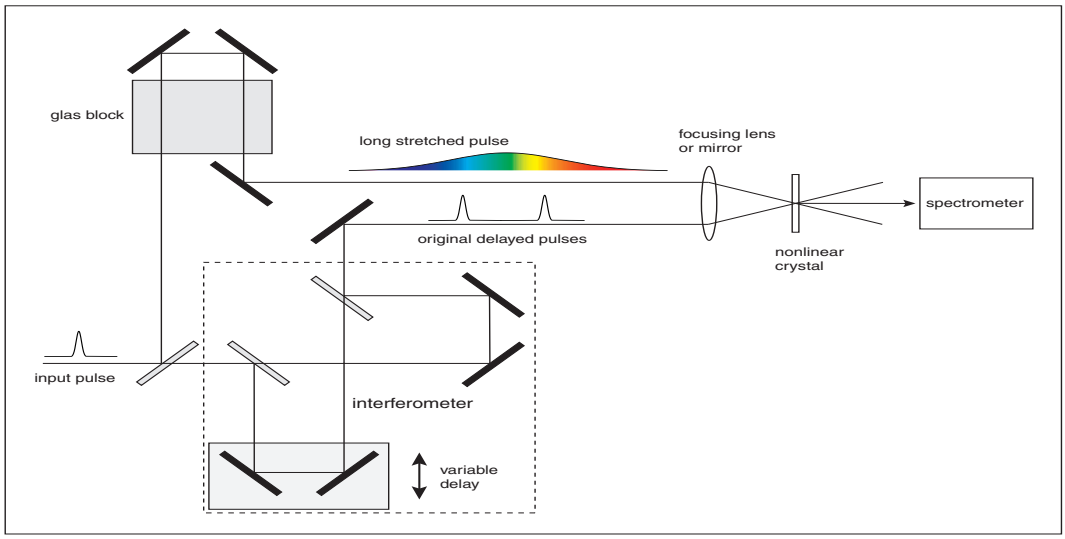

Figure 1.8: Schematic of the setup for Spectral Interferometry for Direct Electric-Field Reconstruction. The laser pulses comes from the left and the spectrally broadened pulse and the two replica are overlapped in the nonlinear crystal with the sum-frequency being detected in the spectrometer.

Measured SPIDER data is shown in Fig 1.9 where (a) is the recorded trace of an unmodulated broadband laser pulse. The fringes indicate the spectral interferometry and one can see the doubled frequency as X axis. In (b) the measured spectral intensity and reconstructed phase versus wavelength are plotted. From this we computed the temporal intensity and phase given in (c) which exhibits a pulse train of about 100fs. Because this phase function is not smooth and continuous it can obviously not be compensated by a prism or grating compressor.

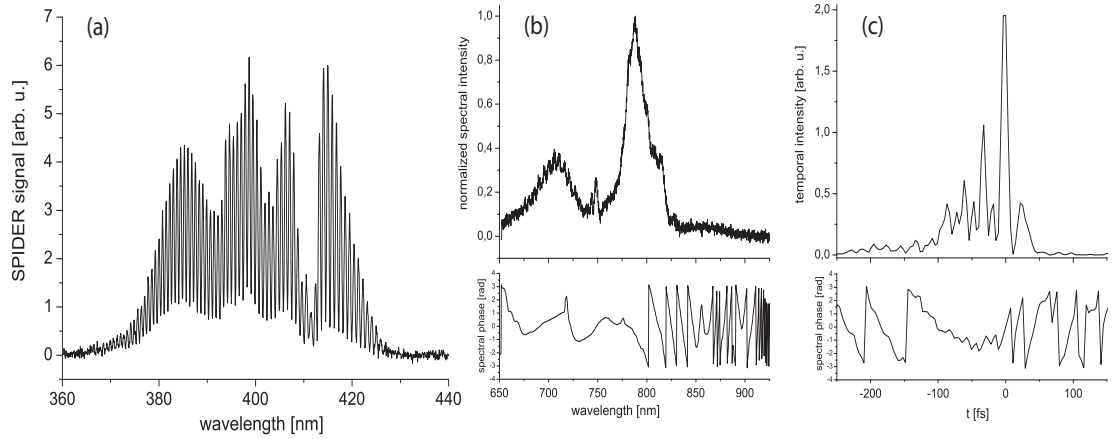

Figure 1.9: A measured SPIDER trace is given in (a). (b) shows the spectral intensity (top) and reconstructed phase (bottom) versus wavelength. In the right part (c) one can see the temporal intensity distribution (top) and temporal phase (bottom) also plotted versus wavelength. The phases are both plotted modulo 2π.

A third technique to measure the intensity and phase of a laser pulse is the frequency-

resolved optical gating (FROG) [34]. It is basically an autocorrelation measurement with a spectrally sensitive detector that does not only monitor the intensity changes but also the spectra at different delays. For the reconstruction of intensity and phase an algorithm is needed so no real-time reconstruction is possible. However, compared to the SPIDER setup a FROG is relatively simple to built and implement and is a widely used and reliable tool. Since no FROG measurement is used in this work it is just mentioned for completeness of the major three techniques to analyze ultrashort laser pulses.

A comparison between the three described techniques can be found in [35]. Concluding, both FROG and SPIDER allow good characterization of spectral phase and intensity and thus the exact electric field while autocorrelation does only yield the pulse duration. On the other hand, for both FROG and SPIDER some software and/or iterative fitting is necessary which makes them vulnerable to numerical or fitting errors. The advantage of the autocorrelation technique is its robustness and that no data evaluation whatsoever is needed an the pulse duration can be directly read from the fringe pattern.

1.3.3 A state-of-the-art Laser system

To achieve pulses so much shorter than the fastest electronic switches some tweaking of optical techniques is necessary. In 1966 mode-locking was demonstrated for the first time and allowed pulses as short as 100ps [36]. It implies that the longitudinal modes in the laser cavity are forced into a fixed phase correlation allowing stable temporally periodic structures (pulses) to be emitted. This and the discovery of titanium-doped sapphire in 1986 [37] as a very broadband lasing medium led to smaller and easier-to-handle tabletop high-power laser systems. The last major step to even higher intensities and shorter pulse durations is Kerr-lens modelocking (KLM) which is illustrated in Fig. 1.10.

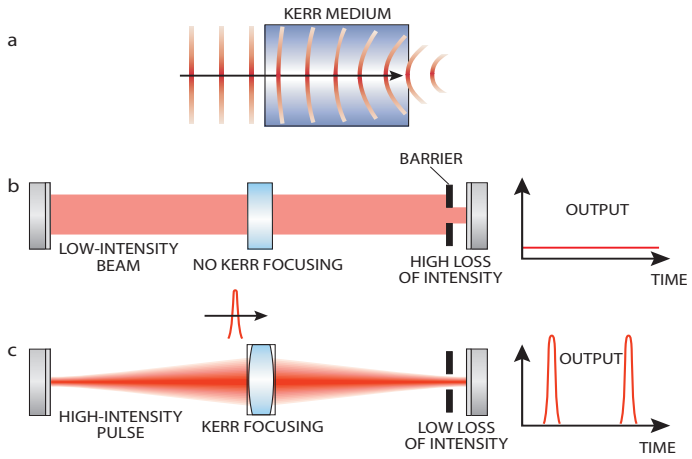

Figure 1.10: Schematic of the Kerr-lens modelocking [38]: In a) one can see the self-focusing of intense laser radiation in media. Part b) shows a cavity build for low peak intensities, where high losses are caused by the barrier. In c) is demonstrated, that a lens-like function of the lasing medium is minimizing the losses. And a single pulse contains the most energy and therefore is focused optimally through the barrier.

As mentioned in 1.2.1, the optical Kerr effect leads to self-focusing of intense laser pulses in dispersive media. If the cavity is detuned in a way that only high-intensity (pulsed)

modes have low losses then all modes will sooner or later automatically merge into one large pulse because of its high intensity. This allows for short pulse durations of about 12fs from the Ti:Sa-based oscillator (Femtopower Femtosource) with a central wavelength of about 800nm. Usually, a solid-state laser runs in a continuous-wave (cw) modus and needs to be 'locked' once after the turn-on-procedure by slightly nudging the cavity mirrors. If the cavity is detuned a little bit from running under ideal conditions for cw, this small perturbation results in different longitudinal modes entering a fixed-phase state; the modes are locked.
The laser system used in this work consists of a the described oscillator that feeds a 800nm-Ti:Sapphire amplifier (Femtolasers Femtopower Compact Pro) pumped with a frequency doubled Nd-YLF laser (Photonics Industries GM30) at 532nm with energies of 10 mJ at 1 KHz. The amplifier is based on the chirped-pulse amplification (CPA) technique which was introduced by Strickland and Mourou in 1985. It allows much higher output intensities of the laser system because the damage threshold of the gain medium is not the limiting factor anymore. The principle is illustrated in Fig 1.11.

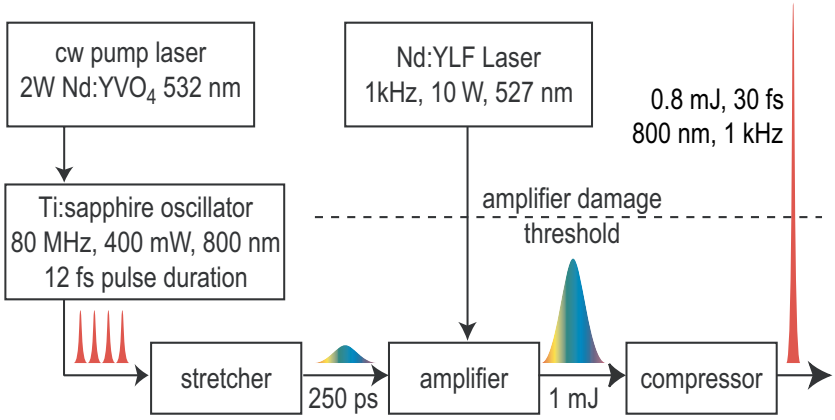

Figure 1.11: Overview of the working principle of a modern single-stage-amplifier Ti:Sa laser system. The oscillator generates short and high-repetition rate 800nm laser pulses from which a single pulse is stretched, amplified and compressed again.

If such short pulses were amplified directly, the laser intensity would exceed the damage threshold. To prevent this the pulses are chirped before amplification and then recompressed afterwards (see Fig. 1.11). The 80MHz pulses from the oscillator are not all amplified due to lower possible single-pulse energies since the pumped medium can only provide a certain amount of photons. Therefore a Pockels cell picks one pulse per 80,000 and this 1kHz laser pulse is then amplified by a factor of approximately one million. Thus the output is a 25-30fs laser pulse with a central wavelength of 800nm, a pulse energy of $0.8mJ$ and a repetition rate of 1kHz. For this work the shorter the pulses the better the experimental conditions and so the next chapter will deal with one way to further decrease the duration of these already ultrashort pulses.

1.3.4 Applications of Ultrashort Laser Pulses

Although still quite expensive, ultrashort laser systems have become useful tools in a number of applications. In science, the high temporal resolution is used for time-resolved spectroscopy in chemical or biological experiments. Here molecular vibrations or chemical

reactions can be detected and to some extent even influenced by specially tailored laser pulses. In material science, laser ablation utilizing femtosecond laser pulses shows some advantages over ablation with longer pulses. Even though the fundamental wavelength of the described system is fixed at 800nm, many applications allow the frequency conversion towards longer (difference-frequency mixing) or shorter (sum-frequency mixing or NOPA [39]) wavelengths. Conversion into a much higher energy regime will be described in Chapter 3. Only a short overview over some scientific problems that are tackled with the help of femtosecond lasers will be given here.
The broad spectrum linked with the high temporal resolution allows excitation of a superposition of vibrational modes in molecules. Utilizing pump-probe spectroscopy the created wave packet can be probed at various positions along its propagation along molecular potential-surfaces [40]. Not only one can analyze this molecular structure but it is also possible to influence chemical reactions using femtosecond laser pulses [41]. This led to a complete new branch at the border between physics and chemistry called 'femtochemistry' which was rewarded in 1999 with a Nobel prize to Ahmed Zewail [42].

In optical communication very often the question of how to convert light into an electronic signal arises. Not only the conversion but in an ideal case even 'steering' electrons with laser pulses [43] is a technique that is based on femtosecond laser systems. It was demonstrated that shaped laser pulses can create and move electron wave packets on a nanostructured surface. This opens a route towards real quantum computers where quantum mechanics meets conventional integrated electronics.

When it comes to metrology, the measurement of one dimension with very high precision, one can also employ a femtosecond laser system. Hänsch et al. [44] made use of the 'frequency comb' generated by femtosecond pulse trains with a fixed carrier-envelope phase. With these frequency combs it is possible to link macroscopic microwave frequencies used in our everyday life with the high precision of atomic clocks [45]. John L. Hall and Theodor W. Hänsch received the Nobel prize "for their contributions to the development of laser-based precision spectroscopy, including the optical frequency comb technique" in 2005.

One last application with a close link to the scope of this work is the use of femtosecond laser pulses for high-order harmonic generation (see Chapter 3). These soft X rays do not only carry the laser's properties, i.e. high spatial and temporal coherence along with high intensity, but also its temporal resolution. In fact, the duration of the generated pulses can be as short as a few hundred attoseconds [24, 25, 26] and even single pulses with this short duration have been created [46, 47, 48]. With this magnificently short light pulses completely new insights into inner atomic structures can be gained [49].

1.4 Evolutionary Algorithm

Very often the mathematical question arises of how to find a maximum of some global quantity F. In this case F is a function of n parameters x_n with x'_n being the set of parameters that produce the global maximum. If the x_n are unbounded continuous parameters, as it is the case in general for our optimizations, finding the optimal x'_n is a challenge. Furthermore, $F(x_i)$ often depends on the x_i in nontrivial ways and then not even local maxima can be analytically figured out by setting the partial derivatives $\partial F/\partial x_i$ equal to zero. Thus it is necessary to employ numerical, computer-based, and often heuristic search algorithms but they are frequently trapped in a local maximum.
The gradient-walk method, for example, will start at an arbitrary position in the n-dimensional space $(x_1, x_2, ...x_n)$. From then, it follows a constant 'uphill movement' which is defined by the direction of the gradient vector ∇. This leads to a maximum at which the gradient vanishes. The path that has been covered resembles a one-dimensional line from the starting to the ending point in search space. Since the search space is n-dimensional, even multiplied applications of this algorithm would not sample a significant part of it and finding the global maximum would be a lucky strike.

Evolutionary algorithms as used in this work are in a way ideal solutions to this problem. They are well-suited for global maximum search in a very high-dimensional search space. In a way, they mimic the natural selection process that has created all known forms of life on this planet. Any creature on earth is characterized by a very large set of parameters, commonly called genes. Here we are disregarding the fact, that the same creatures carry slightly different genetic information but for sake of simplicity, one creature is fully specified by a sequence of n genes $(x_1, x_2, ..., x_n)$. For some given conditions (climate, feed/prey, habitat), a creature having the best genetic sequence is best adapted; the environment serves as a function $F(x_i)$ producing higher and higher values F for individual creatures that are increasingly well adapted to the particular conditions. Evolution is therefore a constant optimization procedure in this n-dimensional search space. Nature found a way to manage this large search space by following a few principles building the modern foundation of an evolutionary algorithm:

- "Survival of the fittest" - This is the well-known Darwinian expression for the natural selection according to which more adapted creatures spread their genes more successful that unfit ones.
- Genetic crossover will help currently best adapted individuals to 'merge their experience' and produce offspring, that carries positive genetic information from both parents.
- Mutation is very important to prevent a narrowing of the search space. Individuals can statistically undergo changes of their set of genes which may in principle allow to reach any spot in the search space.

Iterative application of these principles allows for optimally adapted individuals in nature. A numerical and computer-based realization of this algorithm is illustrated in Fig. 1.12. After some iterations, the algorithm converges to a global maximum of the underlying subset of the search space. Of course, we also do not know whether we found the global maximum of the complete search space.

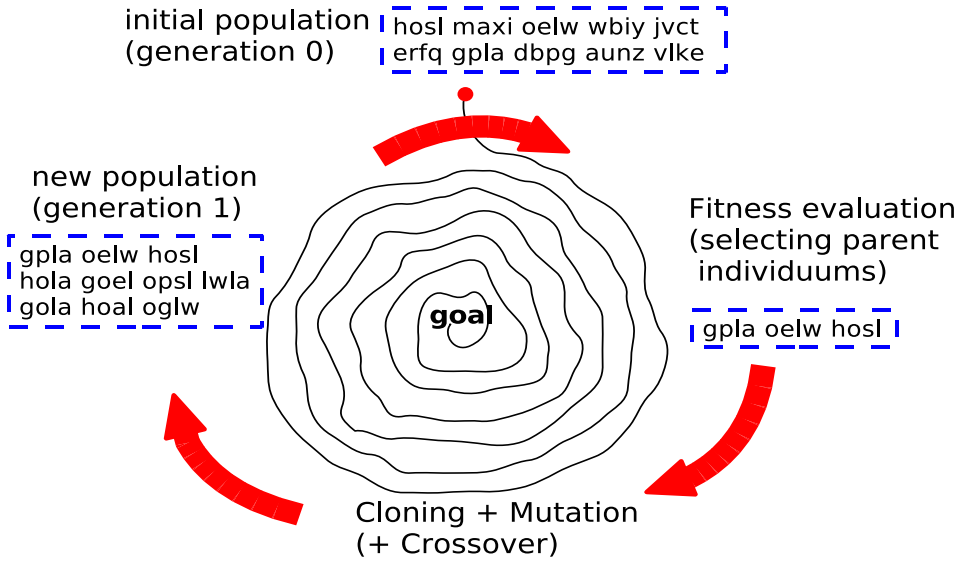

Figure 1.12: Schematic of the working principle of an evolutionary algorithm. In this example, one individual is defined by four genes (letters) that can take values from a to z. The goal of these *'word-individuals'* is the word **goal** itself. The algorithm starts at the top with an initial population, being called generation 0, in a blue dashed frame. From this, the fittest individuals - here the fitness has to be defined - are selected; in our case they have to resemble the letters g-o-a-l. It is noteworthy, that the exact definition of the fitness has a huge impact (Does the order matter? Is ± one letter ok?) on the progress of the algorithm.
From these selected individuals (so-called 'parents') the new population can be generated by cloning, mutation, and crossover. Thus generation 1 is created (blue dashed frame on the left) and the cycle starts again with the selection process.

Transferred to our optimization problems, we are dealing with a huge search space including for example all parameters of the electric field of a laser pulse. Even if the Hamiltonian of a nonlinear quantum system is known, F still depends on the electric field in a highly nontrivial way and cannot easily be computed. For chemical quantum systems, optimal control theory is dealing with this and tries to solve the optimization problem analytically. While this is a good theoretical approach, in experiments the systems are not as well characterized so that very often the exact Hamiltonian is not available. Additionally, harmonic generation is not just a quantum mechanical process but macroscopic effects (e.g. phase-matching) have to be taken into consideration, too. Thus the Hamiltonian of a single gas particle AND the wave equation would have to solved in a self-consistent way and this exceeds the modelling capability today. But even if a single ideal electric field could be computed, it would still have to be reproduced by the laser system and the pulse shaper, which both have their limitations.
Therefore in practice we restrict ourselves to parameterize the laser pulse so that the x_i can be attributed to specific experimental settings or parameters. The resulting $F(x_i)$ is measured experimentally and an evolutionary algorithm provides the tool to solve this multi-dimensional optimization problem 'in situ'. Thus we do not know the systems exact control scheme or the sub-fs processes but it is nevertheless possible to steer the system as previously described. In Fig. 1.13 one can see a typical setup used to shape laser pulses

arbitrarily to prepare them for a certain experiment and maximize whatever the goal is.

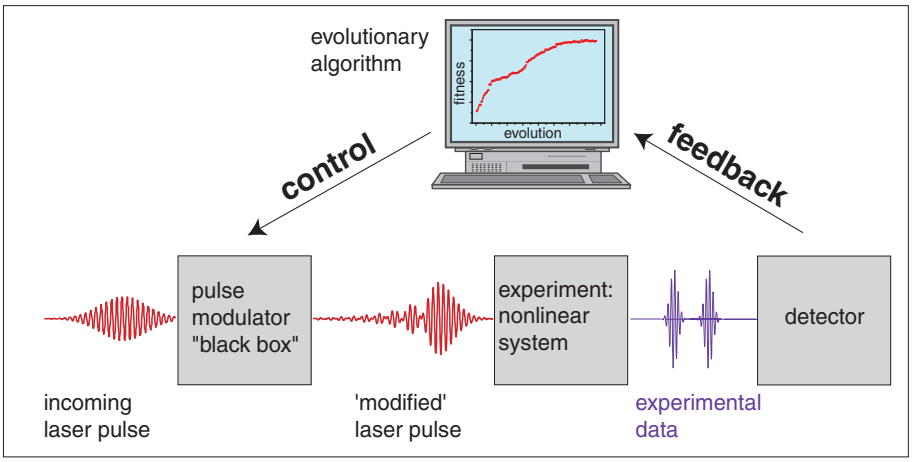

Figure 1.13: Schematic description of an iterative optimization using an input pulse that is modified by a pulse shaper before it enters the experiment. Its results are then fed back to the computer that controls the pulse shaper. Thus an optimal pulse shape can be found without knowing the quantum mechanical explanation.

As external 'tweaking parameters' one can change the cloning rate, that is the amount of individuals, that are taken over to the next generation. Normally this is kept constant in our evolutionary algorithm at a level of 10%. The second important number is the mutation probability (also mutation rate) which should not be too large to prevent positive and negative mutations to counterbalance. This can occur when for every positive change at least one negative change is introduced and thus the fitness is not necessarily higher than for the unchanged individual. On the other hand if the mutation rate is too little, only local optima rather than the global maximum are discovered. A second mutation parameter is the mutation amplitude (e.g. in %) that also needs to be chosen reasonably to balance stagnation with overly-large progress. Crossover, corresponding to sexual reproduction, is not an essential part of our evolutionary algorithm but may help at certain difficulties. The crossover rate normally is adjusted to the exact experimental conditions or left out (in some of our experiments). Both crossover and mutation are usually using a percentage (the fittest part) of the whole population as parental individuals. This 'parent rate' is another possibility of fine-tuning.

A big advantage of the evolutionary algorithm over other optimization methods is the self-teaching effect because of the 'genetic pool' of information that is always forwarded to the next generation. For our applications this is extremely useful because we do not have an analytical solution to our problem but have to rely on the algorithm to find it. Another advantage of this self-teaching algorithm is that one can neglect the different phase-to-wavelength ratios. For example, the fact that a 2π jump for 800nm is a 2.2π jump for 900nm will automatically be included in the optimization.

Chapter 2

Adaptive Pulse Optimization

As previously mentioned a major part of this work is about preparing laser pulses as good as possible for their application. For high-order harmonic generation (HHG, see Chapter 3) the duration of the laser pulse is a crucial parameter. In this chapter our approach to compress the pulses temporally as well as to optimize them spatially is described. From the introduction and 1.1 we know that a broadening of the spectrum e.g. with SPM (1.2.3) must be achieved in order to decrease the temporal duration. For this, traditionally, the laser pulse is coupled into a hollow glass fiber which is filled with a gas at defined pressure. The nonlinear interaction between laser pulse and gas leads to a broadened spectrum as well as a quadratic chirp due to nonlinear dispersion. The glass tube serves as a waveguide to maintain a high intensity over a long distance. With a prism compressor, a set of chirped mirrors or an adaptive pulse shaper this chirp is minimized in this work to realize laser pulses as close to the Fourier limit as possible (described in section 2.2).
What is relatively new in the second part of this experiment is the use of a different technique for spectral broadening: We use an Ar-filled tube without a hollow-core fiber where the laser creates a filament (see 1.2.2) in which the SPM takes place. This will be described in section 2.3 in more detail.
The advantages versus disadvantages between glass capillary and filament are briefly summed up here:

hollow-core fiber	**filament**
$\oplus$ mode selection	$\oplus$ high transmission ($\geq$90%)
$\oplus$ good beam profile	$\oplus$ very robust
$\ominus$ high losses ($\approx$ 40%)	$\oplus$ good scaling
$\ominus$ sensitive coupling	$\ominus$ spatial chirp

We implemented an experimental setup to compare the 'traditional' capillary and a newer filament stage that can be seen in Fig. 2.2. In the first part of this chapter, the pulse shaper used for all optimizations is described. Then SPM in a gas-filled hollow-core fiber and the 'newer' filementation technique to obtain compressible laser pulses will be explained in a little more detail. The last part is a brief explanation why and how we could improve the evolutionary algorithm in terms of parameterization and progression.

2.1 Pulse Shaping using a Spatial Light Modulator (SLM)

While the temporal compression of laser pulses using chirped mirrors or a pair of prisms is straightforward ([50, 51]) we chose to employ a more flexible device in order to control our laser pulse properties. Our spatial light modulator Hamamatsu Photonics PAL-SLM X8267 (details see Appendix A) is a reflective pulse shaper. It enables us to arbitrarily introduce a phase delay of zero to three π for 800nm at a specific position of the active area. In theory, this phase amplitude allows for arbitrary phase masks because every desired phase can be displayed modulo 2π.

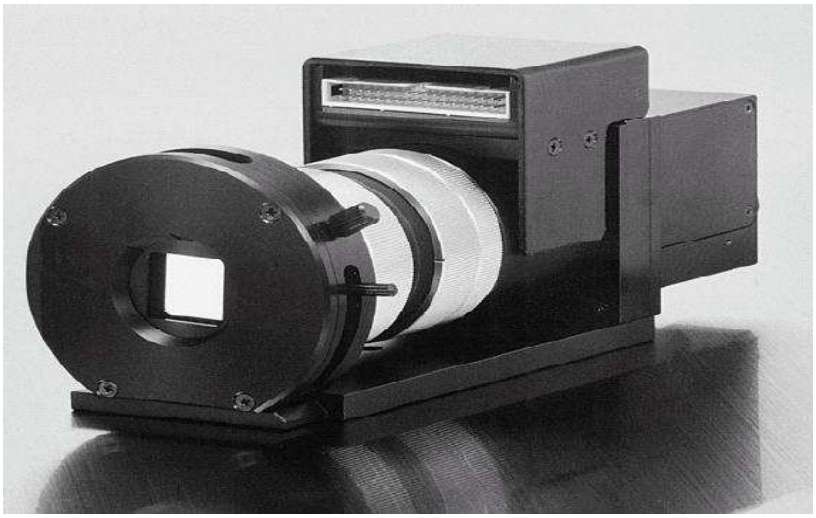

Figure 2.1: Photograph of the 2-D SLM Hamamatsu Photonics X8267. The active area is the $20x20mm^2$ squared golden mirror on the left; imaging LCD mask, laser LED, and connectors are behind on the right side.

The active area consists of 768x768 pixels which are addressed like a monochrome computer screen: each pixel has a 'depth' of 8 bit corresponding to green values from 0 to 255. The reflectivity of this reflective area is larger than 90% for wavelengths from 700 to 1000nm. When used below 700nm, the absorption grows too large for an effective modulation. In addition to low reflectivity, at wavelength larger than 1000-1100nm the maximum phase modulation gets smaller than 2π. Another technical reason for our limitation to a bandwidth of 200nm was the grating-based setup: if a broader spectrum were to be supported, one pixel would shape to many frequencies. So in terms of a compromise, we employed a blazed gold grating with 300 groves/mm and a cylindrical mirror to project the Fourier-plane onto the SLM. Thus the spectral resolution is good enough ($< 0.5nm$ per pixel) while being able to shape a bandwidth of 200nm.
Also, too high intensity can not only damage the reflective surface but because the phase mask is 'written' by a backlight, the laser impinging to the front influences its phase, too. This results in another 'self-phase modulation' (different from the one explained in section 1.2.3) because the laser's intensity writes its own phase modulation even without the intended 'writing light'. For our experiments this means that we have to spread the laser beam as good as possible over the whole phase modulator to prevent this 'self-writing'. A complete characterization of this SLM was done in the scope of [50]. Our pulse shaper is addressed like a 768x768-pixel computer monitor via VGA cable but only the 'green' pin

carries the necessary information. Therefore the images of the phase front are monochromatic green pictures where a phase offset of $2\pi \sim 255 \sim brightgreen$ and $0\pi = 0 = black$. The reason for 2π being not always bright green are the different wavelength we are dealing with.
When used as a temporal pulse shaper (in sections 2.2.2 and 2.3.1) the SLM is placed in the Fourier plane of a prism or grating compressor [52]. By applying different delays at different frequencies it is possible to change the spectral phase arbitrarily. In the spatial shaping setup (section 2.3.2 and 2.2.2), the laser pulse is simply reflected by the active area like from a mirror surface. This allows to form the wavefront in a very exact manner to match its special purpose or correct minor irregularities. Naturally, a combination of both would allow the most promising approach and in section 2.2.2 this is experimentally realized, too.

2.2 Optimization after a gas-filled hollow-core Fiber

To compare this SPM via pulse propagation in a gas-filled hollow-core fiber with the later filament, we built a 'two-mode' setup for direct comparison. This is shown here:

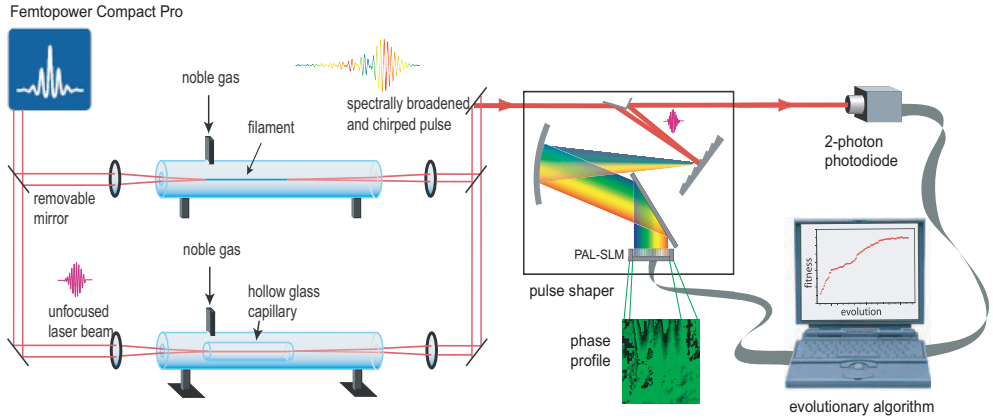

Figure 2.2: This shows our laboratory setup with the possibility to use a hollow glass capillary or a filament for spectral broadening. Either way, the spectrally broadened laser pulses travel through our pulse shaper unit with the PAL-SLM as the high-resolution phase shaper. Afterwards the pulses are detected with a 2-photon photodiode. The whole optimization procedure is monitored by an evolutionary algorithm to achieve the best possible result (global maximum=Fourier-limited pulse) from the given spectrum.

2.2.1 Temporal Shaping

From other experiments [53, 54] we know that octave-broad spectra in the visible/NIR and compression down to $< 4fs$ have been successfully demonstrated. However, the energy of the dramatically shortened pulses is mostly on the order of less than $300\mu J$. Thus, our first approach to temporally shorten the laser pulses was to couple them into a gas-filled hollow-core fiber with a diameter of $\approx 200\mu m$ (various sizes between 150 and 250 μm were used) and a length of about $50 - 100cm$. At moderate pressures $p \approx 200 - 400mbar$ we could observe very clear self-phase modulation around 800nm (see a) in 2.3). The energy throughput was measured to be between 40% and 55%. Most of the losses can be attributed to coupling the laser into the capillary and losses from scattering due to imperfections of the fiber. Ideally we could swap the beam from filament to hollow-core fiber and back to measure for example spectral phase and intensity after both. Experimentally, the coupling into a $200\mu m$ fiber and exciting the proper modes (more about mode excitation in 3.2.1) is much too sensitive to be repeatable without new adjustment. Spectral intensity as well as overall throughput depend strongly on proper adjustment of the coupling process. A typical spectrum with a good beam profile (not shown) and spectral broadening can be seen in 2.3.
From Fourier transformation of the spectrum in Fig 2.3 a) we can see that the two deep holes will lead to pre- or postpulses in the time domain. Later on, this will be shown in a measured IAC. On the right part of Fig 2.3, it is interesting to note that although the 32x32 planes were free to move in any direction, they clearly favored changes in the horizontal direction. Vertical changes are much smaller which leads to an overall stripe-like

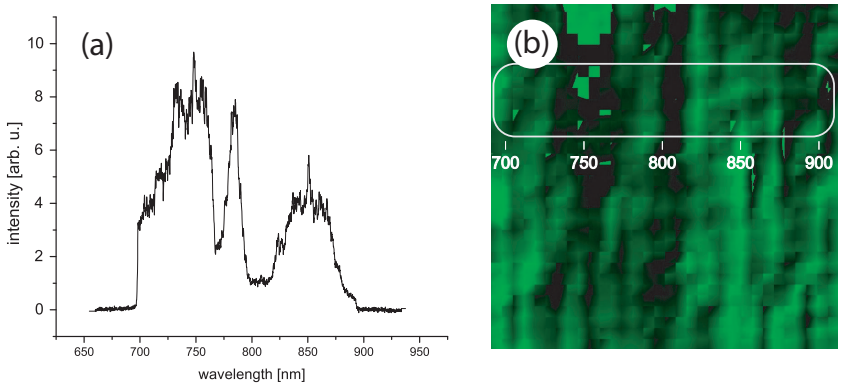

Figure 2.3: a) shows the spectral intensity of the laser pulse after propagation through the gas-filled hollow fiber. In b) the phase mask after optimization is given. One can establish a link between pixels and wavelength but the optimal phase is found arbitrarily. Also visible is the limit of our setup to a bandwidth from about 695nm to 890nm.

phase modulation. From the background of a horizontally expanded spectrum this proves that the algorithm found the more important parameters automatically. An explanation why we used planes instead of simply pixels will be given in section 2.4.
Using the optimization setup described above, we first pre-compensated any chirp of the pulse by adjusting the pulse shaper setup for a maximum signal at the 2-photon photodiode. This we did by fine-tuning the grating-cylindrical mirror distances and thus changing the quadratic phase introduced/compensated by the setup. By applying a flat phase to the SLM this manually optimized signal was measured to be the reference signal. But this reference was not only measured once at the beginning of the optimization but once per generation of the evolutionary algorithm. Doing this we could make sure that intensity deviations of the laser system or changes of the coupling into the fiber would not distort our optimizations extremely. Of course a certain stability of the whole system (laser, spectral broadening, pulse shaper) is necessary in order to perform these several-hours-long optimizations.
The results of our optimization are shown in Fig. 2.4.

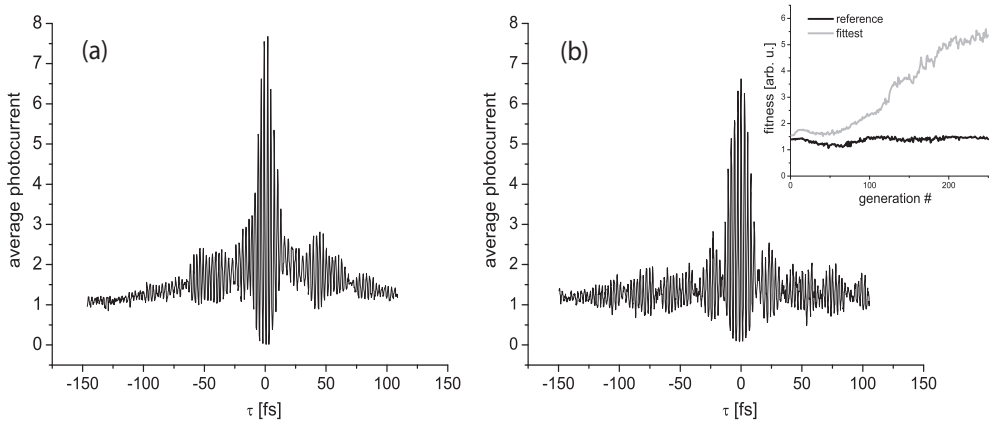

Figure 2.4: Interferometric autocorrelations of the laser pulse before (a) and after (b) optimization. The inset in (b) shows the development of the fitness as computed and optimized with an evolutionary algorithm.

From the inset in 2.4 b) one can see the constant increase of the fitness of the fittest individual (grey) while the reference (black) stays at approximately the same level. The reference is measured once per generation by applying a flat phase to the SLM and its fitness corresponds to the black line. The initial pulse in 2.4 a) is about 12fs long but has a quadratic chirp which can be seen from the hill-shaped 'background' fringes. From now on, this will be referred to as 'wing-structure' because of its bird-like shape. The already-short pulse duration was achieved by adjusting the pulse-shaper setup to maximally compensating the phase (see text above). But it was only after optimization with the evolutionary algorithm that these wing-structures are brought down to weak pre- and post pulses. As mentioned before, using this spectrum it is not possible to completely get rid of these pedestals. The pulse duration in 2.4 b) is only a little shorter at about 11fs.

All in all, it was possible to run optimizations by using the SLM as temporal phase shaper and thereby flattening the spectral phase as presented in 2.4. There is no directly measured phase but from the pulse duration being close to the Fourier-limit of the spectrum a nearly flat phase can be safely assumed. The good temporal structure and useful beam profile unfortunately come along with drawbacks like low energy-throughput (with spatial filtering less than 30%) and tedious alignment procedure before and during every optimization.

2.2.2 Spatio-temporal Shaping

Like many amplified laser systems, our laser has a vertical drift of some $mrad/hour$. For most experiments this is not crucial, but using a hollow-core fiber with a diameter of only a few hundred μ, it can be critical. Not only does the throughput change but the whole coupling process of the focused laser beam into the fiber is somewhat different. Very often, high-order fiber modes are excited which then leads to complex intensity profiles with spatial chirp after the capillary. To compensate this effect, one idea is to let the SLM work as a 2-D spatial shaper and not only 1-D in the time domain.
Up to now the SLM was capable of applying a temporal phase and at the same time shape the laser pulse spatially in one dimension (vertically) in the Fourier plane. In [50] a further improvement of the pulse shaping setup was suggested by dividing the active area of the phase shaper into a spatial and a temporal part. Because the SLM is not sensitive to where and how often the laser beam is reflected, only the software needs to be aware of the double shaping process. On the upper part the laser pulse should be shaped spatially (means: directly applying a phase to the beam profile) while on the lower part the temporal shaping takes place. We changed the setup to make this dual shaping possible but due to more reflections and geometrical reasons the throughput of the complete shaper was reduced to 50%.
Since the evolutionary algorithm is trying to modulate the beam spatially so that the signal of the photo diode is maximized, it will start focusing the laser beam. This smaller spot size on the diode can increase the photocurrent and thus seems very 'fit' although the pulse shape has not improved. A too small spot size can also bring the photo diode into saturation and make any further optimization impossible. To get rid of saturating the diode, we had to use more attenuators which lowers the signal-to-noise ratio. The focusing could be prevented by placing a pinhole where the detection setup was before and moving the photo diode backwards. By this spatial filtering the laser beam had to pass the pinhole always with the smallest diameter (focus) because otherwise the photocurrent would drop. Now the spatial shaping was somewhat restricted because it could not change

the divergence of the beam anymore.
The first realization we built had the spatial modulation before the temporal modulation. This led to the problems described above but after fixing them the spatial shaping influenced the way the laser hit the temporal section. By changing the spatial profile the positions of the spectrally dispersed beam on the LCD was shifted accordingly. This did not give the frequencies a fixed position on the modulation area and the algorithm was not able to produce reasonable results. The solution to this was simply to do first temporal then spatial shaping, because the shaping in the Fourier plane does not influence the beam profile in the far-field directly.

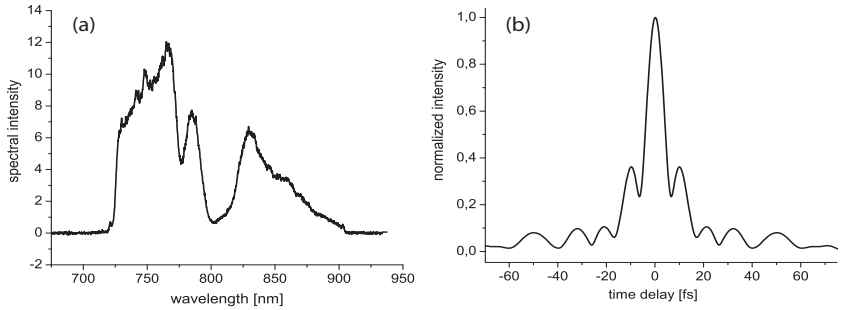

Figure 2.5: Spectrum (a) of the laser pulses after propagation through the fiber and the pulse shaping setup. In (b) is the Fourier-transformed temporal intensity distribution with a pulse duration of ca 9fs. The strong modulation of the spectrum causes the sidewings in the time domain.

The spectrum displayed in Fig. 2.5 was used because it showed a good long-term stability and allowed optimizations up to 1000 generations ($\sim 7h$). Sometimes minor adjustments were necessary to compensate the laser drift, but overall the reference is quite constant (see Fig. 2.6 (b)).
In Fig. 2.6 (a), one can see the two-dimensional phase mask that was found to be the optimum for a minimization of the pulse duration. The spectral shaping is done in the upper part where the wavelength is plotted and again one can see the stronger horizontal than vertical modulation like in Fig. 2.3. In the lower part the spatial modulation is performed and the circle indicates the center of the incident laser beam.

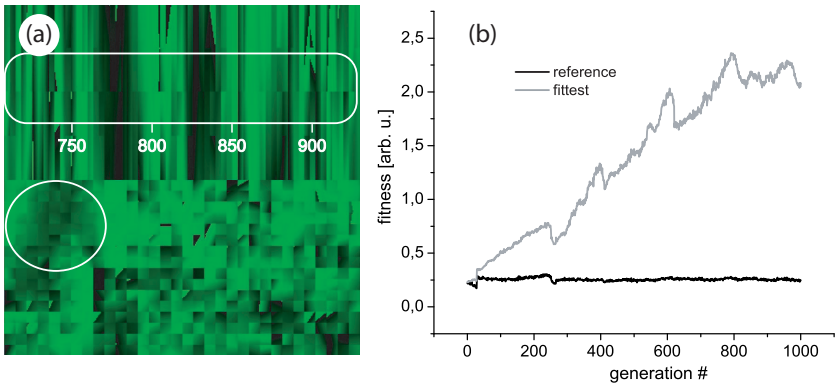

Figure 2.6: Phase mask (a) after the optimization with the goal of the shortest possible pulse duration. (b) is the fitness curve over the complete 1000 generations.

In Fig.2.6 (b) the fitness of the fittest individual is showing some dips at evenly spaced generations. This can be attributed to the doubling of the resolution at certain times. Because the mutation rate was controlled manually, after doubling the genes and not changing the mutation rate the whole population consisting of only 10 individuals was affected by some changes. This rate had to be changed by hand in order to prevent signal degradation. Later in section 1.4, it will be demonstrated that the modulation rate is best adjusted to the resolution whenever it is changed.

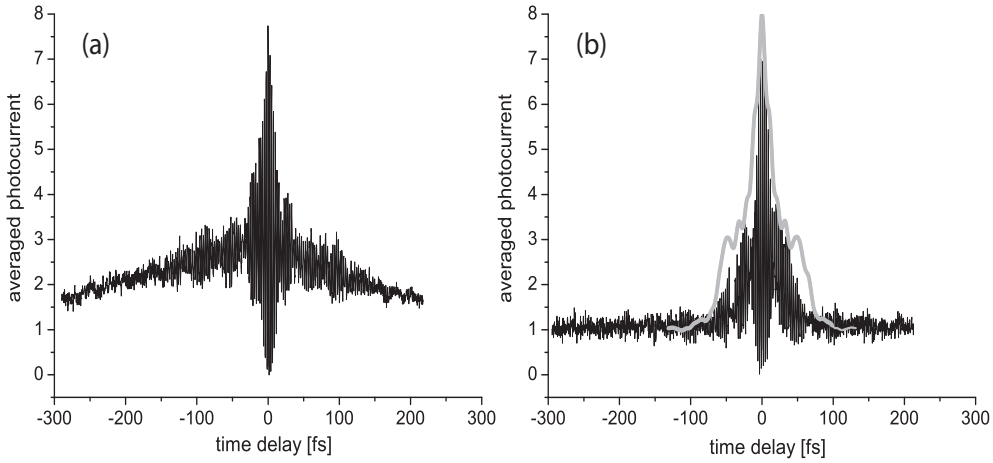

Figure 2.7: Traces of the interferometric autocorrelation of the reference laser pulse (a) and the spatio-temporally optimized pulse (b). Although the pulse durations are not very different (both about 11fs), unlike the fittest pulse, graph (a) reveals a strong background chirp. The grey line in (b) corresponds to the autocorrelation trace of the bandwidth-limited pulse from the spectrum in Fig.2.5.

In Fig. 2.7 two IACs of the reference pulse and the fittest pulse are presented, respectively. The strong quadratic chirp (giving the hill-like background structure in (a)) can be reduced significantly to an almost flat temporal profile. Only small wings in the fittest pulse are remaining and they are caused by a modulation of the spectrum as before in section 2.2.1. The pulse duration could be compressed to about the Fourier-limit which in this case is about 9fs. The fact, that our achieved pulse duration seems to be less than the bandwidth-limit is probably caused by suboptimal experimental conditions. For example, even though the spatial chirp could be minimized using this setup, it is still present. This is very likely to be the reason for the autocorrelation amplitude ratio to be not 8:1 as theoretically expected (compare section 1.3.1).
Another quite substantial problem is due to the setup and the SLM itself: Spatial modulation of a broad spectrum is problematic even if the reflectivity is still high enough. The LCD-based technique implies a wavelength-sensitive index of refraction and therefore two different wavelength at one spot undergo different phase shifts.

2.3 Optimization of the Filament

Since about 2004, many workgroups started investigating the use of femtosecond filamentation for pulse compression [8, 55, 56, 57, 58, 59]. Rarely, even self-compression of the laser pulse in the filament without any further compression device could be measured [60]. A main attraction of the filament is the ultrabroad generated spectrum that exceeds up to 2 octaves [61, 62] and could be created in air [63]. However, it is not the case that filamention is superior to the other technique but both have different advantages and disadvantages [64]. During the work in this field the two methods were applied but for simplicity reasons from this point on a filament in Ar is used as spectral broadening device if not stated differently.

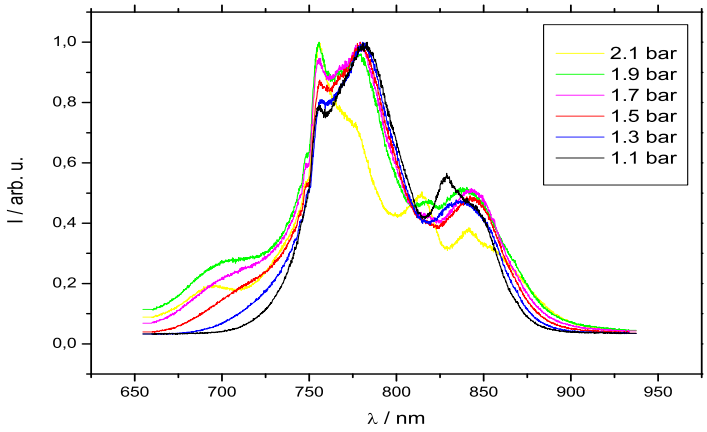

Figure 2.8: Here are several spectra after the filament in dependence on the Ar-gas pressure in the setup; one can see a distinct blue shift at high pressures. The used lens has a focal length of 1.0m.

Some typical spectra recorded after the filament are shown in Fig. 2.8. One can see that the spectral broadening (SPM) is larger with increasing gas pressure due to n_2 depending on the density of the medium. But the pressure can not be adjusted arbitrarily to match the desired spectrum because according to equation 1.18 the breakdown-intensity is also depending on n_2, but inversely proportional. When $P > 3 \times P_{crit}$, we know that multiple filaments can be seeded. Normally, this results in an inhomogeneous beam profile sometimes with an additional spatial chirp. We could easily examine the transition from no filament at 0 to $\approx$ 500mbar, to a single filament from about 500mbar to 1500mbar and then to multiple filaments at pressures above 1500mbar. Of course this depends on the pulse energy, which was set to $700 \pm 50\mu J$ for these observations. Since we are using a peak power of $\approx 25GW$ we would expect the beginning of multi-filamentation in air already at fairly low pressures of around 1.0bar. It is therefore important to note, that other parameters like beam characteristics (ellipticity [16], diameter [15], wavefront [17] or phase offset [65]) also have a strong influence.

In Fig 2.9 one can compare the different beam profiles after the filament in dependence on the gas pressure. Clearly the more homogeneous beam profile with only one intense

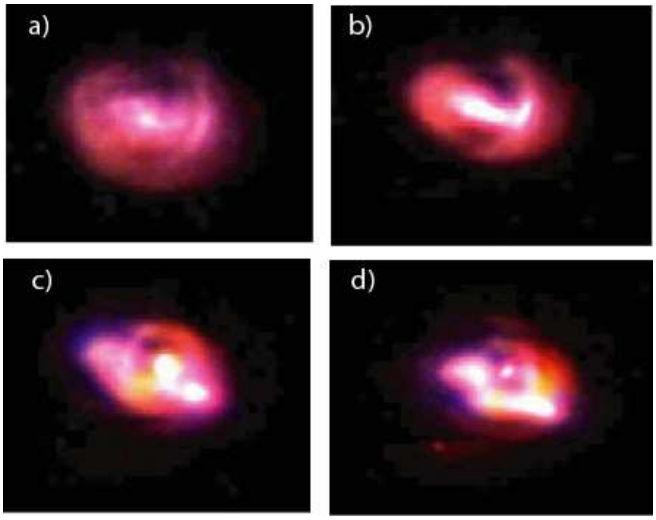

Figure 2.9: Beam profiles recorded after the filament at different pressures with same input power. The pressure in a) is 1000mbar, in b) 1300mbar, in c) 2000mbar, and in d) 2400mbar. The colors are recorded with a normal CCD camera with an IR-filter. There is a clear tendency from low pressures to high pressures that the intensity profile gets inhomogeneous and very un-Gaussian.

point (top left in Fig 2.9) breaks up into a distorted center and even multiple spots with equally high intensities occur (lower right in Fig 2.9). As mentioned in the caption, in Fig 2.9 the beam profile is captured with a low-resolution, commercial IR-insensitive CCD chip. To get a more detailed analysis and not be irritated by false-color representation, the crossections of the beam are plotted in 2-D in Fig. 2.10.

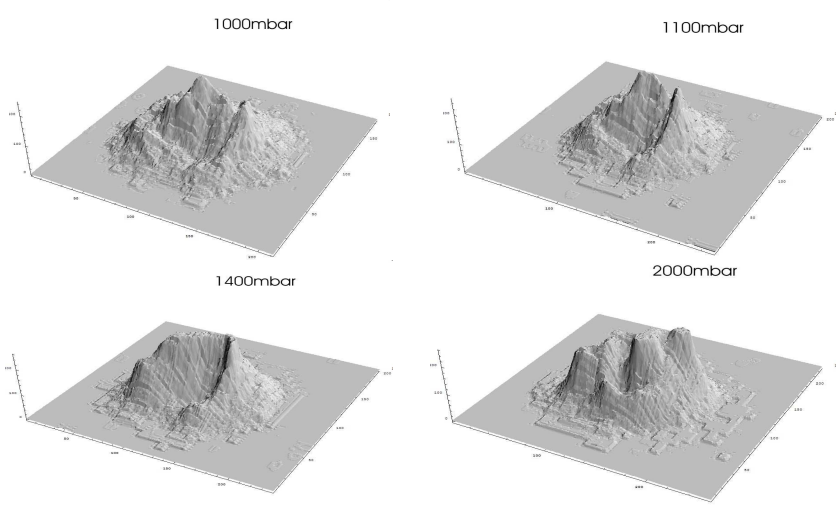

Figure 2.10: Analytical presentation of the beam profiles at different gas pressures. At 1000mbar only one central peak is visible, while at a slightly higher pressure (1300mbar) a neighboring peak grows largely. At 1400mbar the two peaks developed into a horizontally extended high-intensity region with steep slopes. At 2000mbar, there are clearly more focal spots indicating multiple filaments.

To summarize our results concerning multi-filamentation in dependence on pressure and laser power (although this is not shown here), we can sketch pressure versus laser power and get a schematic like in Fig 2.11.

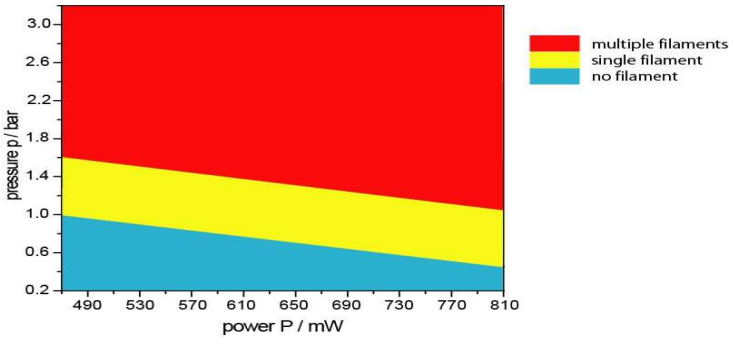

Figure 2.11: Simplifying map that shows our empirical findings on when multifilamentation occurs. There is a pressure/laser power region in which a single filament seems to be reasonably stable.

This is a purely empirical scheme based on the critical pressure/laser power at which the one-peaked profile turns into a 'smeared' peak and ultimately in many intensity peaks. For the map in Fig. 2.11 we observed the beam profile with a CCD camera and as soon as the single brightest spot started to blur or change in size, we noted the beginning of multiple filamentation. The lower limit is simply set by spectral broadening and white light generation, which is a typical indicator of a filament. One can see, that within a certain pressure 'bandwidth' (at a given laser power) we can expect no multiple filamentation and this is the regime where our future optimizations will be performed. Naturally, the transitions from no filamentation over a single light filament to multiple filamentation are not as well-defined and sharp as shown in Fig. 2.11.
Note that the very broad spectra shown in Fig 2.8 are all within the multi-filamentation regime on this map. This demonstrates again, that after dramatic spectral broadening in a filament with high gas pressure one cannot use the complete beam for further experiments. How to prevent or at least limit this inhomogeneity is shown in section 2.3.2.

For our application of the laser pulse we need a Gaussian-like (see section 1.2.5) beam profile that is easy to focus. In order to measure the focusability of our spectrally-broadened pulses we used an M^2 measurement: The laser is focused and at various points along the axis of propagation the beam profile is recorded. These beam profiles are then analytically fitted with a Gaussian to get the FWHM at the different z steps (see Fig. 2.12).
The computed M^2 parameter from Fig 2.12 before the filament is 1.18 ± 0.91 and after the filament is 1.21 ± 0.36. One can see that the error is comparably high (keeping in mind the least possible M^2 value of 1.00) but the main information is that the laser modes do not change enough to influence the focusability in a negative way. So even if the computed M^2 values are not correct, we can definitely conclude that the modal structure after the filament is not significantly worse.
For analysis of this data we used the software *Origin* which performed the nonlinear fitting with the Levenberg-Marquardt algorithm [66, 67]. This fit also gives errors of the fitting parameter M^2 which are the errors named above.

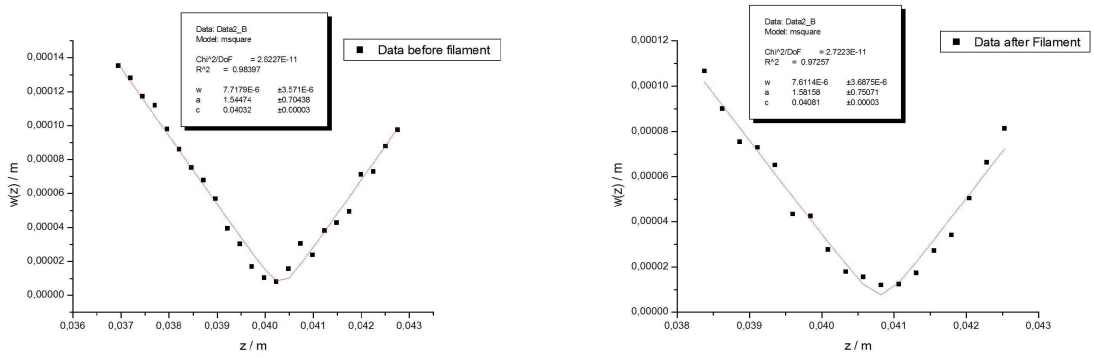

Figure 2.12: M-square measurement conducted before and after the filament. Each plot shows the beam waist (FWHM of a beam crossection) versus distance and a fit to compute the M-square parameter.

At the beginning of section 2.3, the high transmission of the filamentation technique in contrast to SPM in gas-filled hollow-core fibers is mentioned. The following experiment is straightforward: We detected the laser power immediately before and after our gas-filled tube, calculate the energy throughput and it shows the overall very high throughput in our pressure regime (Fig 2.13).

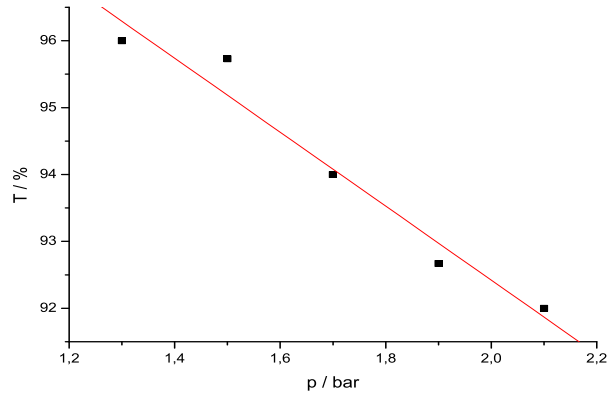

Figure 2.13: Energy throughput plotted versus gas pressure. The higher the gas pressure the more absorption takes place and less energy is transmitted. But even at $p = 2bar$ the transmission is larger than 90%.

In contrast to spectral broadening with hollow-core fibers where transmission is at most $50 - 60\%$, with the filament losses $< 5\%$ are possible if the correct single-filament regime is used.

2.3.1 Temporal Shaping

In Fig. 2.14 a schematic illustration of our setup is shown. Our laser beam is focused using a 1.3m focal lens into the gas-filled tube. Here SPM (1.2.3) broadens the spectrum and provides the possibility to decrease the pulse duration. With a grating it is possible to separate the different spectral components and via a cylindrical mirror each wavelength is focused onto the SLM. Because the pulse shaper is placed in the Fourier plane a very high spectral resolution for modulating the phase can be realized.
In the normal temporal shaping setup only one dimension (the horizontal one - vertically, every pixel has the same phase value) of the active area is used.
As described before, we can now apply arbitrary phases to selected wavelengths in order to shorten the pulses. After the SLM the spectral components are recombined using the same grating and the final laser pulse can be characterized with the SPIDER technique (1.3.2).
Since we have a resolution of 768 vertical lines with each having values from 0 to 255 (corresponding to zero to two pi, respectively), a lot of computing power is needed for optimization. Basically there are two methods to optimize the pulse duration with this setup: First one can maximize a signal that is inversely proportional to the pulse duration (e.g. the second harmonic signal [50, 51]) or one can analyze the spectral phase and apply it with opposite sign to the phase shaper. While the first idea is usually realized with a time-consuming evolutionary algorithm (reference) we decided to choose the seemingly more efficient way of applying the inverted phase to the SLM. To compare this method with the well-established optimization via evolutionary algorithm we did such an 'unguided' optimization as well and this will be described at the end of this section.

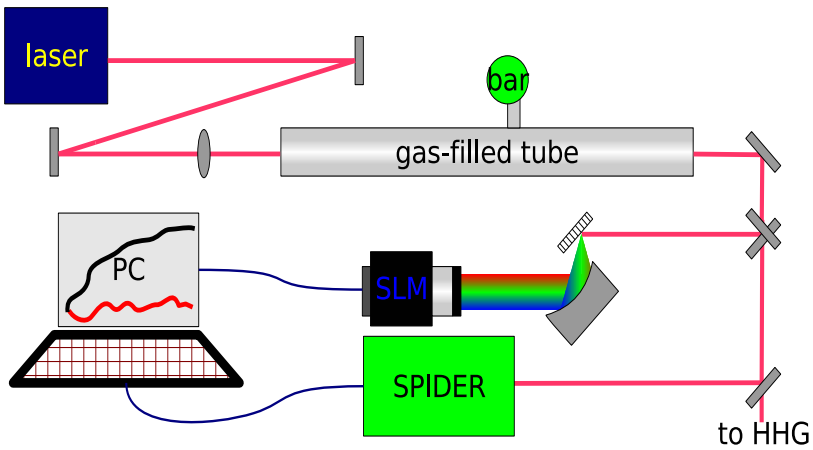

Figure 2.14: This setup shows our compression stage using filamentation and the SLM as a variable dispersion compensation device. After SPM in the gas-filled tube we use a grating to separate the different wavelengths and then image them onto our pulse shaper. The success of this shaping is monitored by a SPIDER from where spectral phase and intensity is given to a PC. Here we use an evolutionary algorithm to improve the shaping process in a closed loop.

One problem we quickly faced was that it is nearly impossible to measure the spectral

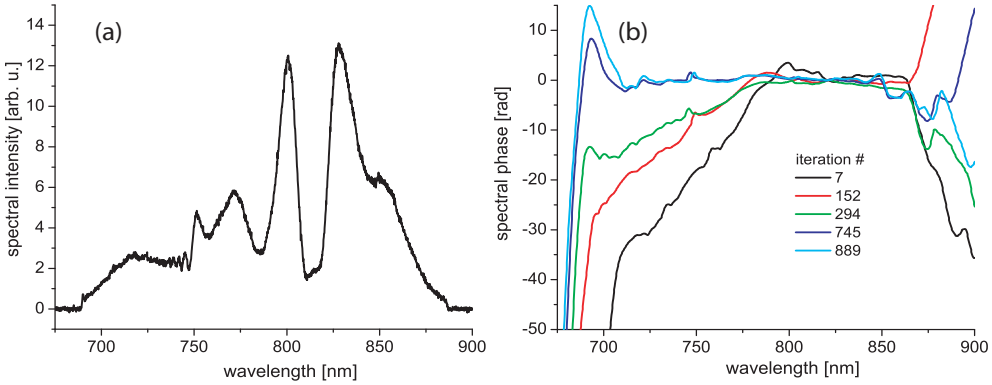

Figure 2.15: On the left one can see the measured spectrum after spectral broadening that can be used for our compression experiment. On the right the spectral phase is plotted versus wavelength and at different iterations.

phase at high resolution and then apply it inversely to the corresponding wavelength in one iteration. An easy way to solve this was to do it in several 'steps'. The initially measured spectral phase is inversely applied to the pulse shaper, the result is measured with SPIDER and from this result a new phase mask is computed. The first iterations turned out to approach a flat phase quite fast but not very accurately but with enough repetitions and smaller phase corrections the resulting phase begins to get comparably smooth.
In Fig. 2.15 the result of this experiment is presented. The left part (a) shows the measured spectral intensity used for this compression and the right part (b) shows the spectral phase after different iterations. While the initial phase features a clear edge at 790nm, it is possible to correct this to a more smooth and flat phase as desired.

The driving force behind these experiments was to generate as-short-as-possible pulses with the given spectra while maintaining a well-enough beam profile. Although the spectral phase in Fig 2.15 is reasonably flat the spectrum is quite modulated which results in pre- and postpulses in the time domain. Thus we decided to use a not-so-broad spectrum to get short pulses with a very good temporal structure (see Fig 2.16). Here the initial phase is not as bent as in Fig 2.15 and the phase could be corrected in a way that its deviation is smaller than $\frac{\pi}{6}$ from 740nm up to 860nm. This resulted in a pulse as short as 15 ± 1 fs without any noticeable pre- or postpulses. The latter is very important for harmonic generation since the ionization potential is changing dramatically for pre-ionized atoms. The Fourier-limit of this spectrum is slightly below 14fs FWHM, which is in good agreement with the result from Fig. 2.16 b). The phase oscillation at about 790nm could not be corrected, even if the applied phase was manually optimized. That was the last part of this work: We did modulate the phase manually to optimize the pulse duration. We simply applied a phase at a certain (estimated) wavelength and watched the result via SPIDER. Step by step it was possible to flatten the phase very much like before. As expected, this yielded no shorter pulses than after iterative computer-assisted optimization while being much more time consuming.

For the second approach we used the evolutionary algorithm to maximize the photo cur-

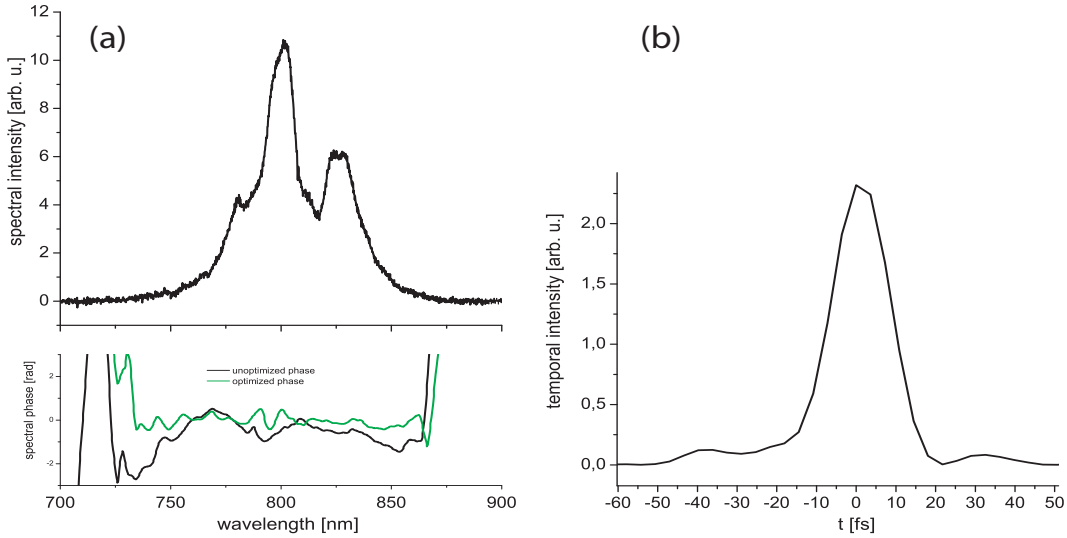

Figure 2.16: In (a) the spectral intensity (in the upper part) and the spectral phase (in the lower part) are plotted versus wavelength. Part (b) shows the resulting temporal intensity of the laser pulse. The duration is ≈ 15fs with almost no pedestals before and after the pulse.

rent of a GaAs diode, which bandgap corresponds to two-photon absorption of 700nm to 900nm photons. Here we had the problem of one-photon excitation resulting in a signal (photo current) from the diode because of a too broad spectrum. As seen before in chapter 2.8, we have a lot of blue shift which results in spectral components down to 400-500nm even in the single-filament regime. This is significantly different after using a gas-filled hollow capillary, where the spectrum broadens symmetrically around the fundamental wavelength (800nm). Although there is not much spectral intensity below 600nm after the filament, it is enough to create disturbing one-photon excitations.
Nevertheless, some optimizations of the pulse duration were performed by simply using the signal from the GaAs diode as fitness. Here we used an evolutionary algorithm to let it find the (global) maximum of the fitness. Thus the SPIDER setup is not used directly for the optimization, which can be regarded as an advantage because of its complexity and sensitivity to misalignment.

2.3.2 Spatial Shaping

As we have seen in Fig. 1.3 (a) and in Fig. 2.10, while filaments feature strong SPM they also clearly distort the beam profile.
One can not only see the not-so-radial-anymore intensity distribution but additionally different spots of the wave front have differing spectral intensities. We refer to this as a 'spatial chirp' because here various wavelength differ not in time (as in 1.4) but in space. This posts a serious problem because if the spectrum varies over the wavefront, the phase and thereby the pulse duration is also not constant over the whole pulse front. We measured this by placing a pinhole before our SPIDER spectrometer and roughly scanning the laser beam in 3x3 positions (see Fig. 2.17). A complete SPIDER pulse characterization is not necessary in such a situation, because the spread-out spectral components make such a laser pulse useless in terms of temporal compression and HHG.
Since the goal was to achieve similar if not identical spectra over the whole pulse front

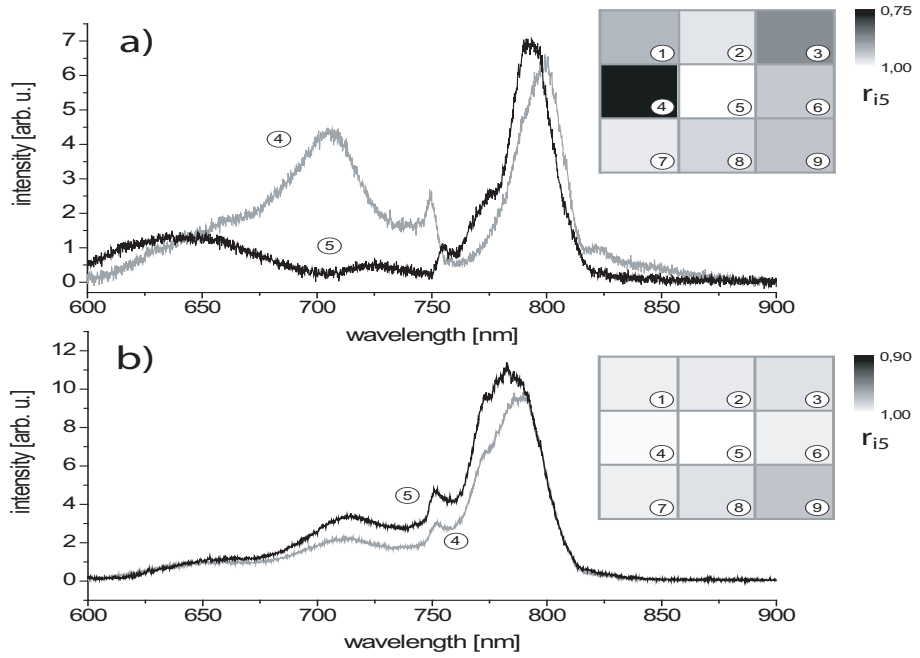

Figure 2.17: Spatially-resolved spectra of our beam profile. On the left are two spectra measured at the positions 4 and 5 from the schematic beam profile on the right. a) shows the original state and b) is the optimized case achieved with setup in Fig. 2.18.

and have a smooth Gaussian-like intensity distribution we changed our setup from section 2.3.1 a little bit. Instead of adaptively shaping the spectral phase like in Fig. 2.14 we moved the SLM before the filamentation tube in order to influence the wavefront before any distortions (see Fig. 2.18).

Due to the highly nonlinear interaction processes within the ionized gas it is unfortunately not possible to simulate the pulse propagation exactly [68]. Again, we employed our evolutionary algorithm to find the unknown ideal spatial phase that should result in a more homogeneous and not spatially-chirped output of the filament. We give the beam profile as an input parameter to the algorithm and let it modulate the phase front until the input parameter is considered to be much fitter. The fitness was computed from each recorded image by integrating the intensity in x and y direction (both orthogonal to the propagation axis). These 'profiles' were fitted with a Gaussian to compute a 'center of intensity' from the two Gaussians central coordinates. From this center of intensity we defined four quadrants in the four directions from the center (top left, top right, bottom left, and bottom right). Now the last step was to count the impinging photons in each quadrant and relate the four intensities to one another. Of course, with an ideal Gaussian beam profile all four quadrants should receive the same amount of photons. So our fitness was a measure of the inequalities between the four quadrants and needed just one more additional parameter to provide good results. Obviously, the beam profile before the filament was homogeneous and not spatially chirped. So the best logical solution for the SLM was to prevent a filament and let the laser beam propagate undisturbed through the gas-filled tube. To 'force' the phase shaper to maintain a filament, we used the blue part of the spectrum that clipped at the prism compressor. This blue part had to have

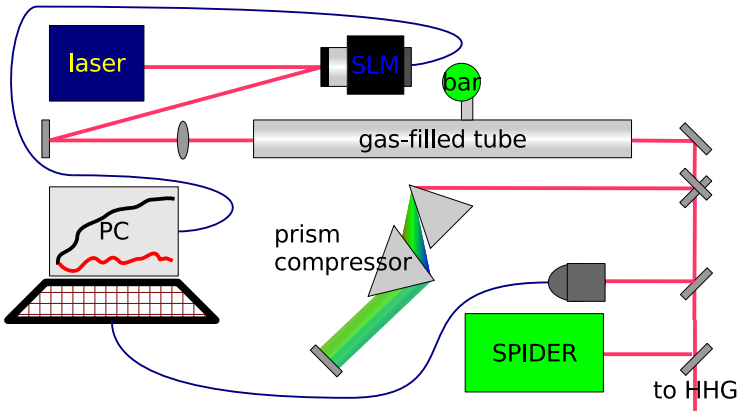

Figure 2.18: Modified setup where the first mirror after the laser system is replaced by the SLM to perform spatial shaping of the wavefront. This time the pulse compression is done in the prism compressor and after this a IR-sensitive CCD camera captures a beam profile. This beam profile is used as a feedback for the evolutionary algorithm on the PC. SPIDER provides the pulse characterization as before.

a certain intensity (measured with a second CCD) to produce 'fit' solutions in terms of phase masks. This way, the algorithm could modulate the beam completely as long as a filament was present.
The described fitness definition is insensitive to different wavelengths which are at least part of the problem as described earlier. However, if all incoming photons - regardless of their energy - are spread like a 2-D Gaussian, it is a fair assumption that the different frequencies are homogeneously spread over the whole beam profile. Therefore monitoring the beam profile with just a black-and-white CCD should be sufficient.

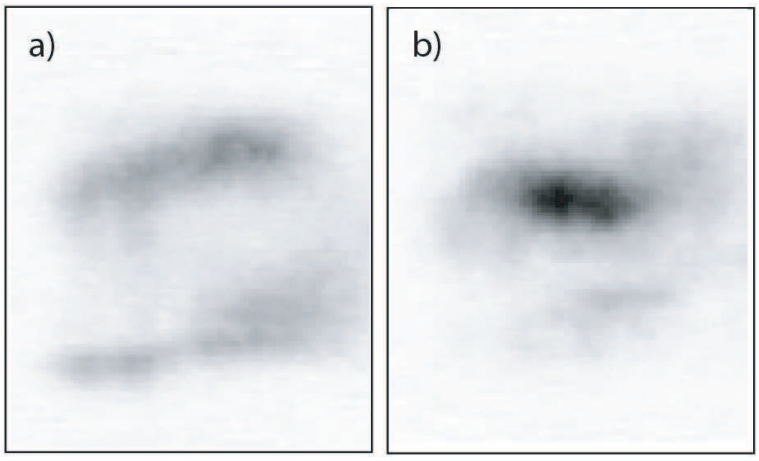

Figure 2.19: This is the beam profile recorded after the filament and the compression stage. On the left is the non-optimized case where the highest intensity is in two distinct stripe-like regions. After the optimization with an evolutionary algorithm the intensity is much more concentrated in the center and thus much more Gaussian.

In the experimental realization, our IR-sensitive CCD camera (Sony XC-ST 50) records

the beam profile after the compression stage. That means, we do not only correct inhomogeneities after the filament but also those created by possible nonlinearities within the prism compressor. Of course, there is only very little adjustment of the latter. One has to make sure that the prisms are aligned for minimum deviation and consist of low-dispersive material (in our case FK5), so that not too much third-order phase terms is added onto the spectral phase of the laser pulse. Our prism compressor has an apex distance of 1m. Since the interaction with the filament should generate mainly a quadratic phase, we tried to compensate this with a prism compressor. This allows for positive and negative phase compensation as opposed to a grating compressor, which can only introduce a negative quadratic phase.
Shaping the wavefront before filamentation does have many advantages. First of all, the spectrum is not yet broadened so that the reflectivity (see section 2.1) is higher than 90%. Not less important is the fact, that the highly nonlinear processes within the filament seem to depend strongly on distortions of the initial wavefront. Thus, it is feasible to shape the filament rather than to try to compensate the inhomogeneities afterwards. The third - and very technical - reason is that the beam diameter right after the laser output is comparably large and exactly fills the active area of the SLM. After the filament the beam divergence is so low that the laser is quite collimated for some lengths. Comparing the beam profile recorded with our monochrome, IR-sensitive CCD before and after the optimization, one can clearly see an improvement in the intensity distribution (see Fig. 2.19).
Even more important for us is the result shown in Fig 2.17 b. Here the difference between the spectral changes over the beam profile is very pronounced. While in the upper part (Fig. 2.17 a) the spectra differ quite a lot from position to position in the lower (optimized) part this spectral differences are much smaller.

We can conclude that it is possible to compensate the spectral chirp after filamentation by adaptively modifying the wavefront before the filament. The throughput remains very high and only the spectral broadening is a little limited due to the restriction to stay in the single-filament regime. Nevertheless pulse duration of around 10fs with pulse energies of $> 600\mu J$ can be realized.

2.4 Improvements of the Evolutionary Algorithm

As was presented before (see section 1.4), evolutionary algorithms are metaheuristic optimization procedures that are inspired by biological evolution. This means that solutions to the specific problem play the role of individuals in a population while every individual includes a set of parameters. Such parameters can be binaries (genetic algorithm) or arbitrary numerical variables (evolutionary algorithm). One major part of these algorithm is the definition of the fitness. In our case, the fitness could always be measured experimentally and thus it is easy to compute the specific fitness of one set of parameters (one individual).
To improve the solutions from one generation to the other, the population undergoes certain changes such as cloning (the 'fittest' individuals are copied), mutation (minor changes are applied to the top individuals) and crossover (two of the 'fittest' individuals mix). After every generation the fitness of this 'new' population is evaluated and the individuals are sorted accordingly. Then the cloning-mutation-crossover-step follows and this continues until a maximum is found. What is special about this algorithm is the fact that it does not necessarily work very fast but it is quite robust against experimental noise and can find its way out of local maxima due to mutation. For a genetic algorithm there is large probability for it to find even the global optimum because of its finite parameter range. Every evolutionary algorithm has a set of parameters that are changed continuously in order to approach the optimum. The first step is the correct parameterization, for example in the setup shown in Chapter 2 each individual corresponds to a phase mask on the SLM. In doing so, each individual is linked to the pulse duration (optimization value) via a Fourier transform. In the spatial shaping setups a certain individual stands for a certain wavefront modulation. The improvements described here are due to a 'learning curve' of the experimentalists on how the parameters of the algorithm should look like at what part of the optimization process.
In this section, our useful adaptions of the evolutionary algorithm are presented and explained and in the next part of this chapter some simulations were performed to verify our assumptions. As briefly mentioned above the mutation rate is a critical parameter and in our case it is linked to the 'resolution' of our optimization space. Since our SLM does have a large amount of pixels this not only gives us a high resolution but also demands a lot of computing power. For our algorithm to be able to run on workstations we have to limit our resolution to about a tenth of the physical 768x768 pixels.

Planes instead of pixels

Because we could not use the complete resolution in pixels due to computational restrictions our fist approach was to define 'meta-pixels' that extend over for example 8x8 or 16x16 physical pixels. This decreases the computer's load but we threw away our high resolution. Therefore the next idea was a parameterization of the wavefront not in meta-pixels but in planes of the same size. These planes are numerically much easier to characterize (total of 3 integers per plane) while they incorporated all physical pixels. This is illustrated in two dimensions in Fig. 2.20 where on top always ten pixels share the same value and therefore have the same shade of green (on the left). On the lower part, the pixels are replaced by planes and a much smoother surface can be generated (again on the left). The sharp black-green transitions in the planes are caused by modulo phase shifts. Since phase differences larger than 2π over the whole phase front need to be possible, every plane has a fourth 'gene' that carries the information at which phase offset

a wrap to 0π takes place. For any wavefront application apart from being numerically

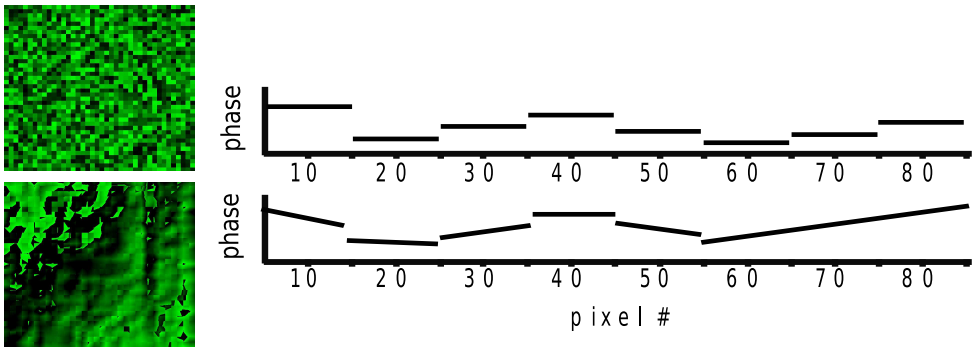

Figure 2.20: Simplifying model of the difference between parameterization by pixels or planes. On the right is a side view onto one row of pixels (top) or planes (bottom) and on the left the corresponding full 2-D phase shape. While the right part is only schematic, the left images are from real optimizations.

less demanding, the planes also provide a smoother phase modulation which is in general favored by the laser pulse. In some applications, an additional 'smoothing parameter' in introduced: The mutation probability for one plane to mutate 'closer' to the rim of another plane can be raised above the probability to mutate further apart. As will be shown in section 2.4.1, this is not always a good feature of the algorithm but partly it may speed up the optimization process.

Stepwise increase of the resolution

Another big step towards a more time-efficient procedure leads us to a dynamic increase of the spatial resolution. It is easy to see that, especially for planes, some very large units at the beginning getting the correct orientation can be of great benefit for the ongoing optimization. If all planes get a fundamental orientation and start deviating from this, of course, it is less time-consuming than letting each plane 'find' its basic alignment by itself. Our implementation is described in Fig. 2.21 below:

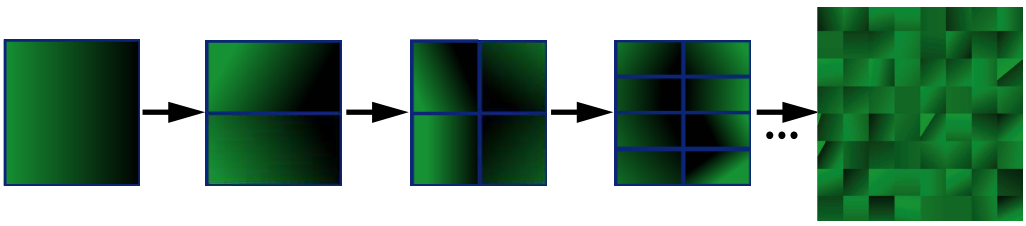

Figure 2.21: A single large plane at the beginning (left) is divided into smaller and smaller fractions. Each new plane is starting with the tilt of the original larger plane and then develops to whatever position is best.

In the next section one will see that a dynamic increase of the resolution is absolutely necessary for every optimization performed in this work. But it is only in the simulations in 2.4.1 where an automated doubling of the planes is implemented. In the experiments using this algorithm, the resolution was increased manually.
What is important to note is the fact, that the absolute mutation rate is strongly coupled to the resolution. If the relative mutation rate refers to the changed fraction among

the complete amount of genes, increasing the genes per individual has a direct influence on the resulting overall mutations. This number has to be within reasonable boundaries as explained in section 1.4. Again, for the following simulations, the mutation rate is a function of the current resolution while in experiments this was adjusted manually.

2.4.1 Simulations

The work presented in this section is purely theoretical, because is was done on computers only and does not include typical experimental difficulties and sources of errors. Nevertheless, it has a strong connection to the experiments conducted since the problem solved is generally helpful for all phase shaping devices.
To test our adaptions of the evolutionary algorithm, we defined a certain high-resolution picture as the ideal phase mask and let the algorithm find the optimal solution. In order to take different 'ideal' phase masks into account, we selected three very unlike images as shown in 2.22:

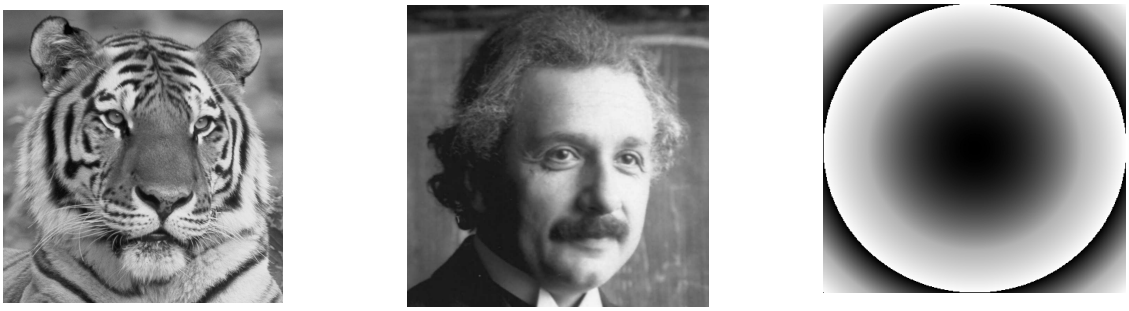

Figure 2.22: Three sample images that are each set to be the ideal phase for an optimization. While the tiger features strong contrasts and very little background, Einstein has a moderate contrast and a lot of blurred background, and the parabola is a low-contrast, SLM-typical shape with very smooth transitions.

As explained in the caption of Fig. 2.22, these three samples feature each different characteristics. From this we want to analyze which algorithm settings are universally good and which are just helpful at specific questions. In the following part, each picture will be set to be the optimal phase mask and the evolutionary algorithm has to match this given mask as good as possible. Only in this section, the fitness is not measured experimentally but computed from the difference between original and simulated image. Thus the fitness value itself from the three images is not comparable but should only be compared relative to the reference. As usual in our experiments, the reference (not shown in the graphs) is measured once per generation by applying a blank phase mask. One more important fact is the number of planes/meta-pixels used for this comparison: We chose to use 64x64 meta-pixels in the highest resolution stage of the algorithm but only 32x32 planes. This is because one meta-pixel only needs one numerical value while one plane is characterized by four numbers (three points and the modulo offset). So four meta-pixels demand approximately the same computational resources as one plane, which in both cases is exactly at the limit of our work stations. This means: employing our single-core, 2GHz, 1GB-RAM laboratory computers, the maximum computable resolution of planes is 32x32 and of meta-pixels is 64x64.

Tiger

Starting with the image of the tiger we can see the simulation results displayed in Fig. 2.23. With the naked eye, the tiger face that consists of meta-pixels seems to come closer to the original from Fig. 2.22 and the plane-based image appears less similar.

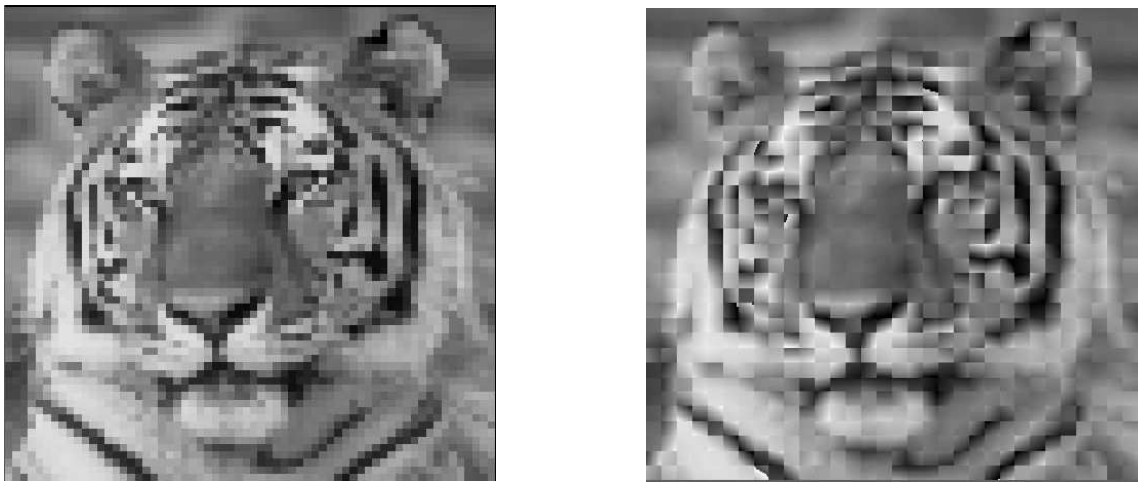

Figure 2.23: On the left is the Tiger's face displayed by meta-pixels and on the right by planes. Qualitatively, one can see a more detailed and sharper picture on the left while the right one seems a bit blurry and with lower resolution. The quantitative evaluation will confirm these results.

Because such a subjective comparison is not necessarily correct, we want to look at the optimization curves as well. In Fig. 2.24, our results of the different optimizations are given.

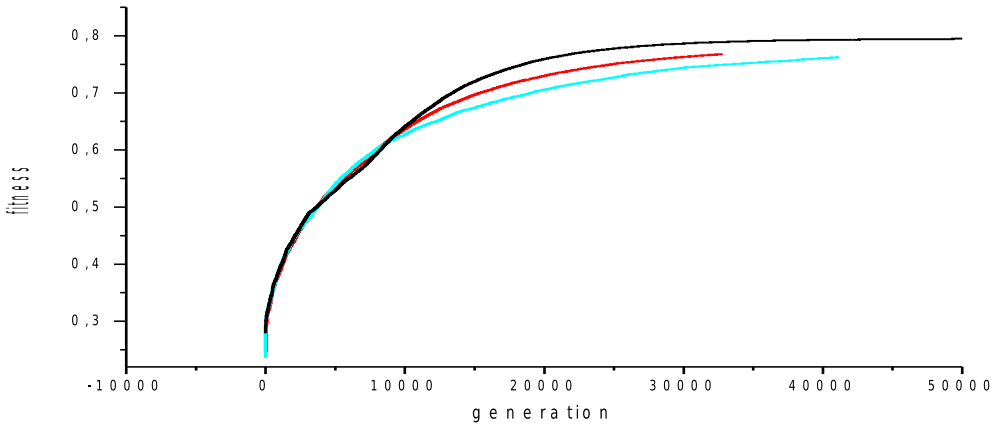

Figure 2.24: This is the plotted fitness of the optimization using meta-pixels (black), planes (red), and planes with additional smoothing (grey) all versus the number of generations. The fitness is in arbitrary units.

One can see that the meta-pixels and planes are rising together until after 10k generations the meta-pixels are in better agreement with the original picture. The planes seem to be at a disadvantage here and especially planes that have a strong tendency of building flat surfaces (smoothing, as explained above) cannot compete with the meta-pixels.
The discrepancy between a clearly better meta-pixel image that only has a $\sim 5\%$ higher fitness can be explained by a trick our brain plays on us. A higher resolved image appears to be more accurate and reveals more details, which is the case for the meta-pixel optimization. However, also more details are introduced that might not be in agreement with the original picture. Thus, the objective advantage of high-resolution meta-pixels over low-resolution planes *can* be smaller than expected.

Einstein

Now the next picture, the one of Einstein in 1913, will be regarded. In Fig. 2.25, both final results are shown and here it is already a little harder to tell which one is more similar to the original. Therefore, a qualitative analysis with the optimization data (see Fig. 2.26) is conducted below.

Figure 2.25: On the left is Einstein's face displayed by meta-pixels and on the right by planes. Again, the meta-pixels reveal more details but also show some quite pixelated areas.

Here, after 2k generations the planes' fitness is rising faster than the meta-pixels' and both planes (grey and red) end up with a higher terminal fitness. Interestingly, the dynamic smoothing seems to boost the planes advantage a little more, even though the two converge after $> 50k$ generations. The dips in the fitness curves, especially the black one, are caused by a doubling of the genes of the individuals. It is normal, that after so many new free parameters are added the system takes some time to improve again - even if the mutation rate is properly adjusted (compare with 2.2.2). The dynamic smoothing, meaning that the smoothing parameter is a gene itself and optimized accordingly, provides a very smooth optimization curve. It is understandable, that this technique, which did not provide good results for the tiger with its high contrast modulation, works better for Einstein's picture.
The two static-mutation-rate graphs are no real competition but nontheless reveal inter-

esting behavior. A larger mutation rate of about 40% starts much quicker than the one with 15% due to its faster mixing of the genes. But in the end, too much change is preventing to come close to the optimum and so the lower mutation rate is advantageous on the long run.

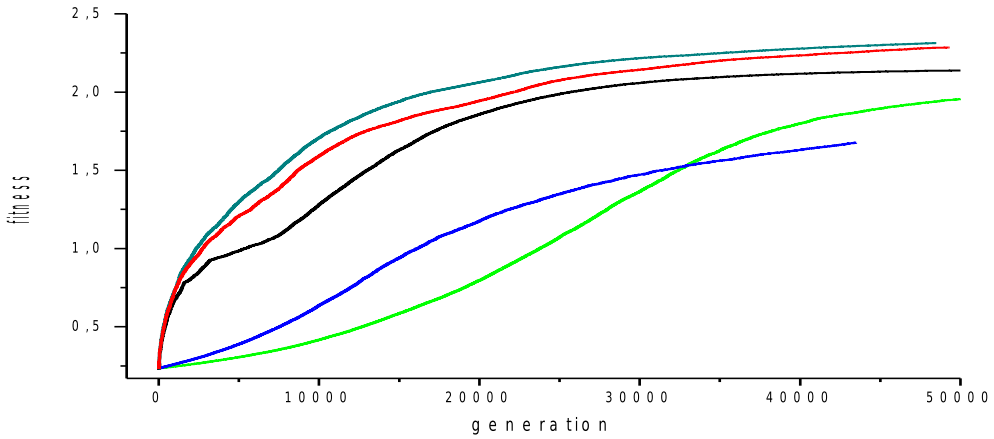

Figure 2.26: This is the plotted fitness of the optimization using meta-pixels (black), planes (red), and planes with additional dynamic smoothing (grey). Also, optimizations with a fixed mutation rate are shown in blue and in orange, with 40% and 15% mutation rate, respectively.

Parabola

The last sample is a two-dimensional parabola that would result in a slight focusing if applied to the pulse shaper. The two final results are shown in Fig 2.27.

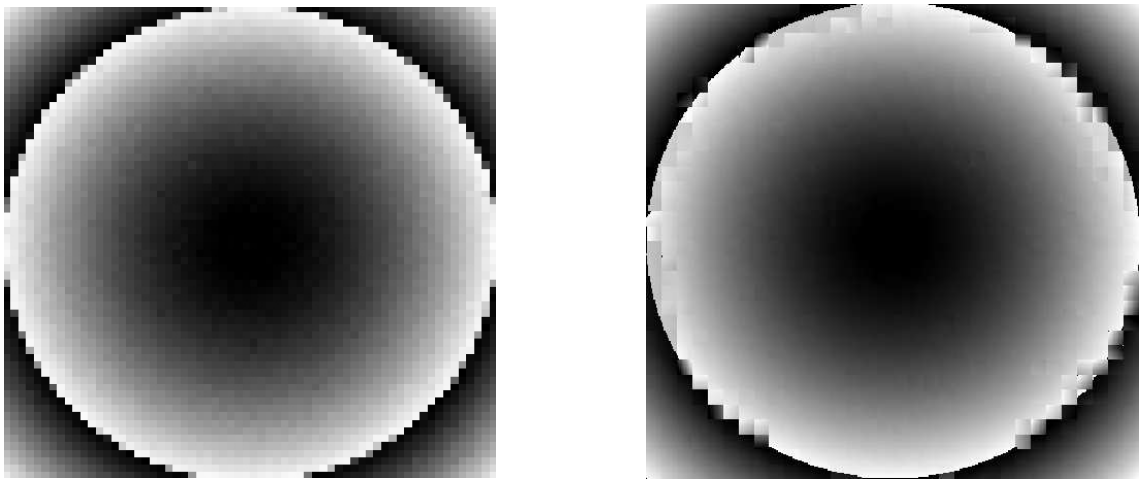

Figure 2.27: On the left is a 2-D parabola displayed by meta-pixels and on the right by planes. The meta-pixels are clearly giving a much more pixelated result while the planes manage to display the given shaped nearly perfect.

To confirm the visual impression, we look one last time at the optimization curves in Fig. 2.28. The impression from the images is confirmed by the graphs because the planes show a much higher increase of the fitness beginning at ≈ 1k generations. The pixelated parts from the rim of the parabola (caused by a modulo phase jump) where a smooth circle is not yet formed *can* be properly sampled by the planes and not by the meta-pixels. The ongoing rise of the fitness indicates, that the three areas in Fig. 2.27 (right), where the circular line is disrupted, could also be corrected on the long run. Also, the gradient in the central part of the parabola is much more homogeneous when displayed with planes. The optimization that started with 32x32 planes right from the beginning (grey in Fig 2.28) converges to a much lower fitness value than if the resolution is increased dynamically. This is hard to explain, since an evolutionary algorithm should always find the optimum - in a disadvantageous case infinitely slow. We guessed, that the planes are simply aligning so slow that our 50k generations are not nearly enough time.

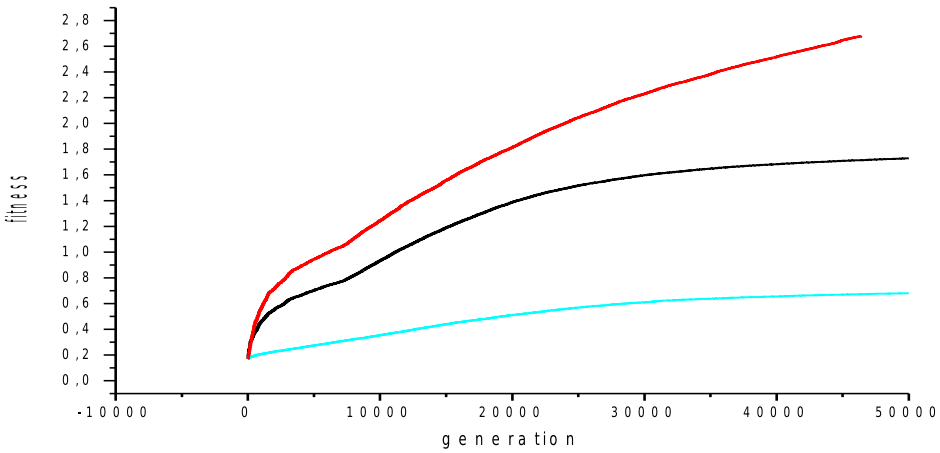

Figure 2.28: This is the plotted fitness of the optimization using meta-pixels (black), planes (red), and planes with a static resolution. Unlike the meta-pixels, the planes seem to rise continuously even after more than 50k generations.

2.4.2 Conclusions

Since this is the only theoretical part of this work, a few concluding statements are added to sum up the impression we got from the optimizations. More simulations than presented here were conducted, but for the basic message the shown data should be sufficient. First, it is clear that a stepwise increase of the resolution is maybe not necessary but helps to accelerate the optimization process significantly. The planes are - as expected - not advantageous in every situation BUT there are indications that smooth surfaces, that are likely to be our goals, are better sampled. Smoothing is definitely not a necessity and it can even inhibit the optimization but there are cases in which it helped to get to the optimum.
To set these simulations in the right context with our experiments, it is worth mentioning that due to experimental reasons rarely more than 1000 generations are used. This already corresponds to a time of about 3-5h in which the laser should not shift at all. And these optimizations are only preparations for high-order harmonic generation (see Chapter 3)

and so they should not be too time-consuming. In section 2.2.2 is was also mentioned, that our amplifier systems has a long-term drift and this is another reason to accelerate the optimization algorithm as good as possible.

Chapter 3

High-order Harmonic Generation

When an ultrashort laser pulse interacts with gaseous, fluid or solid matter, part of the radiation can be converted into higher frequencies. Since this generated radiation carries multiples of the original photon energy, the conversion process is called harmonic generation. Second-harmonic generation (SHG) is a quite common phenomenon, that is used for example in microscopy [69] or in our interferometric autocorrelation setup (Fig. 1.7). When higher orders of this frequency conversion are meant, this is called high-order harmonic generation (HHG) and its details will be the subject of this chapter. In chapter 4, some experiments with HHG are presented and characterization methods described.
Harmonic generation in a way is the ultrashort and coherent continuation of the X rays discovered 1895 by Wilhelm Conrad Röntgen. Just like there are many applications today for X rays, its much less intense but temporally more precise counterpart reveals a lot of potential applications. It is not the case that no other technique is competing with HHG in this field, but no other light source can combine the classic laser properties such as high temporal and spatial coherence and brilliant time resolution with the short wavelength of X rays. Additionally, no other source of ultrashort, coherent near-X-ray radiation can be generated with a tabletop system. The shortest man-made events today are light bursts as short as a few hundred attoseconds that are also generated via high-order harmonic generation [24, 25, 26]. But one downside of the frequency conversion is its efficiency of less than 10^{-4} and down to 10^{-8} depending on the energy regime [70, 71]. Also, up to now only harmonics up to 3keV have been generated [1, 2] from 800nm-fundamental-wavelength lasers and that only marks the beginning of X rays. Thus being a relatively young field of research, there is still some need for scientific work before HHG-setups can be used commercially.

3.1 Process of HHG

High-order harmonic generation was first described in the late eighties [72] when it was discovered, that with increasing order the conversion efficiency behaved somewhat strange: In the perturbation regime it falls linearly with energy as expected but then at even higher energies a region of quite constant conversion efficiency ('plateau') exists that ends in a cutoff. This is shown in Fig. 3.1 where one can also see the second oddity about harmonics: For many materials there are only odd harmonics to be generated while even harmonics are suppressed. This will be explained in detail later in this chapter. The use of a filter as in the right part of Fig. 3.1 is a very convenient tool to select specific spectral

components from the generally very broad harmonic spectrum. We are using Al and Zr filters later in this work, they mainly help to separate the fundamental IR beam from the generated soft X rays.

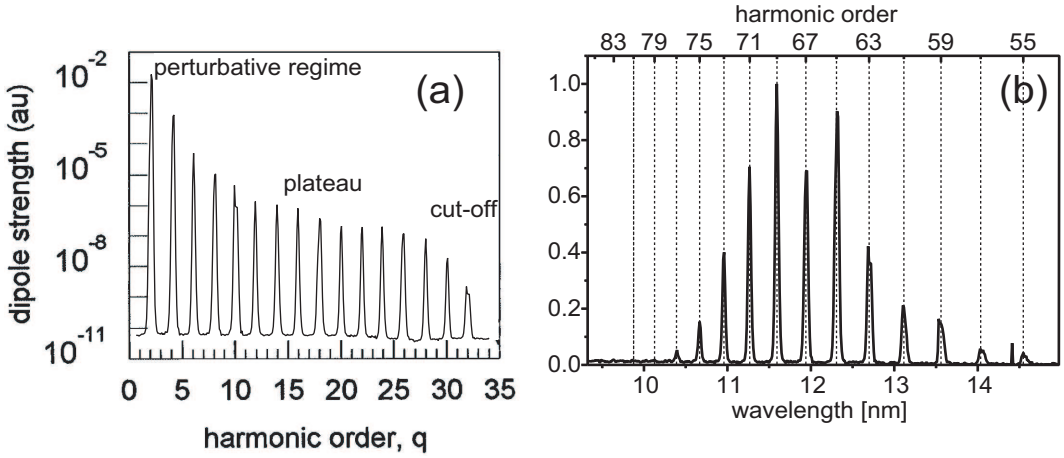

Figure 3.1: On the left is a computed HHG spectrum with no filtering. One can see the perturbation regime and the plateau that stretches up to the cutoff at the 33th harmonic. In the plateau, the harmonics reveal a nearly constant intensity over a large energy band. The highest energies can be gained from the cutoff-harmonics. The right graph shows a filtered spectrum of harmonics generated in Ne. Due to the Zr filter the longer wavelengths as well as the fundamental beam are suppressed. Both graphs are from [73].

There are two models explaining high-order harmonic generation and both will be briefly presented in the following subsections. Since this has not been investigated in this work, a more detailed description can be found in [24, 25, 26, 74]. The models described here refer to the single-atom response and naturally do not include realistic experimental conditions. Harmonic radiation is always the macroscopically resulting buildup of coherent microscopic processes which will be explained in the following subsections. Thus macroscopic effects such as phase matching will be dealt with later since this section should just give a short theoretical background at the atomic scale.

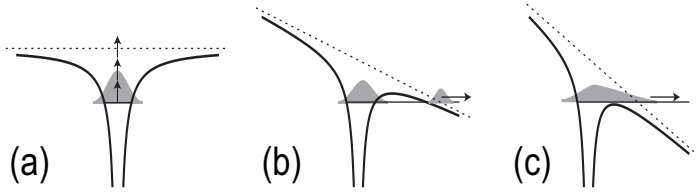

Figure 3.2: In (a) is the situation of *multiphoton ionization* if the laser frequency is large but the electric field is low compared to the ionization potential. If the E-field of the laser is stronger ($E_{laser} \sim E_{pot}$) and distorts the ionization potential, *tunnel ionization* may occur as in (b). For this, the laser frequency has to be low enough to enable the electron to follow the changes of the potential. When $E_{laser} > E_{pot}$, it can suppress the Coulomb barrier completely and *barrier-suppression ionization* dominates (c).

3.1.1 Semi-classical Model

In 1993, Corkum [75] described harmonic generation in a semi-classical model, that has not lost any of its importance to date. It assumes that the electrons do not interact with one another (single-electron approximation) and that one electron can be treated as a free particle after ionization. There are different ways for the electron to leave the atom which is illustrated in Fig. 3.2. The so-called 'Simple-Mans Model' predicts the electron's motion in an atomic potential that is influenced by a strong linearly polarized laser field. The three important steps of this model are shown in Fig. 3.3:

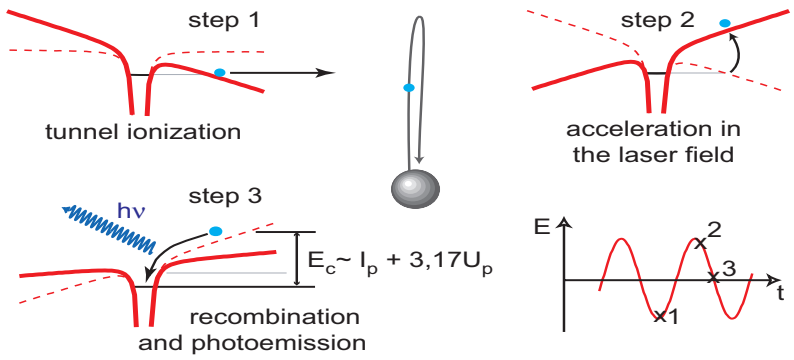

Figure 3.3: Three steps of the process of high-order harmonic generation: in step 1 the electron is tunnel-ionized at a certain phase of E, in step 2 the electron gains momentum in the laser field, and in step 3 it recombines with the atom and emits a photon. This photon carries the kinetic energy of the electron plus its ionization potential. The highest possible energy can be computed to $E_{max} = E_{pot} + 3,17U_{pond}$. At the lower right is a plot of when the three steps take place in time.

Ionization

When laser intensities are as high as $10^{14}W/cm^2$, the laser's electric field starts to distort the Coulomb potential and thus the barrier holding the electrons back becomes weaker. One possibility is that the potential is changed in a way that the electron can now tunnel through the Coulomb barrier with a high probability or the electron is field-ionized if the laser intensity is strong enough (compare Fig. 3.2). The latter is called barrier-suppression ionization and is explained in more detail in [76].

This ionization process occurs twice per optical cycle each time the electric field amplitude is large enough. Which ionization process is the dominant depends on the ionization potential E_p or I_p of the atom, the maximum electric field strength E_0 and the wavelength of the laser λ. The ponderomotive potential is a quantity defined as $U_p = E_0^2/(4m\omega)^2$ and represents the kinetic energy that a charged particle gains on average over the fast oscillations of the laser field. It is introduced not as a potential but as a potential-like scalar to simplify the problem. From these two quantities, I_p and U_p the Keldysh parameter was defined in 1965 [77]:

$$\gamma = \sqrt{\frac{I_p}{2U_p}} \tag{3.1}$$

- If $\gamma > 1$, U_p is small compared to the ionization potential and the predominant process will be multi-photon ionization of the electron.

- If $\gamma < 1$, the ponderomotive potential is comparable or larger than I_p and mainly tunnel ionization will occur.

Important to note is the fact, that there is no strict separation of the two processes and the above definitions are more a rule-of-thumb than exact prediction. Some calculations already suggested tunneling in a regime ($\gamma = 1 \dots 2$), where definitely multi-photon ionization should be the main process [78, 79].

Acceleration
After being ionized the electron is free from the binding forces of the atomic potential and begins to move along with the strong electric field of the laser. Immediately after leaving the Coulomb potential, the electron will be accelerated away from the atom but as soon as the field reverses a backward movement takes over. This way the electron accelerates towards the atom again and may recombine or 'take one more round'. The amplitude of this movement is in the order of some nanometers and can be generalized to E_0/ω^2. Since $r_{bohr} = 5.29 \cdot 10^{-11} m$ is much smaller than this amplitude, it is reasonable to consider the electron dynamics *free* after leaving the atom.
Of course, the energy with which the electron recombines is depending on the time of ionization and recombination. But the highest kinetic energy that an electron can extract from the laser field is fixed and depends on the ponderomotive potential U_p.

Recombination
For the colliding process of the electron it is assumed that the electron recombines to the ground state of the atom and thus that its kinetic energy plus the ionization potential is set free. This energy is emitted as a high-energy photon and it depends on the phase of the laser field at which the electron left the atom. From the model, it was computed that the maximum energy after recombination can only be achieved if the electron leaves the atom at a phase of 18° because only then will it have the largest possible contribution from U_p. This phase is close to the peak of the electric field and therefore the ionization probability is relatively high. The energy of the emitted photon is given by the cut-off law:

$$E_{cut-off} = \hbar\omega_c = 3.17U_p + I_p \tag{3.2}$$

and it has proved to be true for the cut-off harmonics in many experiments. From this rule and the various phases at which electrons may be ionized, continuous high-energy radiation is expected that reaches up to the cut-off energy. To understand why not a continuous spectrum but rather equally-spaced, discrete spectral peaks are generated (Fig. 3.1) one has to consider the macroscopic effects as well.

Why only odd harmonics?

As mentioned before, high-order harmonics are the macroscopic result of a buildup of microscopic processes. The fundamental laser field will - for long enough pulse durations - provide the peak field strength to ionize electrons every half-cycle and thus harmonics are

generated twice per optical cycle [80]. Now if many atoms are contributing to the generated high-energy radiation and have a constant spatial distance, the propagation direction has to be collinear with the fundamental laser field. Forming a coherent buildup, a train of harmonics will develop parallel with the laser beam and the pulse-to-pulse distance will be $T/2$ (where T equals one oscillation cycle of the driving laser field). For phase matching reasons, the spectrally-broad emitting atoms will constructively interfere to generate a temporally coherent spectrum with discrete lines. The spacing between each harmonic can be calculated from the temporal separation of its generation which is $\frac{1}{T/2} = 2f$. Thus, the spectral distance between the discrete harmonics depends on the frequency of the fundamental laser and is in our case $2 \cdot 1.55eV = 3.1eV$ for 800nm.
This process can also be explained by transition rules that allow an atom only to absorb two photons and therefore the emitted energy can only increase stepwise by twice the driving laser's photon energy.
The odd-harmonics-only rule can be changed only by breaking the symmetry of either the medium or the laser pulse. This corresponds to using for example molecules as conversion medium or mixing the fundamental with a second laser pulse [78], respectively. The latter is a technique suggested for the generation of single attosecond pulses from multi-cycle fundamental pulses [81]. The idea behind this is to introduce a temporal gating so that only from one peak of the electric field harmonics are generated. More about this and other approaches to the attosecond regime will be discussed in section 3.1.3.

3.1.2 Quantum-mechanical Model

Lewenstein at al. extended the semi-classical model from Corkum quantum-mechanically one year after its appearance in 1993 [82]. Starting with the time-dependent Schrödinger equation

$$i\frac{\partial}{\partial t}|\psi(\vec{r},t)\rangle = \left(-\frac{1}{2}\nabla^2 + V(\vec{r}) + \vec{r}\vec{E}cos(\omega t)\right)|\psi(\vec{r},t)\rangle \tag{3.3}$$

in atomic units where $V(\vec{r})$ is the atomic potential, the dipole moment was computed.

$$\vec{\mu}(t) = \langle\psi(\vec{r},t)| - \vec{r}|\psi(\vec{r},t)\rangle \tag{3.4}$$

This dipole moment characterizes the dipole that oscillates and generates the harmonics. Therefore from the Fourier transformation of the dipole acceleration one can compute the harmonic spectrum.
In [82], some assumptions were made regarding the ionization of the atomic system: First, the only atomic state that is considered is the ground state $|0\rangle$ because all other states can be neglected. In the strong-field regime ($\gamma < 1$) where harmonic generation takes place, excited bound electronic states are Stark shifted and smeared out. Thus intermediate resonances should not affect the transition from ground state to the continuum. The strong-field approximation (SFA) assumes that the laser affects only weakly the states in which the electrons are strongly bound to the atomic nucleus. For the states in which the electrons are not bound to the nucleus, the effect of the binding potential is neglected, whereas that of the laser field is fully considered.
A second assumption is that the ground states' depletion is neglected due to working below the saturation level of the medium ($U_p < U_{sat}$). In general, this is a reasonable approach because in most experiments the laser intensities are smaller than the saturation intensity of the medium. The third assumption regards the already addressed model, that the electron can be treated as a free particle after ionization. This argument holds for U_p being large compared to the remainder of the atomic potential, which is assumed to

be a short-range potential. Also, the harmonic radiation from one atom is assumed to be generated only by one returning electron (single-active electron approximation, SAEA [83]).

Under these assumptions, the time-dependent dipole moment can be obtained:

$$\vec{\mu} = i \int_0^t dt' \int d^3\vec{p} E cos(\omega t') \times \left(\vec{d}\left(\vec{p} - \vec{A}(t')\right) \times exp(-iS(\vec{p}, t, t')) \times \vec{d}^*\left(\vec{p} - \vec{A}(t')\right)\right) + c.c. \tag{3.5}$$

Here $\vec{A}(t)$ is the vector potential of the laser field, $\vec{p} = \vec{\nu} + \vec{A}(t)$ is the canonical momentum and S stands for the quasi-classical action [4] and is defined as:

$$S(\vec{p}, t, t') = \int_{t'}^{t} \left(\frac{\left(\vec{p} - \vec{A}(t'')\right)^2}{2} + I_p \right) dt'' \tag{3.6}$$

this represents the phase change of the electron while it is moving in the continuum. I_p is the atomic potential and is considered the constant ionization potential. $\vec{d}(\vec{x})$ in 3.5 is an expression for the transition probability from the bound electronic state $|0\rangle$ to a continuum state $\langle x|$ - this is ionization. The complex conjugate describes the inverse process which is recombination of the electron to its former ground state. So one can write $\vec{d}(\vec{x}) = \langle \vec{x}|\vec{r}|0\rangle$ for ionization and $\vec{d}^*(\vec{x}) = \langle 0|\vec{r}|\vec{x}\rangle$ for recombination which gives us a little more understandable perspective of equation 3.5. Concluding one can link parts of the computed $\vec{\mu}(t)$ to steps of the three-step-model:

- $\vec{d}\left(\vec{p} - \vec{A}(t')\right)$ corresponds to the ionization of the ground state at time t'.
- $exp(-iS(\vec{p}, t, t'))$ stands for the propagation of the electron in the continuum.
- $\vec{d}^*\left(\vec{p} - \vec{A}(t')\right)$ is the recombination of the electron with the atom at time t.

By Fourier-transformation of the time-dependent dipole moment, one can compute the harmonic spectra. Interestingly, the quantum-mechanical treatment results in a similar cut-off photon energy law as previously the three-step-model:

$$\hbar\omega_c = 3.17U_p + f\left(\frac{I_p}{U_p}\right) I_p \tag{3.7}$$

where $f(x)$ is a slowly varying function on the order of one. For example, $f(0) \approx 1.32$ for $U_p >> I_p$ and $f(3) \approx 1.25$ for $U_p = \frac{1}{3} I_p$ so this does not change the resulting cut-off energy significantly. The reason for this correction term are quantum-mechanical effects such as tunneling and spreading of the electron wavepacket in the continuum, that are not included in the semi-classical model. In the end, this factor gives the electron slightly more energy when returning to the atom than with the three-step-model.

As one can see from equation 3.5, different electron trajectories included in the integral accumulate different atomic phases ($\phi_{at} = S(\vec{p}, t, t')$) while travelling through the continuum. The resulting shape of the electronic wavepacket on recombination is then determined by the overlap between these separate quantum paths. Reexamining the idea of the semi-classical calculation of the kinetic energy of the electron, one can see that

each harmonic can be generated by the electrons from two different quantum paths (Fig. 3.4). In one of them, the electron spends a longer time (almost one optical cycle) in the continuum before recombining with the electron; this is called the *long trajectory*. The *short trajectory* is the path of the electron, that is ionized 'later' and therefore spends less time in the continuum. In conclusion, one single harmonic depends on the constructive or destructive interference of the wavepackets of the returning electrons.
Because the electric field is included in the dipole moment, one can control the harmonic generation process by arbitrarily shaping the laser pulse [84, 85]. The challenge is that the electric field of the laser is not only capable of interacting with the intra-atomic process but also macroscopic phase matching can be employed for selective enhancement or suppression of single harmonics [86]. This can be understood by exciting different fiber modes in the capillary where the harmonics were generated [87, 88]. Using another source of high-order harmonics, the gas jet, one can control the harmonic quantum path by macroscopically changing the focal position with respect to the gas jet [89]. Additionally, the harmonics from the two different quantum paths can be separated by spatial filtering because the contributions have a slightly different divergence and pulse duration [90].

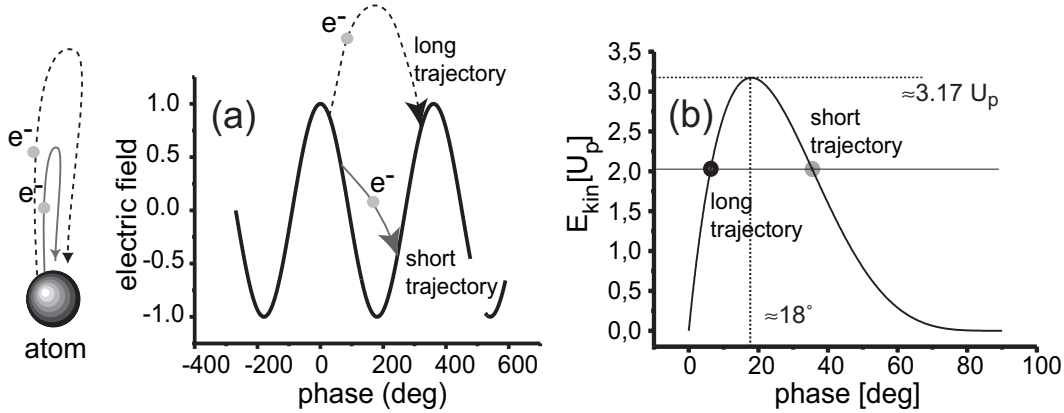

Figure 3.4: Illustration of the two different quantum paths, which stand for different periods of time before the electron-ion recombination (left). In (a), one can see the electric field of the laser in black and the two trajectories all plotted versus the phase. On the right (b), the graph shows the kinetic energy in U_p of the long and the short trajectory. For every energy (and thus for every harmonic), there are two electrons contributing to it. Only the highest possible energy in the cut-off regime consists of just one single quantum path where the electron is ionized at phase 18°.

From the three-step-model one can see, that the *long trajectory* is much more influenced by an additive phase than the *short trajectory*. After careful analysis [91, 92] the *long trajectory* exhibits a phase that is linearly proportional to the laser intensity whereas the phase of the faster recombining electron is almost constant:

$$\frac{d\phi_{atomic,long}}{dI} = a, \frac{d\phi_{atomic,short}}{dI} \approx 0 \tag{3.8}$$

Since the laser pulse intensity at the pulse peak varies quadratically with respect to time, a quadratic temporal phase will be imprinted on the harmonic radiation [93, 94]. This results in a linear chirp and delays the different harmonics with increasing order in respect to each other.

3.1.3 Attosecond Physics

As seen in the previous section, the processes involved in high-order harmonic generation are in the temporal regime of sub-femtoseconds. The shortest possible pulses for a given central wavelength are single-cycle pulses. For a Ti:Sa laser system like ours, the central wavelength is about 800nm which gives a shortest pulse duration of $\approx$ 2.7fs. In order to achieve a better time resolution, shorter wavelengths are needed and high-order harmonic generation is an excellent tool to extend the pulse duration to below one femtosecond. As already explained in section 3.1.1, the harmonics are created every half-cycle of the laser pulse, so naturally an attosecond pulse train (APT) is generated [95]. These ultrashort pulses have already been used for spectroscopy of He [96] or N_2 [97].
As shown in Fig. 3.5, by using a short enough driving pulse the harmonics above a certain energy level are automatically generated at one single moment in time.

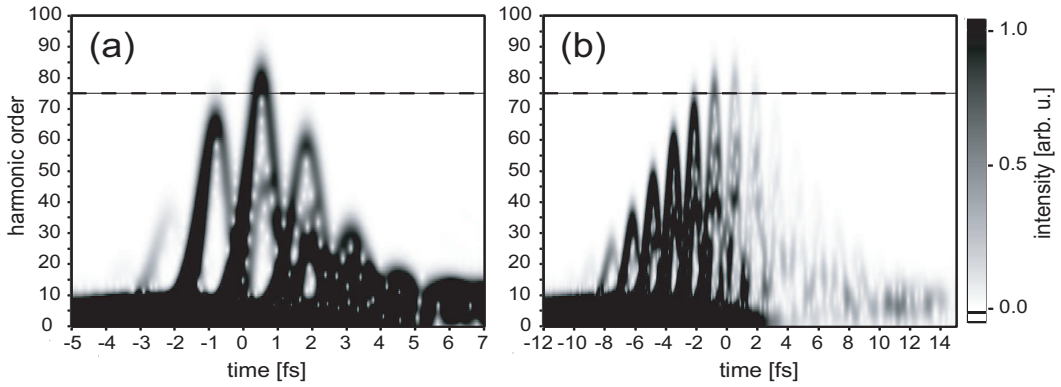

Figure 3.5: Computed time-frequency analysis of the dipole response of H in an intense $5.5 \times 10^{14} W/cm^2$ 800nm laser pulse with a duration of 4 fs (a) and 10fs (b), respectively. This simulation was performed for a two-dimensional quantum-mechanical system using the split-step-operator technique [98]. As predicted before, two contributions per harmonic (arc-like structure) are visible. Above the energy of the 75th order of the harmonics (corresponding to 116eV) are four sub-fs pulses when a 10-fs laser pulse is used (b). By employing a driving pulse with a duration of 4fs, there is only one isolated attosecond pulse left in the high-energy regime (a). This gives an idea of how single attosecond pulses may be generated.

In 2003, Mairesse et al managed to measure only the contribution of the short quantum path and thus a linear chirp for 14 consecutive harmonics [99]. This purely linear chirp can be compensated by plasma dispersion of additional ionized gas or by using the negative group dispersion delay (GDD) of a thin aluminum foil [100]. While every way of harmonic generation naturally includes a variety of wavelengths and features a temporal pulse-train structure, achieving single attosecond pulses is rather challenging. In the following, the generation, characterization, and application of attosecond pulses will be described with a few selected examples since it is a strong motivation for this work.

Generation of single attosecond pulses
The first approach in 2001 was to use a Mo/Si multilayer mirror that reflects and focuses selectively the 90-eV part of the harmonic radiation [48]. This mirror is placed on

a delay stage so that one can measure the cross-correlation between laser and XUV beam by focusing both onto a Kr target and detecting the photoelectrons. From the electron momenta distribution, XUV pulse durations of $\approx$ 500as could be reconstructed in this setup. Because of its filtering of the cut-off harmonics and using only the peak intensity of the laser pulse, this technique is referred to as *ionization gating*. In the last 7 years, this method has improved a lot in terms of stability, XUV intensity, and pulse duration so that further below in **Applications** some experiments based on such a setup are introduced.
The group of Nisoli suceeded in 2006 by applying the so-called *polarization gating* technique [47] first suggested in 1994 [101]. They used a 5-fs CEP-stabilized driver pulse that had a modulated polarization state with an ellipticity, that is only zero at one well-defined point in time. Since harmonic generation, especially the recombination process, is very sensitive to a non-linear polarization, making the polarization well-suited for HHG in only a short time window results in a single attosecond pulse [102]. This is done by shaping the fundamental laser pulse so that it is elliptically polarized except for one optical cycle. Only in this cycle, efficient harmonic generation can occur and thus a well-defined temporal resolution is given.
Apart from these successful experiments, some theoretical suggestions on how to generate single attosecond pulses have been made. By simulating the experimental conditions from [48], it was found that far-field spatial filtering played in important role [103]. According to the authors, it seems possible to generate single attosecond pulses by selecting the correct section of the spectrum and a corresponding distance from the source. In [104], Dudovich et al. propose a two-color setup where the delay between the SHG and the fundamental driver pulse is serving two purposes. First, if the SHG-beam's intensity is low enough, by evaluating the resulting even-harmonic spectrum one is able to characterize the attosecond pulses. As soon as the second harmonic's intensity is increased, the method turns into the control-mode and allows switching on and off the odd harmonics. A last up-to-now only theoretical way is the generation of high-order harmonics from surfaces [105]. The reason for high-order harmonics from solids - or more accurately from overdense plasma - is the much higher output of XUV radiation. This is partly due to the fact, that HHG from overdense plasma is of relativistic origin and the higher intensities induce stronger nonlinearities resulting thus in higher conversion efficiencies.

Characterization Methods
Not only the generation of attosecond pulses from high-order harmonic generation poses a problem but the temporal analysis of the generated pulses is another non-trivial aspect in this regime. In this work, the different techniques are described only briefly but a detailed review on attosecond detection can be found in [24, 25, 26, 106].
The first measurement is described above and was performed by Hentschel et al [48]. They used a kind of 'streaking camera' which corresponds a cross-correlation of the fundamental and the XUV beam [107]. The problem of many XUV characterization measurements is the necessary delay between the XUV beam and a second laser pulse (e.g. the fundamental beam). Small angles between the two propagation directions result in temporal smearing of the correlation signal which is proportional to the beam diameter d and the angle α. To reach a 100-as time resolution one would need an angle smaller than 0.87mrad that experimentally almost corresponds to a collinear geometry. This brings the second problem since beamsplitters and recombiners are not easily available in the XUV-regime. A work-around is a split mirror whose inner multilayer part reflects the desired attosecond pulses and the spatially filtered outer part focuses the fundamental beam [108]. This way a stable collinear delay was realized and resulted in the first successful correlation

measurements regarding high-order harmonics. To date, many more techniques have been suggested and implemented to match the FROG technique (see section 1.3.2) in the XUV-regime [109, 110]. Also an equivalent of the simple autocorrelation technique has been realized for attosecond temporal resolution [111]. Pulse durations down to sub-100as have been measured using those.
Another experiment was suggested in 2002 [112] and realized in 2003 [113] that was also based on the idea of the overlap between XUV and driver pulse. It utilizes two-photon, multicolor ionization to analyze the amplitudes and spectral components thus allowing the reconstruction of an average temporal profile. The name "reconstruction of attosecond beating by interference of two-photon transitions" (RABITT) stands for a successful technique to characterize attosecond pulse trains down to 250as. The downside is that no information about the spectral phase within one harmonic can be gained but only the relative phases between all harmonic orders.
Different versions of the SPIDER (section 1.3.2) technique for the XUV have been implemented as well. In [114], two time-delayed IR pulses with slightly different central wavelengths are generating almost identical attosecond pulses with a spectral shear. This shift in frequency produces an interferogram which can be detected directly with an X-ray spectrometer. The precision of this method is much higher than the detection of pulse duration via photoionized electrons. However, since the second pulse is following the first one with a certain temporal delay, the first one must not carry a lot of energy so that the two harmonic generation processes are not influenced by one another. This can be circumvented if the setup is changed in a way, that the interferogram is not spectrally but spatially encoded [106]. Two spatially separated high-order harmonic beam are brought to overlap in space. Thus the detected carrier modulations do not depend on the temporal delay but on the spatial separation of the pulses after propagation from the interaction region. As a further advantage, the spectrum does not need to be resolved at high resolution which relaxes the constraint of a good spectrometer. This evolution and improvement of our existing characterization method is called 'spatially-encoded arrangement for SPIDER' (SEA-SPIDER).

Applications of attosecond light pulses
One process that is of vital interest for harmonic generation is the tunneling of the electron out of the atomic potential. By an attosecond pump-probe experiment multi-electron excitation (shake-up) and relaxation (cascaded Auger decay) processes are examined [49]. The sub-fs time constant of the Auger decay could be resolved for Neon by using a 5.5-fs, CEP-stabilized Ti:Sa laser system as pump and $\approx 250as$ XUV as probe pulses. The information is gained in real-time by changing the delay between pump and probe pulses and detecting the ions with a time-of-flight ion spectrometer with high mass and spatial resolution.
An attosecond double-slit experiment has also been realized in the time-energy domain rather than the conventional position-momentum domain [115]. The role of slits is played by windows in time of attosecond duration which can be opened or closed by changing the temporal evolution of the field of a few-cycle laser pulse. In the plane of the polarization, two opposing detectors are located which detect the photoelectron spectra of argon as a function of the CEP. It is possible to accelerate the electrons ionized by the fundamental laser using the attosecond pulse. Since the orientation of the attosecond pulse depends on the electric field of the laser - sine or cosine pulse - one can switch the electrons from right to left by changing the carrier-envelope phase.
The fact, that one can compensate the intrinsic chirp of the harmonics was already de-

scribed [100] but using the correct thickness and material it is even possible to shape high-order harmonics in amplitude and phase [116]. Thus attosecond pulses can be optimized in bandwidth or pulse duration by simply using the appropriate filter.
It was suggested in 2007, that using two-color orthogonally polarized laser fields it should be possible to isolate single attosecond pulses as well as monitor molecules with some kind of orbital tomography [102]. By crossing two laser beams and monitoring the XUV radiation generated in the focus, the different harmonics are emitted over a range of angles. This links subcycle temporal resolution with several degrees spatial resolution and allows for a single-shot orbital tomography of molecules. This also results in attosecond pulses being spread spatially and thus a spatial filter would be sufficient for single attosecond pulses.

3.2 Harmonic Generation in the Laboratory

Generally, every nonlinear interaction where an intense laser pulse is focused into matter is capable of producing high-order harmonic generation. It is the strong absorption of air in this energy regime (~ 30 to $\sim 5000eV$ in our setup) that makes it necessary to work in vacuum with the generated radiation. The name "vacuum ultraviolet" (VUV) accounts for the only stable existence of these photons in vacuum chambers.
The second question that arises is the question of the target: solids can be used in vacuum but for HHG they require a relativistic energy regime which needs rather high laser intensity. Fluids are not well-suited for vacuum setups but nevertheless some experiments were conducted [117] and provided interesting results. Both of these dense media feature a rather high conversion efficiency along with problematic requirements for our laboratory setup. Gaseous media can easily be inserted in vacuum chambers and by differential pumping the background pressure can be kept at a constant moderate level. One more advantage of gas is the possibility to switch from one gas to another without complicated change of the target chamber. The last reason for a gas target is the adjustable pressure which gives one more parameter for optimization of the harmonic output.

3.2.1 Gas-filled hollow-core Fiber

One technique for high-order harmonic generation is focusing the laser into a gas-filled hollow-core fiber at a defined pressure. The laser propagates collinearly with the XUV radiation and the buildup of harmonics takes place over the complete length of the capillary ($\sim 5cm$) in an ideal case. A schematic setup is illustrated in Fig. 3.6.

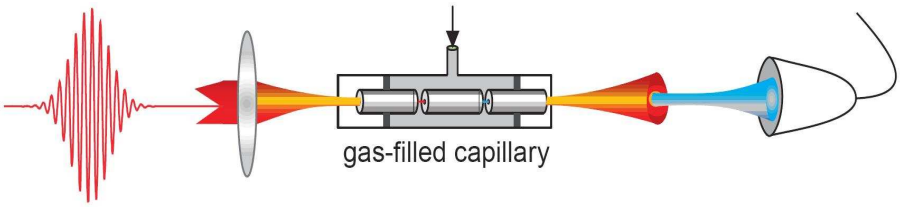

Figure 3.6: HHG scheme in a fiber setup. The laser pulse is focused into a capillary and propagates along with the harmonics. The three-parted glass provides a high-enough pressure for harmonics in the middle section while the first and last hollow-core fiber serve as differential pumping stages. After exiting the fiber and propagating some distance in vacuum, the fundamental beam is separated from the harmonics by an Al filter.

Clearly, when the propagation in the fiber plays such an important role, 'phase-matching' is crucial in this kind of implementation. By 'phase-matching' we mean a constructive overlap of the phases of the fundamental and generated laser pulses so that the conversion efficiency is as high as possible. For constructive harmonic generation, the phase velocity of the driving laser pulse must match that of the harmonic. In wave-vector notation this means $\Delta k = qk_{laser} - k_{xuv} = 0$, where q stands for the harmonic order. This already illustrates, that efficient generation of more than a few harmonics ($\sim 5 - 10$) is not possible. Because harmonic generation as a macroscopic phenomenon depends on constructive microscopic interference, phase matching is a very important aspect. Therefore its background will be given here in a little more detail.
Due to the propagation within a capillary filled with gas, there are different contributions

to the cumulative dispersion. Basically, it depends on three effects:

- The **neutral dispersion** is influenced by the gas pressure and the type of gas used for HHG. It can be characterized by:

$$k_{disp}(\lambda) = \frac{2\pi N_a \delta(\lambda)}{\lambda} \tag{3.9}$$

  where N_a is the atom density and $\delta(\lambda)$ depends on the neutral gas dispersion. Assuming that the index of refraction is higher in the visible than in the XUV-regime where the harmonics are generated, one can conclude that $\Delta k_{disp} > 0$. Thus we have a positive contribution to the overall dispersion.

- **Plasma dispersion** is relying on the generated free electrons that will oscillate in the electric field of the laser with respect to the atomic center. The refractive index of such a free-electron system is given by

$$n_{plasma}(\omega) = \sqrt{1 - \left(\frac{\omega_p}{\omega}\right)^2} = \sqrt{1 - \left(\frac{N_e}{N_c(\omega)}\right)} \tag{3.10}$$

  with ω_p being the plasma frequency which is the resonance frequency of the laser-driven plasma. N_e is the free-electron density and $N_c(\omega) = \frac{\epsilon_0 m_e \omega^2}{e^2}$ is the critical density at which the plasma becomes opaque for radiation with the frequency ω. Correspondingly, the resonance frequency of the plasma is given by:

$$\omega_p^2 = \frac{N_e e^2}{\epsilon_0 m_e} \tag{3.11}$$

  Here e is the unit charge, ϵ_0 is the vacuum dielectric constant, and m_e is the electron mass. If we are dealing with a weakly-ionized gas, meaning the relative amount of free electrons is comparably small, equation 3.10 can be linearly approximated by:

$$n_{plasma}(\omega) \approx 1 - \frac{1}{2}\left(\frac{\omega_p}{\omega}\right)^2 \Rightarrow \Delta n_{plasma} = -\frac{1}{2}\left(\frac{\omega_p}{\omega}\right)^2 \tag{3.12}$$

  From this change of the refractive index, the contribution to the wave vector Δk_{plasma} can be computed by putting equation 3.11 into equation 3.12 as a function of λ:

$$\Delta k_{plasma}(\lambda) = \frac{2\pi \Delta n(\lambda)}{\lambda} = -\frac{e^2 N_e \lambda}{4\pi \epsilon_0 m_e c^2} \tag{3.13}$$

  The classical electron radius $r_e = \frac{1}{4\pi\epsilon_0}\frac{e^2}{m_e c^2}$ helps to simplify equation 3.13 to

$$\Delta k_{plasma} = -N_e r_e \lambda \Rightarrow \Delta k_{plasma} < 0. \tag{3.14}$$

  One can see that the plasma dispersion is always a negative contribution to the wave vector. As with the filament (section 1.2.2), the laser pulse will "see" the creation of the plasma and thus a fast negative change of the index of refraction. The resulting SPM causes only a blueshift, since the recombination time of the plasma is much longer than the pulse duration and the pulse does not "see" it happen.

- Unlike the previous Δk_{plasma} and Δk_{disp}, the contribution of **waveguide dispersion** is only existing for the propagation in a capillary. Because in this work only harmonics from a gas-filled tube are used, the waveguide contribution to the wavevector is introduced here just for completeness. It can be described by

$$k_{geom}(\lambda) = -\frac{u_{nm}^2 \lambda}{4\pi a^2} < 0 \tag{3.15}$$

  where u_{nm} is the m-th root of the Bessel function $J_{n-1}(z)$ and a is the inner radius of the hollow-core fiber. The derivation as well as more explanation of this formula is given in [118]. Again, our main interest is the negative contribution to the overall Δk.

Additionally, the propagation term for vacuum, $k_{vac} = 2\pi/\lambda$, has to be added to the wavevector terms so that the resulting complete dispersion for propagation in a gas-filled hollow-core fiber can be written as:

$$k(\lambda) \approx \frac{2\pi}{\lambda} + \frac{2\pi N_a \delta(\lambda)}{\lambda} - N_e r_e \lambda - \frac{u_{nm}^2 \lambda}{4\pi a^2} \tag{3.16}$$

For the gas-filled tube, the last term from the waveguide propagation can be neglected. The main adjustable parameters for our setup is the gas pressure, the gas type and the wavelength of the fundamental laser. An additional very important parameter is the beam quality (e.g. divergence, wavefront) although this is adjusted once to be optimal and then ideally remains this way. Due to the long interaction range, in gas-filled hollow-core fibers mostly fairly low gas pressures $p_{fiber} \approx 50 - 150$mbar are used. Pulse shaping, especially temporal, can have a huge impact for harmonics generated in fibers because of the waveguide dispersion depending strongly on the temporal shape of the pulse [84, 86, 119, 120, 85]. Shaping of the waveguide is another approach to influence the phase-matching conditions as was successfully demonstrated [88]. With this technique, artificial regions of higher and lower gas-densities are generated which leads to quasi phase-matching (QPM) due to macroscopic constraints.

3.2.2 Gas-filled Tube

The free-focusing geometry can be realized in different ways. One way is to employ a pulsed gas-jet that is triggered by the laser and provides just enough gas for harmonic generation but not too much for strong reabsorption. For this mostly a piezo-driven pulsed pump is employed
We realized an easier setup by simply filling a nickel tube with gas at a constant pressure and let the laser drill its own hole through the metal. At spotsizes with diameters of less than $50\mu m$, the gas flow is adequately low and the interaction region has a high-enough atom density. The exact gas flow depends significantly on the size of the hole in the nickel tube which itself depends on the used focusing geometry and the beam profile. To control the gas pressure, we used a closed-loop pressure monitoring hardware that regulates the gas flow. Schematically our setup is presented in Fig. 3.7.
Employing the gas-jet setup, temporal pulse shaping does not have such a strong influence probably because the interaction length is significantly shorter than in the fiber setup. However, as mentioned earlier, the contributions of the two quantum paths can be controlled by placing the focal spot slightly before or after the gas tube. This and the increased sensitivity towards the wavefront of the pulse make it well suited for the spatial

shaping setup that was presented in section 2.3.2.

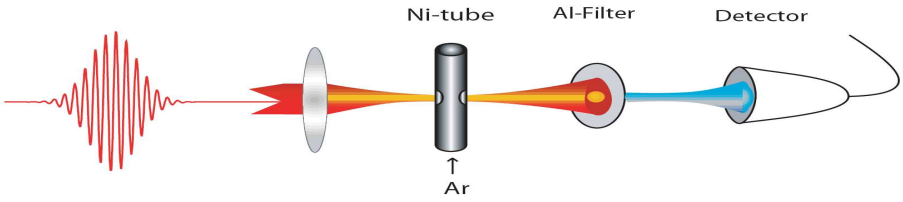

Figure 3.7: The IR laser pulse coming from the left is focused by a lens or a mirror right into the gas-filled nickel tube. The thin-walled metal is ablated very fast so that two holes on each side of the tube are drilled. Subsequently, the fundamental driver pulse is again filtered by Al or Zr filters and the generated XUV-radiation propagates to the detector. The tube can be filled with various gases and most commonly Ar, Ne or He are used.

Also, with the gas-jet higher-order harmonics can be achieved than with the capillary setup because the limitation on the peak intensity is somewhat less restrictive.

3.2.3 Setup of the "Beamline"

For our harmonic generation setup we decided to build a modular vacuum chamber with four sections that can be replaced or moved individually. A drawing of our experiment is given in Fig. 3.8.

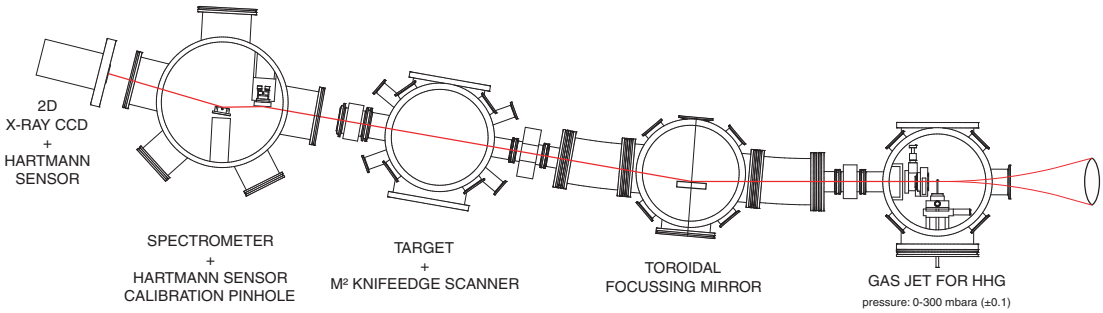

Figure 3.8: Top view onto our modular setup build of four separate chambers. The laser pulse is coming from the right, generates harmonics in the gas-filled tube which then propagate to the toroidal mirror in chamber two. The XUV-radiation is subsequently focused in our experimental chamber and afterwards recollimated by a second toroidal mirror. By passing a reflective grating and placing a 2-D X-ray CCD in the Fourier plane, the spectral and 1-D spatial properties of the generated harmonics can be analyzed.

The first chamber is build for harmonic generation in a nickel tube whose gas pressure can be controlled to within 0.1 mbar from 0 to 300 mbars. To get rid of the high gas load, a rotary vane pump and a roots pump are sequentially attached to the chamber and achieve pressures of 4×10^{-3}mbar with no gas load and during operation still less than 10^{-2}mbar. If the gas pressure is much higher than that, absorption "eats up" most of the generated harmonics. After the nickel tube a variable, electronically controlled pinhole is located to remove the outer parts of the more divergent IR-beam. The harmonics are propagating

almost collinearly with the IR-beam but due to their much shorter wavelength their divergence is only a fraction of the driver beam's.
In the next chamber, approximately 550 mm behind the nickel tube, the harmonic beam is supposed to have a diameter of about 1mm. In the bead linking the first and second chamber is a pinhole (diameter: 2 mm) for diffractive evacuation reasons. Thus it is possible to have a fairly low pressure ($10^{-5} - 10^{-7}$mbar) in all chambers but the first. The second and third chamber are evacuated by Pfeiffer $1000l/min$ turbo pumps allowing for off-duty pressures down to 10^{-8}mbar. The divergent harmonic beam is focused using a toroidal mirror (see Fig. 3.9) under grazing incidence. This is a necessary feature because focusing broadband XUV radiation is not possible with any transmissive optical elements. Therefore a focusing mirror must be employed and for a high reflectivity ($> 60\%$) is it mounted in a grazing incidence geometry under an angle of $\approx 5°$. Because such a geometry is bound to create astigmatism, a specifically designed toroidal mirror (see Fig. 3.9) is placed onto a 3-D, piezo-driven mount that can be addressed electronically.

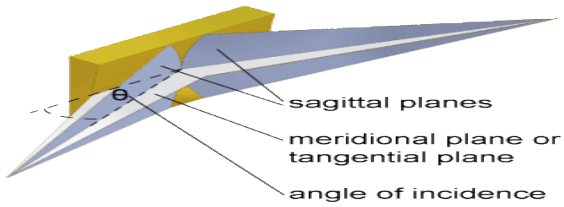

Figure 3.9: A toroidal mirror (gold coated) can be envisioned as a part of the surface of a doughnut. It is a mirror with two different radii for the sagittal and meridional plane which enables the mirror for a correct angle of incidence θ to focus a beam almost without astimatism.

The third chamber is the place for the experiments e.g. a gas target or a M-square apparatus. It has many connectors so that subsequently a time-of-flight spectrometer or other devices can be attached.
The last 'detector' chamber is for characterizing the spatial and spectral properties of the harmonics. As shown in Fig. 3.10 from [121], the XUV radiation is hitting the second toroidal mirror with the identical specifications as the one in the focusing chamber.
Directly after the mirror, the harmonics hit the reflective grating (Au, 300 lines/mm, blazed for 300nm at 3°) and are focused onto the X-ray CCD (Andor DO420BN) camera. The 1024x255 pixels allow for spectral as well as spatial detection with a resolution of $26x26\mu m^2$ (pixel size). The spectrum incident on the camera can be adjusted by tilting the grating via a goniometer. Thus in the current configuration without an entrance slit the resolution $\lambda/\Delta\lambda$ at the 51th harmonic is about 300.

Between the first and the second chamber as well as between second and third chamber, VAT vacuum valves are included that have a circular hole in the middle where our filters can be mounted. It is important to put the first filter as far away as possible from the harmonic generation point, since too high laser intensity will destroy the 200nm-thick metal foils. Thus a position as close to the toroidal mirror as possible is favorable. Of course during the pumping process the filters have to be protected from any direct airflow and therefore the vacuum valves are serving two purposes at a time: they allow moving the filters in and out of the beampath and completely shut the beamline for the fundamental

laser radiation once they are in operating position.

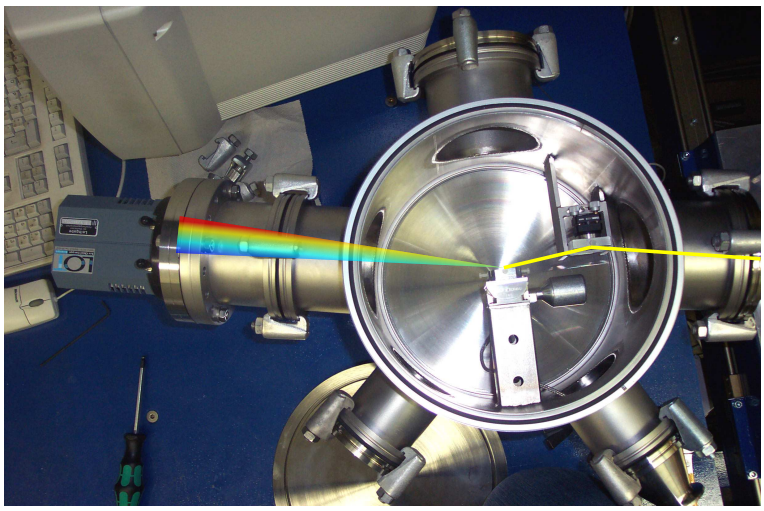

Figure 3.10: Photographic top view of the spectrometer chamber with an illustrated ray-tracing. The divergent harmonics hit the second toroidal mirror (identical in construction to the first one) which images the spectrally split XUV beams onto the X-ray CCD camera.

3.3 Filtering of High-order Harmonics

Since we need to separate the fundamental 800nm radiation from the generated harmonics, a filter that has a high transmissivity for sub-80nm (10th harmonic) radiation is needed. Basically, in this work we used Aluminum and Zirconium foils with a thickness of 200nm and 300nm, respectively. In Fig. 3.11, one can see that both filters do absorb strongly in the low-energy regime at longer than 90nm. Furthermore, the Al filter features a very large spectral window with comparably high transmission ($> 50\%$) from 20nm to 70nm which is very convenient for broadband experiments such as spectroscopy. The disadvantage about the aluminum foil is the strong absorption below 20nm (41th harmonic) that is within our generated harmonic spectrum.

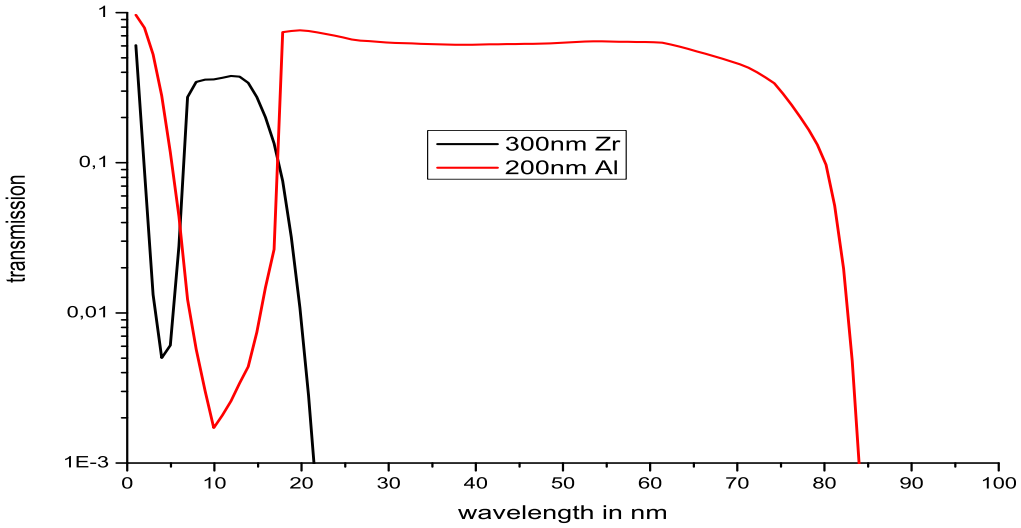

Figure 3.11: Plotted transmission of a 300nm Zr foil and a 200nm Al foil versus wavelength, respectively. Data from [122].

The Zr filter has a lot lower transmission and a smaller bandwidth of transmission but it allows higher-order harmonics ($> 41th$) to be used for experiments. The region below 5 nm is not of great importance for this work, because due to our pulse energy of at most $700\mu J$ (at a pulse duration of 25-30fs) and a 30-cm focusing lens our cut-off energy is at about 200eV (corresponding to the 131th harmonic or 6nm). The exact cut-off energy is of course depending on the used gases since the ionization potential contributes directly to it (e.g. $I_{p,Ar} = 15.8eV$ and $I_{p,Ne} = 21.6eV$).
The metal foils used to separated the fundamental from the XUV beam are not the only 'spectral shaping' elements in our setup. Since the harmonics are generated in a gas jet by interaction of the 800nm laser with ionized Ar atoms, the absorption from this needs to be taken into account as well. We assume a 2mm long interaction region with a constant pressure to estimate a realistic absorption from the gas. In reality, the pressure is far from constant but more or less rises up to the set value but decreases over about 10mm before and after the gas-filled tube. Therefore the interaction region is also hard to measure. But even though the exact conditions are not known, looking at the measured absorption [122] of for example Argon gas helps to explain the experimentally measured spectra. In Fig.

3.12 the throughput of harmonic radiation from 5 to 40 nm is plotted. If one considers that the Ar gas is effectively suppressing harmonics above 28nm and the Al foil the ones below 18nm, a fairly small window of harmonics (29th to the 43th order) appears possible.

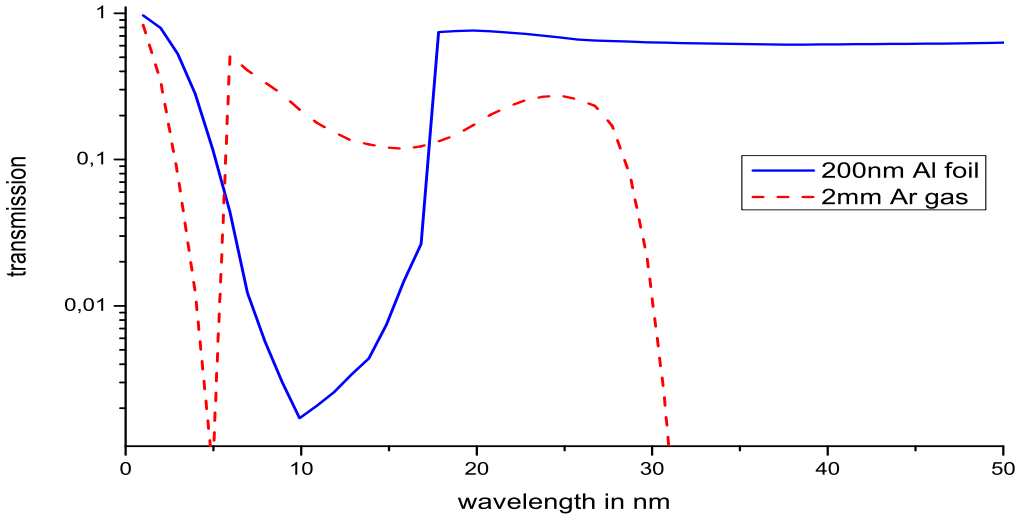

Figure 3.12: Plotted transmission of a 200nm Al foil and 2mm of 300mbar Ar gas versus wavelength. Data from [122].

The influence of different gas pressures is also interesting, but from Fig. 3.13 one can see that an increased pressure only results in higher absorption as expected. Thus the exact length of the way the harmonics travel through the gas does not matter; it is more the highest pressure that has an impact on the efficiency of the harmonic generation process.

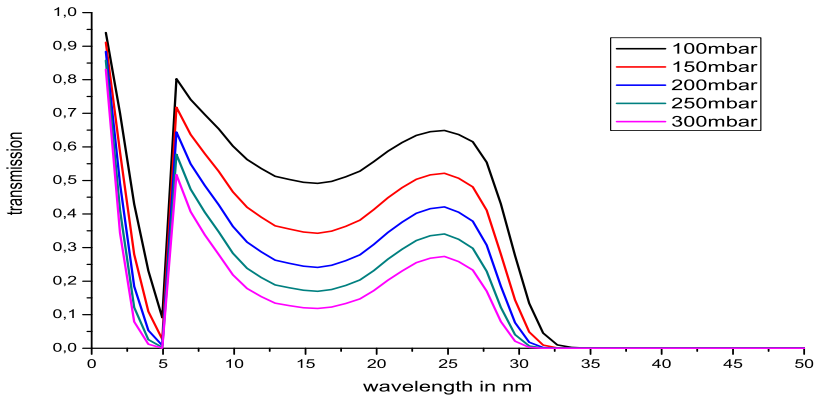

Figure 3.13: Plotted transmission of 2mm of Ar gas at various pressures versus wavelength. Data from [122].

Another important issue is the length of the interaction medium. One can see from 3.16 that the propagation through the medium is a crucial aspect of phase-matching. Therefore in our experiments, we often squeezed the gas-filled tube a little bit to decrease the high-

gas-pressure interaction region. An exact simulation of this is not conducted in this work, but it is worth noting that the dependence on the interaction length is not only a question of re-absorption (as shown in Fig. 3.14) but even more one of phase-matching.

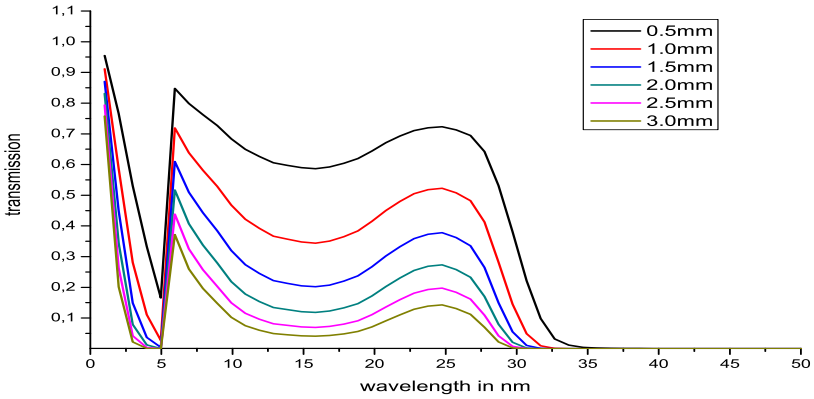

Figure 3.14: Plotted transmission of 300mbar Ar gas in dependence on the interaction length. Data from [122].

An interaction length of less than 1.0mm is not realistic in our setup because then too high gas pressures would be needed for HHG. This would result in a very high background pressure, because the overall gas that needs to be evacuated is just a function of the hole size (which can be assumed to be constant) and the gas pressure in the tube. So if the sample pressures increases over a certain level, our pump system is no longer capable of maintaining a rational background pressure in the first chamber. Thus only interaction lengths between approximately 1.0mm and 3.0mm are feasible where the difference of absorption is about a factor ten.

Chapter 4

Characterization and Optimization of HHG

At the beginning of this chapter is seems reasonable to sum up some existing results for control of high-order harmonics to date. It was already demonstrated in 2000 [84] that temporally shaping the laser pulse can influence the harmonic spectra if they are generated in a hollow-core fiber (see Fig. 3.6). In subsequent experiments in Würzburg [87, 86, 123], a further control of the efficiently generated XUV radiation could be shown. The setup is schematically illustrated in Fig. 4.1:

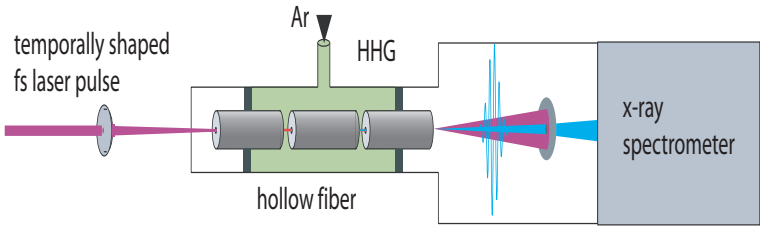

Figure 4.1: Temporal shaping setup for harmonic generation. The arbitrarily shaped laser pulses can excite different fiber modes which then generate specific harmonics more efficiently than others. The produced XUV radiation is analyzed spectrally to gain a feedback signal for the evolutionary algorithm.

In Fig. 4.2, the results of these optimizations are presented. They were performed using a closed loop algorithm and a deformable mirror with 19 independent degrees of freedom at the Fourier plane of a pulse shaper. The algorithm works as explained in Fig. 1.13 where the outcome of the experiment is supposed to depend not only on the temporal shape of the input pulse but also allows limited control of the output.
For the first experiment (shown on the left in Fig. 4.2), the fitness of a single laser pulse is defined by the intensity in the spectral region I divided by the intensity in II (in a) or vice versa (in b). The evolutionary algorithm adaptively changes the temporal phase of the laser pulse to maximize the fitness. Thus without analytical knowledge it is possible to achieve a specifically designed spectrum.
On the right side of Fig. 4.2 this ability to control the spectrum is even more pronounced. The first spectrum d) shows again the reference spectrum and in e) and f) the goal was to suppress one and two harmonics, respectively. The experiment works sufficiently although one must admit that the overall intensity is decreased along with the optimization. This

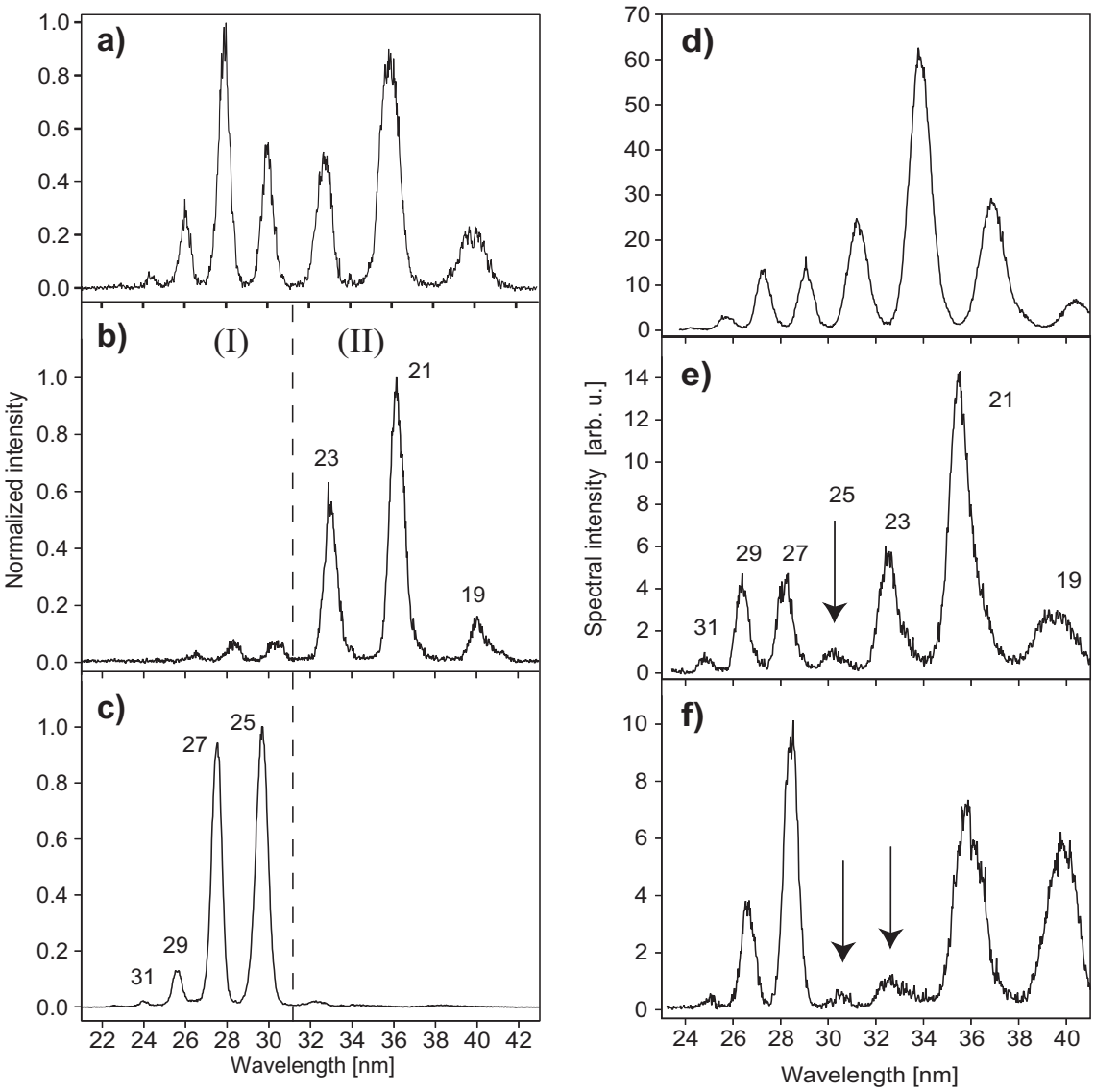

Figure 4.2: On the left (a-c) is shown selective control of HHG by defining the fitness of a driving laser pulse as the intensity at the desired part (marked as I) of the spectrum divided by the intensity at the unwanted part (marked as II). A typical harmonic spectrum is given in a) and the spectrum in b) was created by defining the fitness as II/I. c) shows the opposite definition of the fitness. On the right the selective suppression of one or two harmonics is presented. Again, a typical reference spectrum is given in d), while e) and f) show the spectra after the optimization process.

can be explained by the necessary excitation of less efficient fiber modes for the desired spectra. This is also underlined by a frequency shift of the two optimized measurements due to a somewhat different blueshift compared to the reference spectrum. Since the blueshift is indirectly proportional to the laser intensity, less intense fiber modes explain this behavior well.

4.1 Spatial Optimization

After the optimization of the beam profile after the filament (see 2.3.2) the next important step was to measure the impact of this on the harmonic generation process. To conduct these experiments we simply combined the filamentation setup for pulse compression (Fig. 2.18) with the HHG vacuum chamber (see Fig. 3.8). A no-to-scale setup is presented in Fig. 4.3.

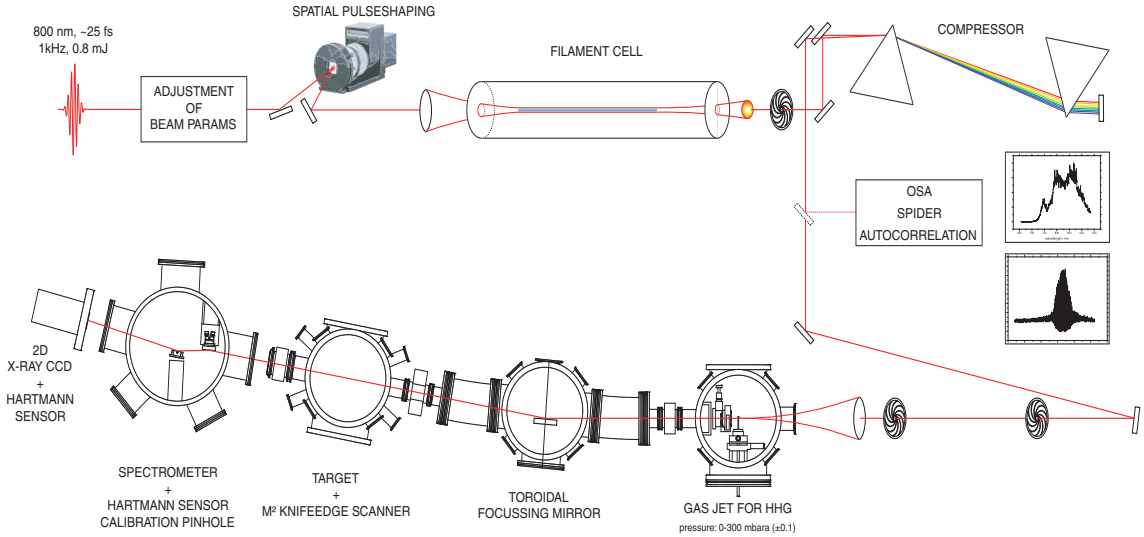

Figure 4.3: A combination of the formerly described spatial shaping and temporal compression scheme and the harmonic generation vacuum system is shown here. The laser pulse is spatially shaped by the SLM, spectrally broadened in a filament and afterwards compressed temporally. Some characterization tools are optional to measure pulse duration and/or spectrum. The 'prepared' pulse is then focused into the gas-filled tube in the first chamber, focused by the toroidal mirror onto a target and then analyzed in the spectrometer section. A Hartmann sensor is the upgrade described in section 4.2. One possible target is a knife-edge scanner to quantify the beam profile and it will be dealt with in the next section as well.

As demonstrated in Fig.4.4, an overall increase of harmonic generation can be seen. The reason for the abnormally broad harmonic peaks is a misalignment in the setup. The two toroidal mirrors are not hit on the same height and thus the beam is incident non-orthogonally to the lines of the grating but under a certain angle. This and the fact, that the CCD is not adjusted to compensate these twisted spectra somewhat leads to the very broad spectral peak of each harmonic.
Also one can see a certain blueshift from the optimized spectrum with respect to the reference one. This can be attributed to a higher intensity in the focus and therefore more free electrons in the plasma. The larger background radiation of the fittest (red) compared to the black line is probably due to scattered XUV radiation from the zeroth order. What appears interesting is the fact, that seemingly an increased intensity in the focus causes more harmonic generation to be effectively generated without changing the cut-off energy. This paradoxon can be explained by the previously discussed use of filters and the reabsorption from the gas (in this case Ar). The harmonics measured here are in good agreement with the ones theoretically expected from the energy window from the two constraining materials.

So we could confirm experimentally that spatial phase shaping of the filament can contribute to an increase of XUV radiation. A characterization of the harmonics' beam profile would give further insight into the dependence of HHG on wavefront shaping.

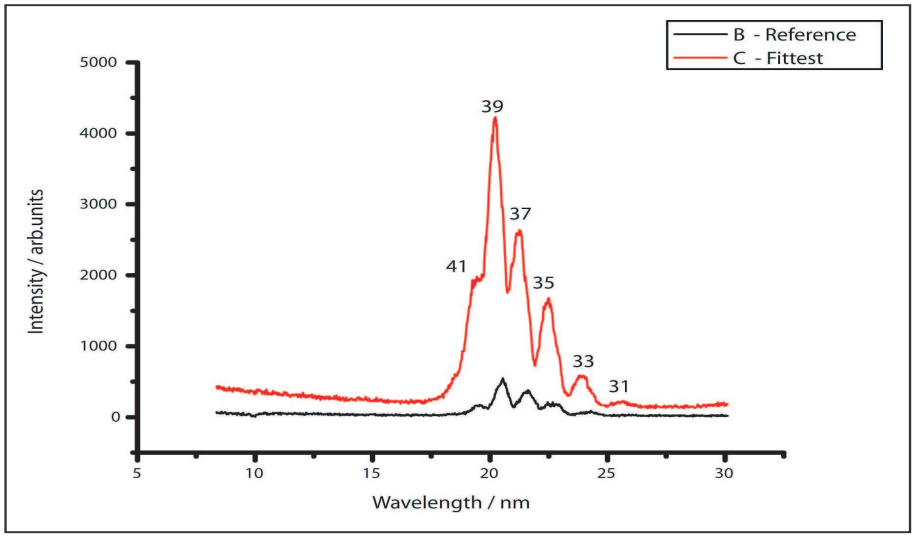

Figure 4.4: Harmonic spectrum before and after spatial optimization of the wavefront before the filament. The intensity is plotted versus wavelength and the numbers above the peaks indicate each harmonic. The overall increase is about one order of magnitude from the reference to the optimized spectrum.

What remains to be analyzed is the spectrum of the optimized harmonics in terms of a shift of the cut-off to shorter wavelengths. If the only improvement achieved by the spatial shaping is a higher intensity, this should result in a changed cut-off energy according to 3.2. Unfortunately, at the time of this experiment the available and usable filters were made of Al and the only Zr filter was damaged.

4.2 Wavefront Measurements

As we have shown before, the beam profile is an important criterion for pulse compression and thus for HHG. In addition to the M^2-measurement described in section 1.2.5, a wavefront measurement that actually allows spatially resolved wavevector analysis seems interesting. For the visible, such a wavefront analyzer can be realized like a *Shack-Hartmann*-sensor [124]. This is typically a microlens-array with a CCD chip at the focal distance of the lenses. A plane wavefront will create evenly spaced spots on the camera while for a somewhat distorted wavefront the spot array will not be perfectly symmetric anymore. The center of each focus will move depending on the k-vector of the incident wavefront. From this deviation from the plane wave, which is needed for calibration, one can compute the wavefront of the 'real' incident beam.
For XUV radiation, naturally, no microlenses are available and so a very simple trick is employed: One uses the shadows cast by a hole-array placed in front of the X-ray CCD camera and evaluates their centers. If the spacing between the holes and the diameter of the holes are small enough one can get an array of spots that do not overlap. Diffraction is not a problem here because of the wavelength that is several orders of magnitude smaller than the diameter of the holes. In our case, we are using $40\mu m$ holes and expect harmonics with less than $50nm$ wavelength. An image of the commercially available hole-array is shown in Fig. 4.5.

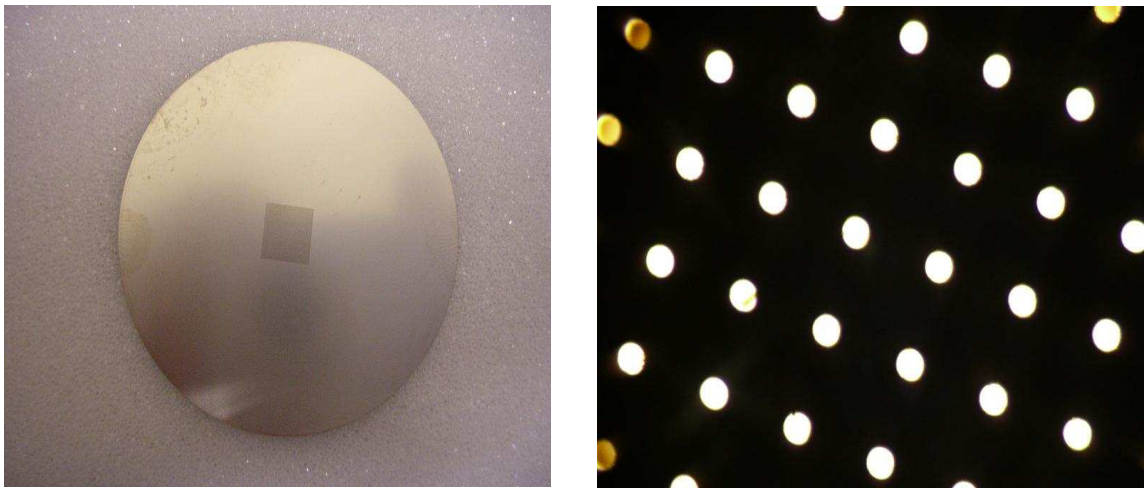

Figure 4.5: Hole array from the company Lumera, manufactured to our specifications. On the left one can see the size relative to the fingerprints at the left rim of the molybdenum plate. The right image shows an enlarged section of the array where the very symmetric spacing and shape of the holes is illustrated.

Theoretically, a much finer grid of the holes would result in a more detailed picture of the wavefront. Apart from the diffraction that might occur, the shadow of one single spot needs to illuminate more than one or two pixels in order to allow computing of the center. Since our CCD-pixels are $26\mu m \times 26\mu m$, a $50\mu m$ spot diameter is about the lower limit. Additionally, the detected intensity is fairly low when too small holes are used.
For the experiment, first of all a plane wave has to be realized for the calibration of the wavefront analysis. This is done by inserting a $1\mu m$ pinhole in the XUV beam and choosing a large enough distance to the hole array which is placed directly before the X-ray CCD

chip. Alternatively, the sun can be regarded as a source of plane waves as well and this can also be used for the calibration. The reference spot-pattern now can reveal whether the pinhole is parallel to the detector and the harmonics are incident perpendicular to the hole array. Calibration here means setting these spots as reference points from which the deviation Δx and Δy is measured after removing the pinhole. From the change of the center of each spot one can compute the k-vector at this small fraction of the beam profile (see Fig. 4.6).

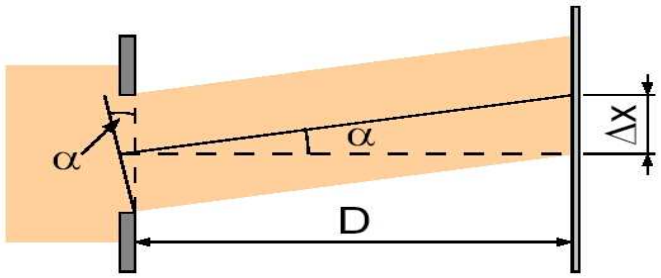

Figure 4.6: Side view of the one-dimensional change of the center of one illuminated spot. The deviation from the former center Δx is linked to the tilt of the wavefront indicated by the angle α. The distance D is only important for the calibration measurements when only a tiny part of the beam is incident on the hole array.

Using a software that is capable of interpreting the spot patterns after a given wavefront distortion (e.g. spherical, astigmatic, and comatic abberation) should help at the automated analysis. Alternatively, the program can be fed with simulated wavefronts to illustrate what to expect for evaluation. Two results of simulated wavefront are given below in Fig. 4.7.

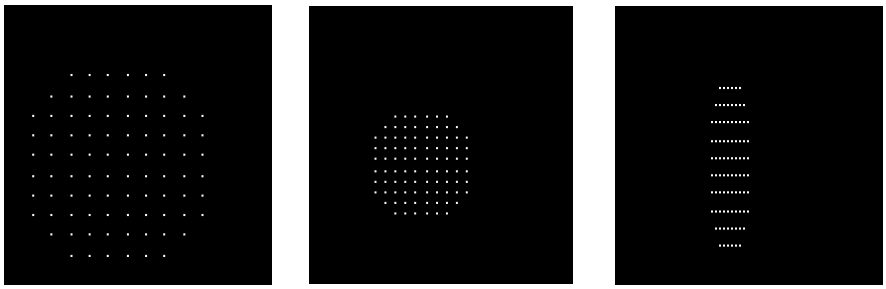

Figure 4.7: On the left image is a reference spot pattern with equally spaced spots in x- and y-direction. The middle image shows a strongly convergent beam with much smaller distances between the single spots. On the right is a simulated spot pattern for astigmatism where the spacings are different in vertical and horizontal direction.

But the wavefront can not only be constructed quantitatively by summing over the tilt of the different small part of the beam profile. Another method is the description of the generated pattern by Zernike polynomials [125]. These polynomials represent a 2-D basis system that characterizes the wavefront. Numerically, a wavefront can generally be written as the vertical offset z in dependence of the horizontal coordinates x and y :

$$z = W(x, y) \tag{4.1}$$

and knowing the $z(x, y)$ or the gradients in x- ($\frac{\partial W}{\partial x}$) and y-direction ($\frac{\partial W}{\partial y}$) the phase front is positively defined. The wavefront can be expanded as follows:

$$W(x, y) = \sum_{i=0}^{\infty} c_i f_i(x, y) \tag{4.2}$$

While as basis functions Fourier- or Taylor-expansions can be employed, the use of Zernike polynomials $Z_i^{(n)}$ implies a significant advantage: lower order Zernike polynomials represent directly the basic aberrations. Therefore one can rewrite 4.2 to

$$W(x, y) = \sum_{i=0}^{\infty} c_i Z_i^{(n)}(x, y). \tag{4.3}$$

The $Z_i^{(n)}$ are derived from Legendre polynomials $P_n(x)$ and defined on the unit circle; they make up a complete orthogonal normal basis system. The Zernike polynomials are defined in the polar coordinate system as follows:

$$Z_n^m = R_n^m(r)cos(m\theta) \text{ for } m > 0 \tag{4.4}$$
$$Z_n^m = R_n^{-m}(r)sin(-m\theta) \text{ for } m < 0 \tag{4.5}$$
$$Z_n^m = R_n^m(r) \text{ for } m = 0 \tag{4.6}$$

with

$$R_n^m = \sum_{s=0}^{(n-m)/2} \frac{(-1)^s (n-s)!}{s!((n+m)/2-s)!\ ((n-m)/2-s)!}\ r^{n-2s} \tag{4.7}$$

Although looking quite elongated, the first few Zernike polynomials that are relevant for the later analysis will be computed here. Along with the specific order the physical meaning in terms of abberation is given.

$Z_0^{(0)} = 1$	movement in z-direction
$Z_1^{(1)} = x$	tilt in x-direction
$Z_2^{(1)} = y$	tilt in y-direction
$Z_3^{(2)} = 2xy$	astigmatism in 45°
$Z_4^{(2)} = 2x^2 + 2y^2 - 1$	defocus
$Z_5^{(2)} = -x^2 + y^2$	astigmatism 0/90°
$Z_6^{(3)} = -x^3 + 3xy^2$	trefoil in x-direction
$Z_7^{(3)} = 3x^3 + 3xy^2 - 2x$	comatic-abberation in x-direction
$Z_8^{(3)} = 3y^3 + 3x^2y - 2y$	comatic-abberation in y-direction
$Z_9^{(3)} = y^3 - 3x^2y$	trefoil in y-direction

$Z_{12}^{(4)} = 6x^4 + 12x^2y^2 + 6y^4 - 6x^2 - 6y^2 + 1$	spherical aberration of the 3rd order
$Z_{24}^{(6)} = 20x^6 + 60x^4y^2 + 60x^2y^4 + 20y^6$	
$30x^4 60x^2y^2 30y^4 + 12x^2 + 12y^2 1$	spherical aberration of the 4rd order

Thus one can link the coefficients directly to a certain wavefront distortion which is demonstrated above for up to the third order and two more terms. In this listing, the upper index corresponds to the radial order m while the lower index is a commonly used for enumeration of the polynomial terms. One has to mention, that there is no convention on a consistent ongoing denomination so the one used here is only one interpretation.

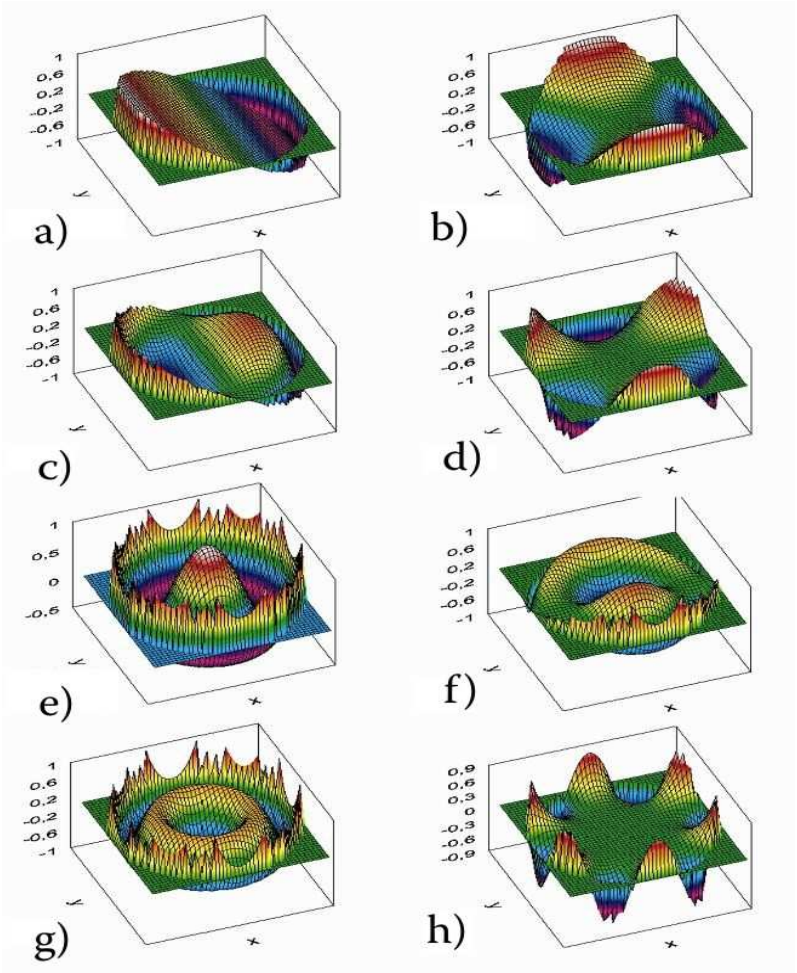

Figure 4.8: The simulated wavefronts show a tilt (a), an astigmatism (b), a comatic-aberration (c), a trefoil (d), spheric aberration (e), and higher order terms (f,g, and h). They have been computed with the evaluation software used to interpret the spot pattern on the detector.

Higher order terms than the sixth order, which are evaluated by our software, can be neglected due to the small beam diameters we are using. In astronomical context at very large beam diameters, higher order terms are necessary because they can carry important information about the distortion. Some of the numerical terms are illustrated in Fig. 4.8.

4.2.1 Computational Evaluation

To evaluate the measured spot pattern we developed a LabView program which constructs the aberrations. The first steps are universal and have to be performed for the step-by-step reconstruction of the wavefront and for the analytical Zernike-based computation of the aberrations.

Finding the correct spots
Since our hole array has squared unit cells, the pixels of the CCD chip are separated into $N \times N$ squares with one spot of light in each of them. If the spots are very large or the distortions are strong, two spots might overlay or one spot can be located between two squares. Given our beam parameters and our specific hole-array setup this seems unlikely but the problem could then be solved by bringing the mask closer to the CCD. From the mathematical point of view, it is important to have a quite circular spot pattern on the detector due to the orthogonality of the basis functions (in case of Zernike-based analysis).

Detecting the centers
To compute the wavefront, the center of each casted shadow-spot has to be determined. This is achieved by summing over the pixels in x- and y-direction:

$$C_x = \sum_i \frac{x_i I_i}{I_{tot}} \quad \wedge \quad C_y = \sum_j \frac{y_j I_j}{I_{tot}} \tag{4.8}$$

where C_x and C_y are the coordinates of the centers in x- and y-direction, respectively. $I_{i,j}$ is the intensity at pixel x_i or y_j, respectively. By summing over one dimension (x or y) and dividing by the total intensity $I_{tot} = \sum_i I_i$, we compute a numerical mean value for the coordinate in one direction. Using this averaging, it is theoretically possible to achieve sub-pixel resolution for the centers' coordinates. The radius of the beam is normalized to match the unit circle so that the coordinates are scaled to this as well. The so-calculated centers of the spots are then compared to the reference values (corresponding to the centers of the spots from a plane wave). From the difference $\Delta S_{x/y} = S_{x/y} - S_{x0/y0}$ the pointing direction of the wave-vector can be deduced as shown in Fig. 4.6.

Summing up the deviations
Because of $D >> \Delta x$, the far-field approximation can be used and $tan(\alpha) \approx \alpha = \frac{\Delta x}{D}$ (see Fig. 4.6). Using this and $tan(\alpha) = \frac{\Delta z_{x,y}}{a}$ the deviations of the centers of the spots can be transformed into local changes of the wavefront $\Delta z(x, y)$ where a is the center-to-center distance between the holes on the mask.
These small $\Delta z(x, y)$ must now be combined to represent a complete phase mask. Mathematically, this is done by summing over the deviations in x- and y-direction and thus generating one array with the deviations of all spots in x-direction X and one array with the deviations in y-direction Y. By adding the single components one can get the complete wavefront representation. Since the wavefront is continuous, any addition of Δx_{ij}

and Δy_{ij} allows to compute the wavefront at a certain i and j and the result is independent of the way of integration. For simplicity reasons, we used the X_0 or Y_0 rows/columns as illustrated in Fig. 4.9.

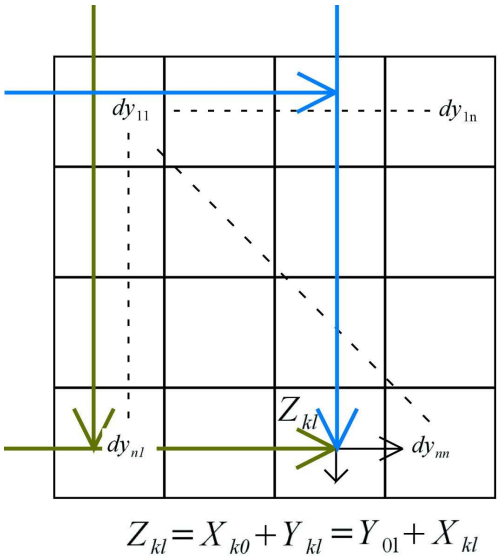

Figure 4.9: The second step of the algorithm combines all $z(x, y)$ from the two directions. This means, that the phase offset at a certain point Z_{kl} is computed by adding up the values of the offsets along the way. Thus the Z_{kl} is independent of the exact path of 'integration' and any chosen way results in the same wavefront offset at the coordinates k and l.

Zernike polynomials

To quantitatively analyze the wavefront of the harmonics, the above-described Zernike polynomials are used as a basis system for the spot pattern. The necessary fitting is done by a Singular Value Decomposition (SVD) algorithm from the Least Square Fit package from LabView 7.1. Unfortunately, this only works reasonable for low-order polynomials. Simulations with spot patters from pure Zernike polynomials (e.g. astigmatism) revealed that different other modes are added to the solution owing to the non-unique hole pattern. This means, that the polynomials are not yet approximated well enough. For example, from a pattern of 30 illuminated holes from the array, the circular rim of the spots is not circular enough. Correspondingly, the error of adding non-existing modes to the solution decreases when more holes are illuminated and for lower-order polynomials. By using an additional fitting routine, these minor inconsistencies could be reduced to a neglectable size.

Alternatively, one can also compute the low-order aberrations from fitting to the derivatives of the Zernike polynomials [126]. The fit is integrated in the end to resolve the complete wavefront. This method is only practical for up to $n = 3$ (astigmatism) because the derivatives of the higher order polynomials are no longer linearly independent. Therefore when a clean high-order aberration is given to this algorithm, additional modes are 'detected'. While with the procedure described above only mathematical fitting errors are contributing to this, this latter technique [126] intrinsically includes non-existing modes as a result. The advantage is probably a higher speed due to lower necessary computing

power.
We chose to evaluate the wavefronts by directly fitting to the Zernike polynomials because computing time is not crucial for our applications yet and the mathematical errors turned out to be controlable. For a closed-loop realization, fitting to the derivatives might actually prove to be the better suited technique if it is considerably faster.

4.2.2 Simulation Results

For the first simulations, we again used our LabView fitting software with idealized spot patterns. This means that the image that is handed to our algorithm contains the centers of the spots already so that it does not have to evaluate them before fitting. Thus different interpretations or deviations of the raw data are excluded to have an impact on the result of the algorithms.
The patterns are generated by calculating the partial derivatives of the Zernike polynomials in x- and y-directions at the centers of the apertures. By arbitrarily choosing the coefficients and thus the amplitude of each mode, the 'integration' process and the fitting routine can be tested. Figure 4.10 shows the front end of the evaluation software with which the patterns are constructed as well as analyzed.

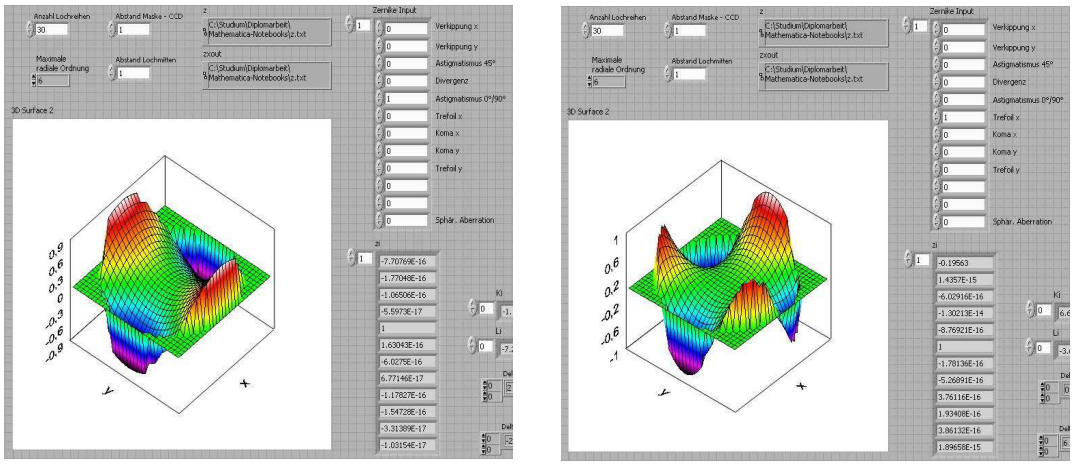

Figure 4.10: Screenshots of the evaluation software front panel for two simulated pure Zernike polynomials. On the left is an astigmatism with different tilts of the phase front in two directions. The right image shows a trefoil aberration. In both cases, the parameters at the top characterize the generated spot pattern, while the lower resulting parameters are the fitted coefficients.

A fairly good agreement between the 'applied' coefficient and the fit results is given. However, for trefoil the first coefficient corresponding to a shift in z-direction is still pronounced. Also, the other coefficients are not null and this leads to the assumption, that the approximation of orthogonality of the basis functions is not necessarily valid. This seems more crucial at higher orders of the polynomials and it seems to depend on the quality of the circular boundary of the pattern. To prove this, simulations were conducted with different amounts of illuminated apertures and the results are given in table 4.2.2.

One can see that even at very high numbers of illuminated apertures (> 100) the 'wrong' coefficients have significant contributions to the fit. As expected this error decreases with increasing spots. Additionally, higher order modes suffer more from virtually added Zernike polynomials than a simple tilt (see Fig. 4.10). For example, at 30 holes per diameter, the false coefficients make up $\approx 8\%$ of the real z_8-mode for a comatic aberration but more than 50% of the real z_{12}-mode for a spherical aberration.

number of holes	z_2	z_4	z_5	z_8	z_9	z_4	z_5	z_{12}
10	0.0496	0.0682	0.1364	1	0	0.4463	1.0909	1
20	0.0136	0.0357	0.0714	1	0	0.2585	0.5714	1
30	0.0062	0.0242	0.0484	1	0	0.1811	0.3871	1
50	0.0023	0.0147	0.0294	1	0	0.1130	0.2353	1
75	0	0.0091	0.0073	0.998	0.002	0.0769	0.1579	1
100	0.0006	0.0074	0.0149	1	0	0.0582	0.1190	1
200	0.0001	0.0037	0.0075	1	0	0.0296	0.0597	1
300	0	0.0025	0.0050	1	0	0.0198	0.0399	1
500	0	0.0015	0.0030	1	0	0.0119	0.0240	1

Table 4.1: Reconstruction of the Zernike coefficients from a comatic aberration (z_8, left table) and from a spherical aberration (z_{12}, right table). Both tables refer to the amount of apertures per line (left column). The initial coefficient is normalized to 1.

To illustrate the influence of illuminated apertures on the fitting quality one can compare a low and a high 'resolution' wavefront each with a pure comatic aberration in Fig. 4.11. Even if the visible quality of the wavefront is quite similar, the coefficients (lower right table in both screen shots) reveal significant differences between the two fit qualities. Again, only $z_8 = 1$ is the initially given parameter for the wavefront distortion.

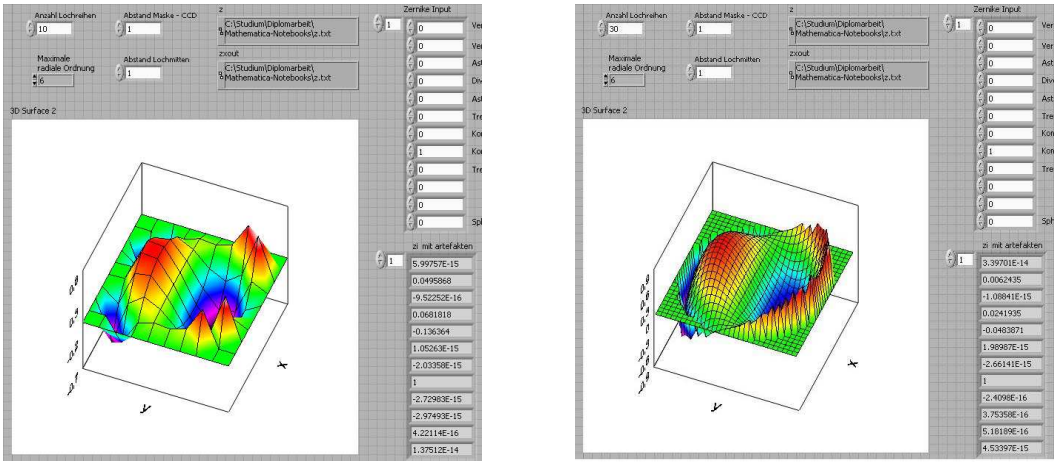

Figure 4.11: Comparison between the same given aberration but analyzed with a different amount of illuminated apertures. The left one uses very few spots while the right corresponds to our setup when the hole array is completely hit by the harmonic beam.

So concluding one can say that the higher the amount of apertures and the lower the order of the Zernike-polynomial distortion, the easier it is to achieve a reasonable fitting result with our evaluation software.
However, one more important insight was gained by the simulations: Since the fit is the best when a smooth circular area of spots is generated, the absolute positioning of the center of the beam on the hole array is also important. We have computed the difference between an even and an odd number of illuminated apertures per diameter of the circle. Interestingly, some 'false' aberration coefficients (astigmatism) can be reduced by 20% while others stay approximately on the same level. This is demonstrated in Fig. 4.12, where some coefficients are plotted with even number of spots (left) or odd number of spots (right), respectively.

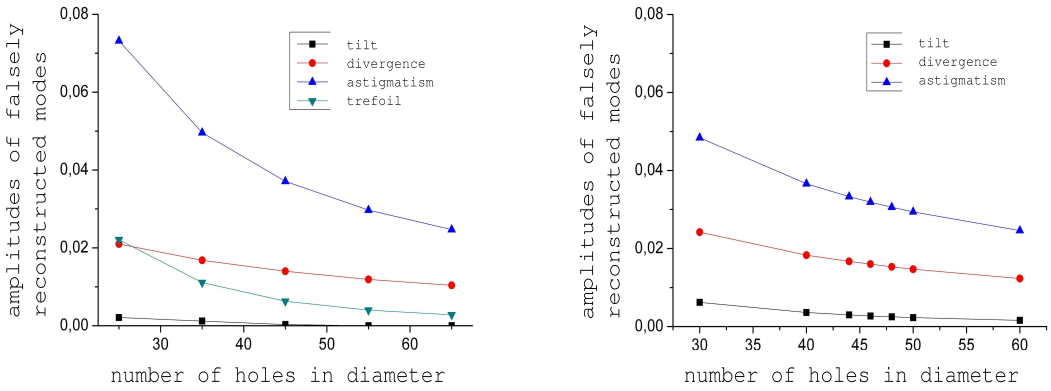

Figure 4.12: On the left are the virtual coefficients plotted versus the number of holes when the diameter always contains an **even** number of spots. The right shows the same plot but with an **odd** number of illuminated spots.

This problem can be solved by careful alignment and an additional pinhole that spatially filters all but a circular central part of the beam.
On the other hand, this would decrease the amount of illuminated apertures and thus decreases the quality of the fit again. A perfect hole array with a radially symmetric orientation could also help to minimize the fitting error but it would complicate the evaluation software significantly.
Last but not least, a certain resolution (regarding the number of spots) is necessary for a detailed description of the wavefront. In these simulations, we always evaluated the spots from one aberration (just one non-zero Zernike coefficient) without any experimental noise. Of course, the presence of more than one aberration is only detectable, if a good resolution can be provided. Therefore we simulated a pure spherical aberration with a coarse mask (left, Fig. 4.13) and with the hole array we are employing in the experiment (right, Fig. 4.13).

Iterative elimination of virtual Zernike polynomials
For better fitting results, it would be desirable to eliminate the non-existing modes from the output of the evaluation software. This is non-trivial, because there is no obvious way

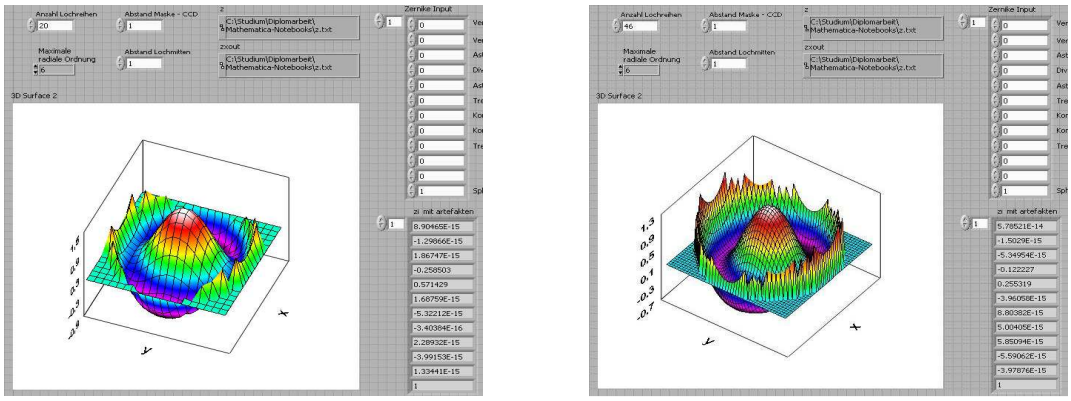

Figure 4.13: Comparison of low-resolution wavefront measurement with pixelation effects at the outer beam area (left) and high-resolution analysis (right).

to tell apart the existing from the misleadingly reconstructed coefficients and real modes must not be deleted. Especially if two basis functions (Zernike polynomials) influence one another, a reasonable correction seems impossible.
After a number of simulations, fortunately, it was found that existant modes of the order n in the worst case only generate artifacts of the order $n-1$. Thus the highest reconstructed orders can be assumed to be characterized correctly which simplifies an iterative 'cleaning' process significantly. A schematic overview of the correction looks as follows:

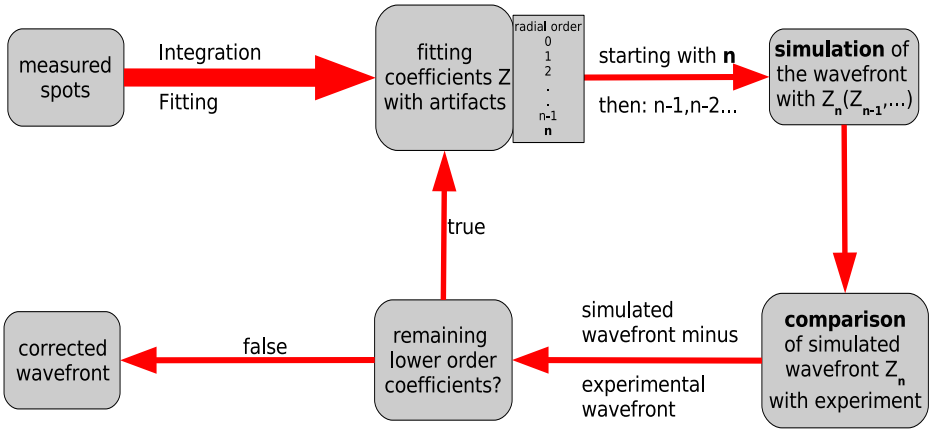

Figure 4.14: Illustration of the iterative cleaning procedure for the reconstructed Zernike polynomial coefficients.

The experimentally reconstructed, highest-order coefficient of the fit is used as the starting parameter for the simulation (see Fig. 4.14). From this simulation one gets the typical artifacts from zeroth to $(n-1)$-th order just like the ones from fitting the experimental data. By subtracting the simulated artifacts from the experimental ones it is possible to

see how adequate the Z_n coefficient is. Thus the first - and highest-order - coefficient n is found and one can go on to the $(n-1)$-th coefficient. This can be continued until there is no difference between the simulated and experimental artifacts because then theoretically the simulation describes the experiment correctly. To check this procedure, more simulations were conducted for a realistic number of apertures (46 on the diameter) which are given in Fig. 4.15. One can see the large improvement after the correction in terms of less 'noisy' Zernike coefficients. The reconstruction accuracy is in the one-tenth-of-a-percent regime and thus the overall precision is increased about three orders of magnitude.

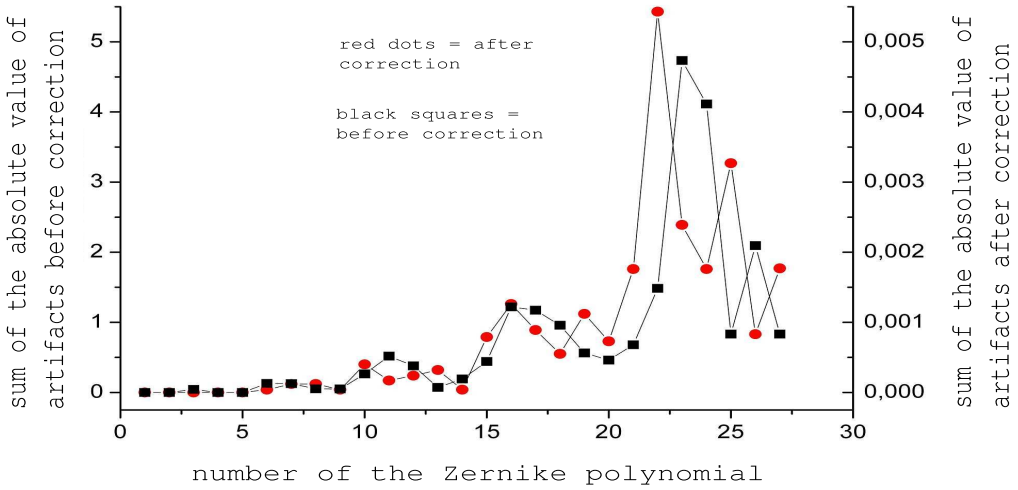

Figure 4.15: Comparison between the absolute values of the artifacts versus number of the Zernike polynomial. The black squares indicate the falsely reconstructed coefficients before the iterative correction and the red dots show the final amplitude of the artifacts. Note the different scales.

For these simulations, the centers of the intensity spots were not computed but given to the algorithm directly and any kind of experimental noise like movement of the source of radiation is not considered.

4.2.3 Experimental Results

To apply our wavefront measurement device, we set it up directly after the XUV generation chamber (see Fig. 4.16), so that the aberrations from the toroidal mirror and possible clipping from differential pumping would not occur. We focus the $500\mu J, 40$fs laser pulses with a fused silica lens ($f = 0.3$m) into the nickel tube, which can be filled arbitrarily with gas. Before this, the laser passes our 2-D SLM in order to be capable of spatial shaping and measuring its impact on the resulting wavefronts. The spectrum of the XUV radiation has constraints (compare section 3.3) which let us assume that the spectrum looks very much like the one measured before with harmonics from the 29th to the 41st order. Such a spectrum is given in Fig 4.17 with a characteristic intensity distribution that depends on the gas and filter material.

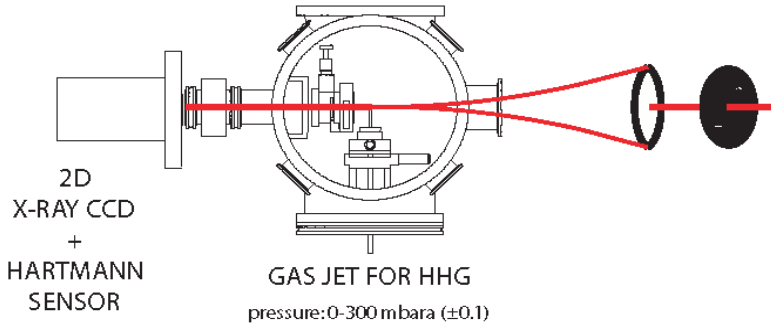

Figure 4.16: Extremely shortened 'beamline' to monitor the high-order harmonics directly after their generation without focusing or collimating devices.

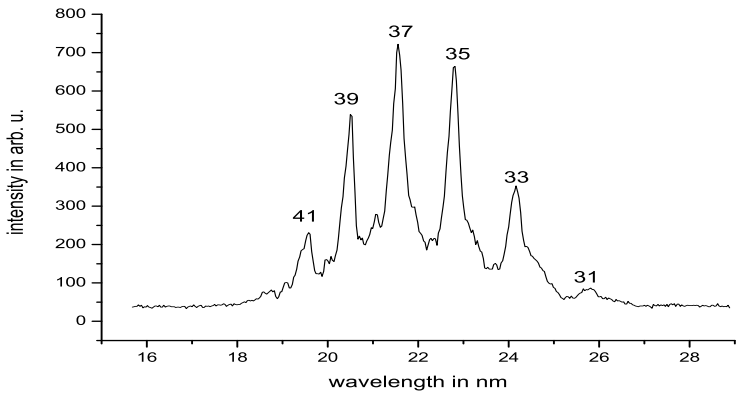

Figure 4.17: Typical harmonic spectrum of the XUV photons used for wavefront measurements and characterization where the numbers correspond to the harmonic order.

Changing the gas pressure

The next step is to characterize the beam profile while changing the gas pressure in the nickel tube. A feedback system allows regulating the pressure in 0.1mbar steps but due to a very time-consuming data evaluation a stepsize of 5mbar was considered reasonable.
In Fig. 4.18, two intensity graphs are plotted versus the gas pressure. Only one has errors bars because the systematic error can be assumed to be the same because both intensities are evaluations of the same data set. One can see a characteristic trend where no harmonics are generated at zero pressure and than the XUV radiation peaks at about 100 to 120 mbar before declining again. The red curve represents the the overall counts of the X-ray CCD camera which corresponds to the total number of photons hitting the detector. The

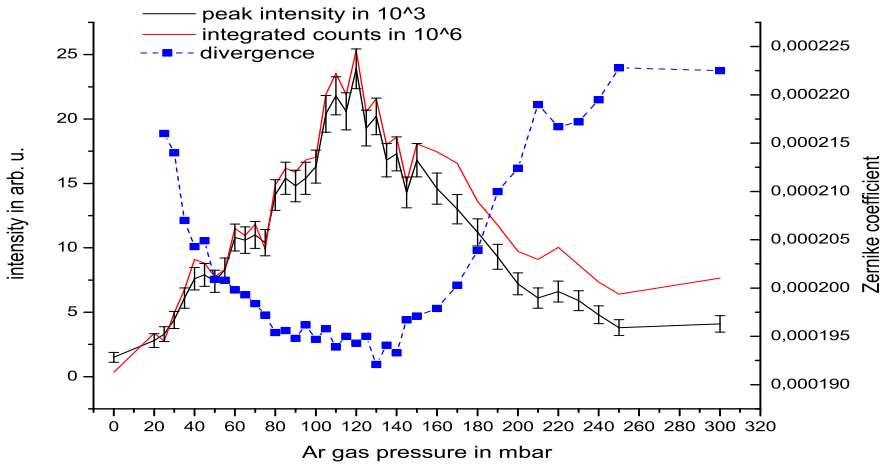

Figure 4.18: Overall photons (red) and peak intensity (black) plotted versus gas pressure. The blue graph shows the divergence of the beam computed with the Hartmann sensor.

black curve with the error bars gives the peak intensity, meaning the highest counts at one pixel on the CCD chip. It is not trivial that both curves have their maxima at roughly the same pressure, which indicates that the optimal pressure in terms of conversion efficiency is also the best in terms of brilliance. This statement is underlined by the third graph in Fig. 4.18 showing the divergence computed from the Hartmann image. Naturally, the generated harmonics have an intrinsic divergence because of the fundamental laser beam being focused into the gas. But apart from this the blue graph shows that a minimum divergence is present in the region from 110 to about 140 mbar which is in agreement with the peak intensity data. Together this leads to the conclusion that - as stated above - the best pressure for the overall harmonic generation provides the best beam quality in the XUV regime, too.

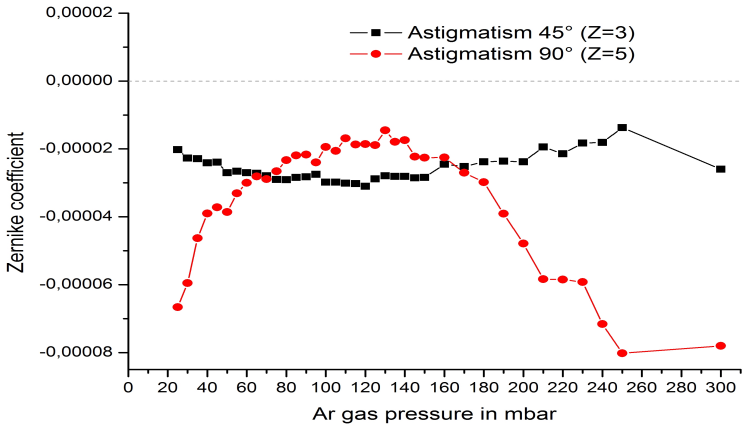

Figure 4.19: This plot shows the behavior of the reconstructed horizontal/vertical (black) and diagonal (red) astigmatism when the gas pressure is changed.

The astigmatism of the harmonic beam in dependency on the gas pressure reveals some interesting behavior (see Fig. 4.19). The black curve (45°-astigmatism) refers to a different divergence of the laser beam along the two diagonal axes; for example, the laser propagates and at one z-position a focus looks like a 'forward slash' and at a second z-position a second focus looks like a 'backslash'. One can see that this abberation remains nearly constant and shows only little 'quadratic' behavior when the pressure is changed. The red curve (90° astigmatism) describes the same 'two-focal-points' phenomenon but this time the foci look like vertical and horizontal bars, respectively. Of course, in both cases the beam profiles at the focal spots do not form an exact bar but more an ellipse-like structure. However, it is important to notice that this second abberation depends much more on the gas pressure and its minimum coincides with the maximum intensity (see Fig. 4.18).

Changing the z-position

The second macroscopically adjustable parameter is the position of the focal spot with respect to the nickel tube. In Fig. 4.16, one can see that by moving the focusing lens along the z-direction one can place the focal spot in arbitrary distances to the gas medium. As described earlier, the focal spot position is very important for phase matching of fundamental and harmonic radiation and offers selectivity over the dominant quantum path (see section 3.1.3).
The z-position at all these measurements refers to the absolute scale of the micrometer table on which the focusing lens is mounted. When the focal spot and the gas-filled nickel tube coincide, we have a z-position of about 9 mm. It is hard to measure this exactly because of the self-focusing effect in air and no easy way to directly measure it in vacuum. Thus, this number is an estimate given with the naked eye and should not be considered absolutely correct.

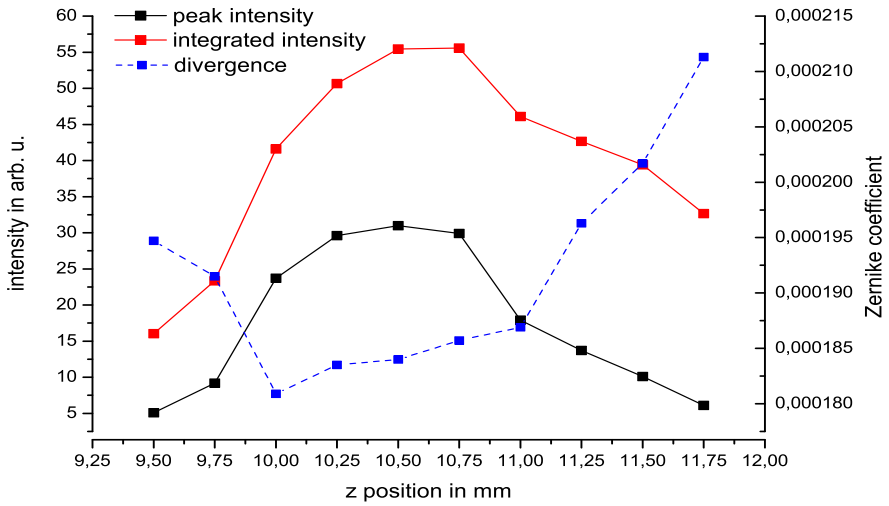

Figure 4.20: Integrated (red, in 10^6 counts) and peak intensity (black, in 10^3 counts) plotted versus the z-position of the focus in respect to the gas tube. The gas tube is located at about 9mm. The blue, dashed graph gives the divergence in dependence on the longitudinal position.

Nevertheless, we know that this 'overlap position' is at lower z numbers and that more millimeters mean moving the focal spot away from the gas.
When we look at the same observables (peak intensity, overall counts and divergence) as before in 4.18, we see a similar behavior with some peculiarities. First, peak intensity and integrated counts are very much alike and differ only in magnitude which is natural. The dashed blue curve depicts the divergence and has a minimum at approximately $z = 10$mm. This aberration does not increase overly towards the maximum counts but at much larger distances between focal spot and gas tube the divergence grows while the harmonic intensity decreases. Interestingly, the counts fall steeper when moving the focal spot towards the gas tube and do not decrease as fast when the lens is moved away from the jet. This can be explained by the importance of phase matching: when going near the gas jet, very little harmonics can be generated efficiently and the optimal conditions require a focus before the interaction medium. Another reason why we can safely assume that bad phase matching is the main reason for the steeper drop closer to the gas is the still acceptable divergence. If the lower count rate were caused by a distorted wavefront, this would have been detected which is not the case.

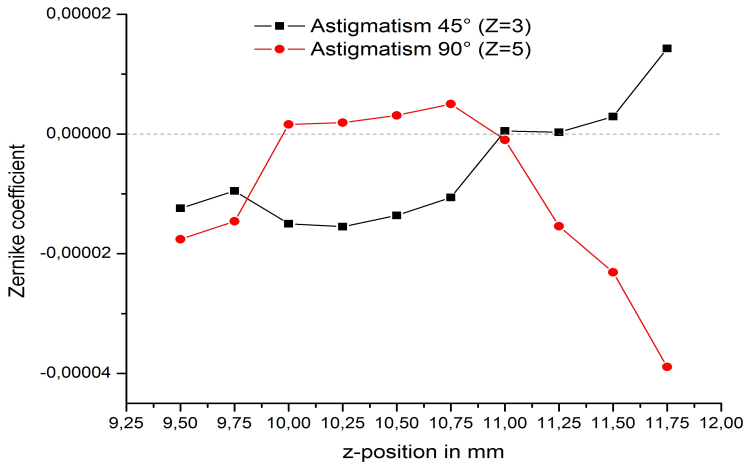

Figure 4.21: Horizontal/vertical (red, 90°) and diagonal (black, 45°) astigmatism plotted at various z positions that correspond to different distances between focal spot and gas jet.

The astigmatisms in Fig 4.21 are not easily interpreted. If we neglect the diagonal one (assuming it is intrinsic in the fundamental beam), the 90°-astigmatism shows a clear plateau between 10.0 and 11.0 millimeters; in this regime the abberation is very little. Going further away from the gas jet, the astimatism grows and probably causes some of the decrease in intensity. When we look at smaller distances, the astimatism is not quite as strong which again indicates that the drop in intensity might be caused by bad phase-matching.
What is unfortunately not visible is the regime where the focus is exactly at and behind the gas jet, because of the too low count rates. We expect to be able to measure this in the next few months and would like to see the influence of the z-position on the wavefront distortion and evaluate its impact on short and long trajectories.

Applying phase masks

We also applied different phase masks with our SLM and reconstructed the harmonic waveforms with the Hartmann sensor. Using extreme values (Zernike coefficients were set equal to one) for astigmatism, tilt, divergence, trefoil, or comatic abberation mostly decreased the detected counts significantly. This can be explained by very poor focus quality and/or shifting the harmonic beam off the CCD chip. In the few cases where an applied wavefront distortion improved the harmonic intensity, we assume that somehow an existing aberration was effectively compensated. This was only the case when the coefficient was not set 1.0 but about 0.1.
If pure aberrations are introduced by the SLM, in almost all cases the reconstruction failed. It was not possible to 'recognize' the applied wavefront distortion by the Hartmann sensor even though divergence and astigmatism had been successfully reconstructed before. This means that either a systematic error in the evaluation process occurred or harmonics do not automatically assume the whole wavefront properties of the fundamental beam. We consider it more likely, that macroscopic parameters have a larger and more systematical effect on the harmonic wavefront than minor spatial shaping. This does not mean that spatially shaping the wavefront would not be a way to improve the XUV output. On the contrary: we could show that spatial shaping can improve the macroscopic parameters (e.g. intensity, see Fig. 4.4) but in this section we learned it cannot automatically influence the wavefront of the harmonics as well.

Summary and outlook

High-order harmonic generation provides a robust and easy-to-handle technique to generate ultrashort light pulses with wavelength down to the water window (2.4-4.2nm). Apart from its usefulness for spectroscopy, coherent control and attosecond physics to name just a few, some fundamental investigations were yet to be conducted. For example, we could show that the comparably new technique of spectral broadening after a filamentation stage allows compression of laser pulses down to about 10fs. A comparison between self-phase modulation in hollow-core fibers and filamentation reveals that each realization brings it's own advantages and disadvantages. The higher throughput and better scalability of a filament on the one hand and better spatial beam quality and less spatial chirp after the capillary on the other hand. However, both techniques allow efficient compression of laser pulses afterwards and the emerging laser pulses are well-suited for HHG.
By the technique of temporal, spatial and spatio-temporal adaptive pulse shaping, to a certain extent the harmonic's properties can be controlled. Formerly, the spectrum of the generated XUV radiation was demonstrated to be controlled arbitrarily by shaping the spectral phase of the fundamental laser pulse. Spatial shaping did not result in any spectral selectivity but it provided a useful tool to counter the spatial inhomogeneities after the filament. These spatially optimized laser pulses revealed a strong increase of the efficiency of the harmonic generation process.
For all the adaptive shaping experiments an evolutionary algorithm was employed that was specifically parameterized to meet the demands of the experiment. A simulation was conducted that benchmarked the newly developed algorithm with the unmodified one. Some changes are clearly improvements and speed up the optimization process while other advances are only of limited use for very specific applications.
Since most of the preceding experiments and simulations are aimed at high-order harmonic generation, XUV radiation was generated and the formerly developed techniques were applied. Besides some optimization of the conversion efficiency, a newly adapted method for wavefront characterization of harmonics was tested. By the use of a Hartmann sensor, the wavefront of an arbitrarily shaped XUV pulse can be analyzed. Because this characterization procedure is not trivial due to experimental and theoretical constraints, an evaluation program was written that solves many of the numerical difficulties. We could show the influence of pressure and position changes on the harmonic output and prove that a high peak intensity corresponds to the best conversion efficiency at the same time. Furthermore, these macroscopic tuning parameters exhibited a more profund and systematic impact on the harmonics' wavefront than spatial phase shaping of the fundamental laser pulse.

What remains to be done is a complete characterization of the spatial (wavefront), spectral (spectrometer) and temporal (see section 3.1.3) properties of the harmonics. From this, one should gain more insight into the complex process itself and be able to optimize the

generated pulse duration, its spatial profile or the conversion efficiency.
The use of a phase shaper for temporally-resolved phase contrast microscopy for example is just one application that yet awaits to be realized. The quite new field of attosecond physics allows for investigation of inner-atomic processes and can greatly benefit from increased conversion efficiencies and spatial characterization methods as well.

This field of physics is a combination of many exciting aspects of material science. It deals with fundamental generation processes of ultrashort light pulses, nonlinear processes in gaseous, fluid or solid matter, and analysis of atoms and molecules with unprecedented high temporal and fairly high spatial resolution. And in a way, a high resolution in every aspect is 'all that matters' for getting to know any existing system that needs to be investigated.

Zusammenfassung und Ausblick

Kurzwellige Laserstrahlen, die durch Frequenzkonversion erzeugten “hohen Harmonischen”, stellen eine zuverlässige und einfach handhabbare Strahlquelle bis hinunter ins “Wasserfenster“ (2,4nm bis 4,2nm) dar. Trotz ihrer vielfältigen bisherigen Anwendungsmöglichkeiten in der Spektroskopie, der kohärenten Kontrolle und der Attosekunden-Physik sind noch einige grundsätzliche Fragen im Bereich der ultrakurzen Laserpulse zu beantworten. Zum Beispiel gelang es uns mit der Filamentierung eine neue Technik zur spektralen Verbreiterung einzusetzen und Laserpulse bis zu 10fs hinunter zu verkürzen. Dabei wurde im Rahmen dieser Arbeit auch ein Vergleich zwischen dieser neuen und der häufig verwendeten gasgefüllten Hohlkern-Kapillare durchgeführt der zeigte, dass beide eine effektive Komprimierung von Laserpulse erlauben und jede Realisierung ihre Vor- und Nachteile mit sich bringt.
Durch zeitliche, räumliche und raumzeitliche, adaptive Pulsformung war es möglich in gewissen Grenzen die Eigenschaften der erzeugten hohen Harmonischen zu kontrollieren. Wie schon vor einiger Zeit demonstriert wurde, kann man die spektrale Struktur der generierten Strahlung durch geeignete Modulation der spektralen Phase des erzeugenden Laserpulses verändern. Durch räumliche Formung der Phasenfront der Pulse war zwar keine Selektivität der Harmonischen zu erreichen, allerdings erwies sie sich als probates Mittel um Inhomogenitäten im Strahlprofil auszugleichen. Auf diese Weise war eine Verbesserung des Harmonischenintensität um fast eine Grössenordnung möglich.
Bei all diesen ”Pulsformungs“-Experimenten griffen wir auf einen evolutionären Algorithmus zurück, der genau für diese Zwecke von uns geschrieben beziehungsweise weiterentwickelt wurde. Verbesserungen am Berechnungsprozedere konnten durch Simulationen verifiziert werden und dienten uns bei den weiteren Experimenten als Optimierungshilfe. Dabei waren selbstverständlich nicht alle neu eingeführten Parameter bei allen Fragestellungen hilfreich und es stellte sich heraus, dass für die optimale Lösung eines jeden Problems eine kleine Anpassung des Algorithmus nötig ist.
Da fast alle vorherigen Experimente darauf ausgerichtet waren in irgendeiner Weise die Erzeugung der hohen Harmonischen nach gewissen Kriterien zu verbessern, wurde im Vakuum eine XUV-Strahlquelle realisiert. Neben einer verbesserten Konversionseffizienz konnten wir auch ein neues Verfahren zur Wellenfrontvermessung im XUV-Bereich testen. Da die Auswertung dieser Messmethode sehr aufwendig ist, wurde sie mittels eigener Software durchgeführt, die auch einige numerische Schwierigkeiten ausräumen konnte. Als Ergebnis konnten wir den Einfluss von Gasdruck und Längsposition des Wechselwirkungsbereichs auf die erzeugten Harmonischen vermessen. Es ergab sich, dass beste Konversionseffizienz und maximale Spitzenintensität bei fast gleichen Bedingungen auftreten. Die Parameter Gasdruck und Längsposition stellten sich auch als systematischer und stabiler heraus als eine Veränderung der räumlichen Phase des Laserpulses.

Noch ausstehende Messungen umfassen die komplette Charakterisierung der räumlichen

(Wellenfront), spektralen (Spektrometer) und zeitlichen (siehe Abschnitt 3.1.3) Eigenschaften der Harmonischen. Dadurch sollte man mehr Einblick in den komplexen Erzeugungsprozess selbst und eventuelle Optimierungsmöglichenkeiten gewinnen. Die Verwendung eines Phasenformers für zeitaufgelöste Phasenkontrastmikroskopie ist dabei nur eine vielversprechende neue Anwendung. Das relativ neue Feld der Attosekundenphysik erlaubt die Untersuchung der inneratomaren Prozesse und profitiert selbstverständlich auch von verbesserter Konversionseffizienz und räumlicher Charakterisierung des XUV-Pulses.

Dieses Arbeitsfeld der Physik stellt sich als Kombination von vielen interessanten Aspekten der "Werkstoffkunde" im allgemeinsten Sinn dar: Es befasst sich mit grundliegenden laserphysikalischen Umwandlungsprozessen, nichtlinearer Lichtwechselwirkung mit gasförmiger, flüssiger und fester Materie und Analyse von Atomen und Molekülen mit höchstmöglicher zeitlicher und hoher räumlicher Präzision. Und - wie schon in der Einleitung geschrieben - eine hohe Auflösung in jeder Dimension ist ein entscheidender Vorteil bei der wissenschaftlichen Erforschung von Systemen aller Art.

Appendix A

Pulse Shaper

The spatial light modulator used in this work is a Hamamatsu Photonics PAL-SLM X8267 with an addressable resolution of 768x768 pixels. The device is a reflective shaper that receives its mask from a LCD (1024x768 pixels) that is illuminated by a laser diode. The desired phase mask is fed to the LCD unit and then imaged onto a thin layer of hydrogenated, amorphous silicon ($\alpha Si : H$).

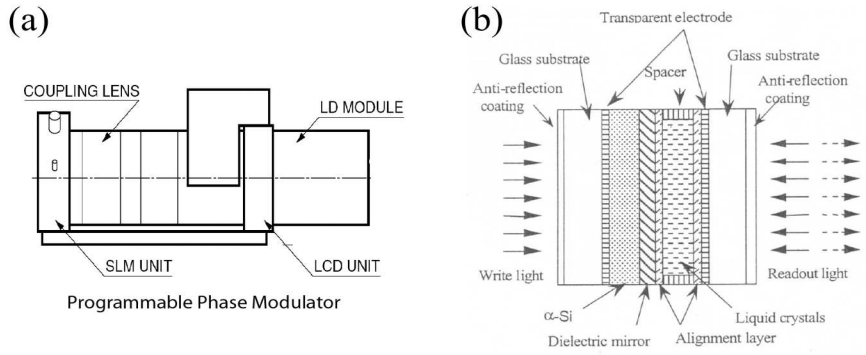

Figure A.1: (a) is a side view of the pulse shaper shown in 2.1. It consists of the laser diode that illuminates a LCD unit from where the picture is imaged onto the SLM unit via the coupling lens. (b) shows only the front part - the SLM unit - which is described in the text below.

This special material has an intensity-dependent dielectric constant and thus the local $\epsilon_r(I)$ can be modulated. Because of a driving voltage applied between the Si-layer and the LCD-layer on the other side of the dielectric mirror, the LCD is influenced by the light incident on the 'rear' part (see (b) in A.1). The liquid crystals are parallelly aligned and with a voltage they tilt and change the refractive index with essentially no rotation along the optical axis. Thus, linearly polarized light will be phase-modulated if parallel to the liquid crystals and no polarization change is induced. With this technique we can image a phase mask given to the LCD unit to the 'front' part and thus to the laser beam without pixelation. Between 700-900nm the reflectivity for the readout light is above 95% and therefore we can best shape the pulses before spectral broadening. After a filament or gas-filled capillary, the spectra are sometimes too broad for optimal phase modulation. The smoothness of the active area is also enhanced because of a slightly blurry projection

of the 1024x768 pixels of the LCD to the 768x768 pixels of the SLM. This results in a link between neighboring pixels and thus large phase jumps extend over a few pixels.
To test this, a stripe-like phase pattern with $0\pi - 3\pi - 0\pi - 3\pi$ and so on was applied to the phase mask. One can see from A.2 that such a steep gradient seems to influence 2-3 pixels which then deflect the incident light. This results in the visible cuts in the spectrum at the transition from one phase to another. Very interesting is the increase of the spectral intensity in parts of the spectrum, here in section 5 and 7 of the phase mask (in Fig. A.2). This effect can be contributed to a change of the polarization of the laser beam due to interaction with the modulation area. A twisted polarization leads to reduced transmission through the whole setup. From A.2 (b) one can see that this effect is very dominant at zero offset (write light is weak/off). Then the strong readout-light (the IR-laser) will act as a write light itself and affect the PAL-SLM and change the polarization. When the input level is 255 (corresponds to green, 3π, and a strong write light), the laser diode will overrule this effect and dominates the modulation. As long as this is the case the polarization is nearly unchanged and the transmission is high.

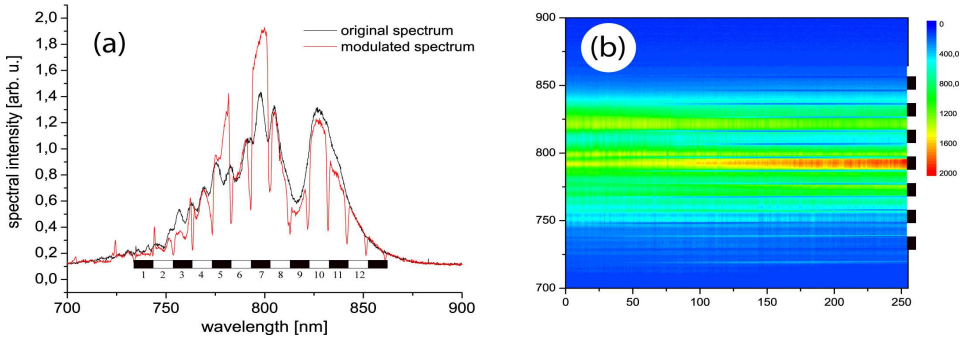

Figure A.2: On the left is a spectrum plotted with and without applying an alternating mask of zero and maximum phase offset. This was realized in the temporal shaping geometry. In black is the original spectrum and in red is the spectrum after modulation of the phase. The bar below the spectrum indicates where the input level was 0 (white, corresponding to 0π) and 255 (black, corresponding to 3π). In (b) is the spectrum plotted versus the modulation depth to show that this phenomenon really depends on the SLM.

As already mentioned, a downside of the optical backlight writing is the fact that transmitted light from the readout side can 'self-modulate' its phase.

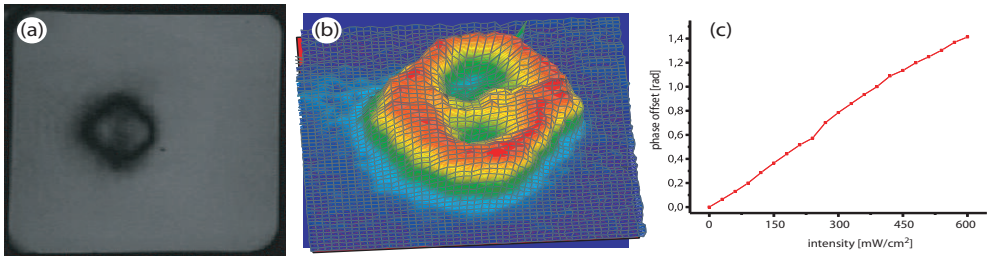

Figure A.3: SPM from the SLM is given in (a) and (b) when the incident laser is acting as a 'write-light'. In (c) is the phase offset as a function of intensity.

This effect seems to be very strong when no write light is applied. Therefore we let the laser beam hit the active area without any signal from the write light and measured the phase change (see Fig. A.3) employing a second laser. As shown before, the laser diode is able to compensate this self-phase modulation of the laser beam, but still it is important for no-offset measurements. Another intrinsic problem is the fact, that the phase modulation depends on the wavelength and thus a certain applied phase will result in different offsets for the different frequencies. Nevertheless, this SLM proved to be a useful tool in this work and its high resolution in Fig. A.4 is a step in the direction of high versatility and sensitivity.

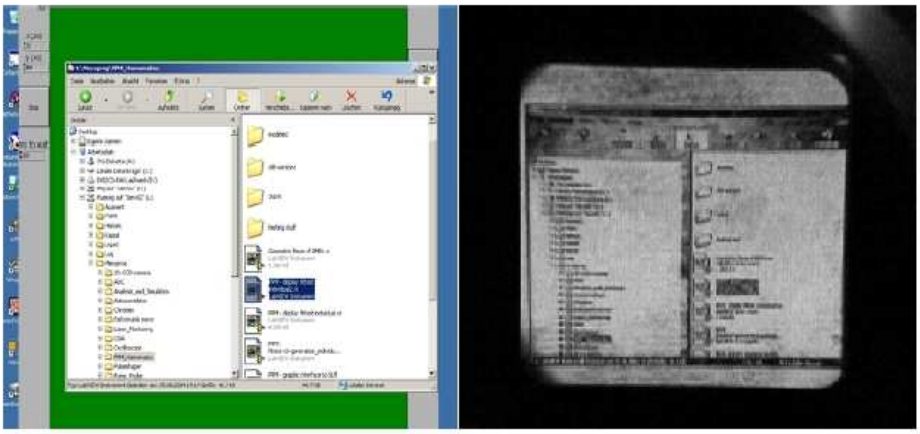

Figure A.4: On the right is the intensity modulation of the Windows Explorer picture on the left. Even small details are visible and the limiting factor of this image was the low resolution of the CCD camera.

During this work no permanent damage of the SLM was detected, so the damage threshold for 10fs laser pulses is assumed to be $> 3.5 \times 10^{10} W/cm^2$. The technical problems described here and more tests and calibration measurements have been studied in detail in [50].

List of Figures

Bibliography

[1] J.Seres, E.Seres, A.J.Verhoef, G.Tempea, C.Streli, P.Wobrauschek, V.Yakolev, A.Scrinzi, C.Spielmann, and F.Krausz. Source of coherent kiloelectronvolt x-rays. *Nature*, 433:596, 2005.

[2] Christian Spielmann, Clarence Kan, Neal H. Burnett, Thomas Brabec, Michael Geissler, Armin Scrinzi, Matthias Schnürer, and Ferenc Krausz. Near-kev coherent x-ray generation with sub-10-fs lasers. *IEEE Journal of selected topics in quantum electronics*, 4(2), March 1998.

[3] J.-C. Diels and W.Rudolph. *Ultrashort Laser Pulse Phenomena*. Academic Press, London, 1996.

[4] J.D.Jackson. *Classical Electrodynamics*. John Wiley and Sons, Inc., New York, 3 edition, 1999.

[5] L. Bergmann and C. Schaefer. *Optik, volume 3 of Lehrbuch der Experimentalphysik*. Walter de Gruyter, Berlin, 10 edition, 2004.

[6] E.T.J.Nibbering, P.F.Curley, G.Grillon, B.S.Prade, M.A.Franco, F.Salin, and A.Mysyrowicz. Conical emission from self-guided femtosecond pulses in air. *Optics Letters*, 62, 1996.

[7] A.Couairon. Filamentation lengths of powerful laser pulses. *Applied Physics B*, pages 789–792, 2003.

[8] C.P.Hauri, W.Kornelis, F.W.Helbing, A.Heinrich, A.Couairon, A.Mysyrowics, J.Biegert, and U.Keller. Generation of intense, carrier-envelope phase-locked few-cycle laser pulses through filamentation. *Applied Physics B*, 79:673–677, 2004.

[9] J.Kasparian, M.Rodriguez, G.Méjean, J.Yu, E.Salmon, H.Wille, R.Bourayou, S.Frey, Y.B.André, R.Sauerbrey, J.-P. Wolf, and L.Wöste. White-light filaments for atmospheric analysis. *Science*, 301:61, July 2003.

[10] J.Philip, C.D.Amico, G.Chériaux, A.Couairon, B.Prade, and A.Mysyrowicz. Amplification of femtosecond laser filamentation in ti:sapphire. *Physical Review Letters*, 95(163901), October 2005.

[11] A.Dubietis, A.Couairon, E.Kučinskas, G.Tamošauskas, E.Gaižauskas, D.Faccio, and P.DiTrapani. Measurement and calculation of nonlinear absorption associated with femtosecond filaments in water. *Applied Physics B*, 84:439–446, 2006.

[12] Gadi Fibich, Shmuel Eisenmann, Boaz Ilan, and Arie Zigler. Control of multiple filamentation in air. *Optics Letters*, 29(15), 2004.

[13] W.Liu, J.F.Gravel, F.Théberge, A.Becker, and S.L.Chin. Background reservoir: its crucial role for long-distance propagation of femtosecond laser pulses in air. *Applied Physics B*, 80(7), June 2005.

[14] Ting-Ting Xi, Xin Lu, and Jie Zhang. Interaction of light filaments generated by femtosecond laser pulses in air. *Physical Review Letters*, 96(025003), January 2006.

[15] O.G.Kosareva, N.A.Panov, N.Akozbek, V.P.Kandidov, Q.Luo, S.A.Hosseini, W.Liu, J.-F.Gravel, G.Roy, and S.L.Chin. Controlling a bunch of multiple filaments by means of a beam diameter. *Applied Physics B*, 82:111–122, 2005.

[16] Taylor D. Grow and Alexander L. Gaeta. Dependence of multiple filamentation on beam ellipticity. *Optics Express*, 13(12), 2005.

[17] Dominik Walter, Stefan Eyring, Jan Lohbreier, Robert Spitzenpfeil, and Christian Spielmann. Spatial optimization of filaments. *Applied Physics B*, 88(2), 2007.

[18] M.A.Porras, A.Dubietis, A.Matijošius, R.Piskarskas, F.Bragheri, A.Averchi, and P. Di Trapani. Characterization of conical emission of light laments in media with anomalous dispersion. *Journal of the Optical Society of America B*, 24(3), 2007.

[19] online. Wikipedia. *http://www.wikipedia.org*, 2008.

[20] P.Dombi, A.Apolonski, Ch.Lemell, G.G.Paulus, M.Kakehata, R.Holzwarth, Th.Udem, T.Torizuka, J.Burgdörfer, T.W.Hänsch, and F.Krausz. Direct measurement and analysis of the carrier-envelope phase in light pulses approaching the single-cycle regime. *New Journal of Physics*, 6(39), 2004.

[21] Richard Ell, Jonathan R. Birge, Mohammad Araghchini, and Franz X. Kärntner. Carrier-envelope phase control by a composite plate. *Optics Express*, 14(12), May 2006.

[22] G.Sansone, E.Benedetti, J.-P.Caumes, S.Stagira, C.Vozzi, M.Pascolini, L.Poletto, P.Villoresi, S.De Silvestri, and M.Nisoli. Measurement of harmonic phase differences by interference of attosecond light pulses. *Physical Review Letters*, 94(193903), March 2005.

[23] Takao Fuji, Jens Rauschenberger, Christoph Gohle, Alexander Apolonski, Thomas Udem, Vladislav S. Yakovlev, Gabriel Tempea, Theodor W. Hänsch, and Ferenc Krausz. Attosecond control of optical waveforms. *New Journal of Physics*, 7(116), 2005.

[24] Markus Drescher and Ferenc Krausz. Attosecond physics: facing the wave-particle dualism. *Journal of Physics B*, 38:727–740, 2005.

[25] E.Goulielmakis, V.A.Yakovlev, A.L.Cavalieri, M.Uiberacker, V.Pervak, A.Apolonski, R.Kienberger, U.Kleineberg, and F.Krausz. Attosecond control and measurement: Lightwave electronics. *Science*, 2007.

[26] P.Agostini and L.F.DiMauro. The physics of attosecond light pulses. *Repetitions of Modern Physics*, 2004.

[27] Y.M.Li and R.Fedosejevs. Ionization-induced blue shift of krf laser pulses in an underdense plasma. *Physical Review E*, pages 2166–2169, 1995.

[28] Wm.M.Wood, C.W.Siders, and M.C.Downer. Measurement of femtosecond ionization dynamics of atmospheric density gases by spectral blueshifting. *Physical Review Letters*, 67(25), December 1991.

[29] William M. Wood, Glenn Focht, and M.C.Downer. Tight focusing and blue shifting of millijoule femtosecond pulses from a conical axicon amplifier. *Optics Letters*, 13(11), November 1988.

[30] online. Bragg mirrors. *http://www.rp-photonics.com/bragg_mirrors.html*, 2008.

[31] Robert Szipöcs, Kárpát Ferencz, Christian Spielmann, and Ferenc Krausz. Chirped multilayer coatings for broadband dispersion control in femtosecond lasers. *Optics Letters*, 19(3), February 1994.

[32] Kyung-Han Hong, Yong Soo Lee, and Chang Hee Nam. Electric-field reconstruction of femtosecond laser pulses from interferometric autocorrelation using an evolutionary algorithm. *Optics Communications*, 271:169–177, 2007.

[33] Chris Iaconis and Ian A. Walmsley. Spectral phase interferometry for direct electric-field reconstruction for ultrashort optical pulses. *Optics Letters*, 23(10):781–783, May 1998.

[34] R.Trebino, K.W.Delong, D.N.Fittinghoff, J.N.Sweetser, M.A.Krumbugel, B.A.Richman, and D.J.Kane. Measuring ultrashort laser pulses in the time-frequency domain using frequencyresolved optical gating. *Review of Scientific Instruments*, 68(32773295), 1997.

[35] G.Stibenz, C.Ropers, Ch.Lienau, Ch.Warmuth, A.S.Wyatt, I.A.Walmsley, and G.Steinmeyer. Advanced methods for the characterization of few-cycle laser pulses: a comparison. *Applied Physics B*, 2006.

[36] A.J.DeMaria, C.M.Ferrar, and J.G.E. Danielson. Mode locking of a nd3+-doped glass laser. *Applied Physics Letters*, 8:22–24.

[37] P.F.Moulton. Spectroscopic and laser characteristics of ti:al2o3. *Journal of the Optical Society of America B*, 3(125), 1986.

[38] John-Mark Hopkins and Wilson Sibbett. Big payoffs in a flash. *Scientific American*, pages 73–79, 2000.

[39] T.Wilhelm, J.Piel, and E.Riedle. Sub-20-fs pulses tunable across the visible from a blue-pumped single-pass noncollinear parametric converter. *Optics Letters*, 1997.

[40] A.Assion, M.Geisler, J.Helbing, V.Seyfried, and T.Baumert. Femtosecond pump-probe photoelectron spectroscopy: Mapping of vibrational wave-packet motion. *Physica Review A*, 1996.

[41] A.Assion, T.Baumert, J.Helbing, V.Seyfried, and G.Gerber. Coherent control by a single phase shaped femtosecond laser pulse. *Chemical Physics Letters*, 1996.

[42] H.Ihee, J.Cao, and A.H.Zewail. Ultrafast electron diffraction: structures in dissociation dynamics of fe(co)(5). *Chemical Physics Letters*, 1997.

[43] M.Aeschlimann, Michael Bauer, Daniela Bayer, Tobias Brixner, F.Javier Garcia de Abajo, Walter Pfeiffer, Martin Rohmer, Christian Spindler, and Felix Steeb. Adaptive subwavelength control of nano-optical fields. *Nature*, 2007.

[44] T.Udem, R.Holzwartz, and T.W.Hänsch. Optical frequency metrology. *Nature*, 2002.

[45] S.Diddams, D.Jones, J.Ye, S.T.Cundiff, J.L.Hall, J.Ranka, R.Windeler, R.Holzwarth, T.Udem, and T.Hänsch. Direct link between optical and microwave frequencies with a 300thz femtosecond laser comb. *Physical Review Letter*, 2000.

[46] Juan J. Carrera, X.M. Tong, and Shih-I Chu. Creation and control of single coherent attosecond xuv pulse by few-cycle intense laser pulses. *Physical Review A*, 74(023404), 2006.

[47] G.Sansone, E.Benedetti, F.Calegari, C.Vozzi, L.Avaldi, R.Flammini, L.Poletto, P.Villoreso, C.Altucci, R.Velotta, S.Stagira, S. De Silvestri, and M.Nisoli. Isolated single-cycle attosecond pulses. *Science*, 314:443–446, October 2006.

[48] M.Hentschel, R.Kienberger, Ch.Spielmann, G.A.Reider, N.Milosevic, T.Brabec, P.Corkum, U.Heinzmann, M.Drescher, and F.Krausz. Attosecond metrology. *Nature*, 2001.

[49] M.Uiberacker, Th.Uphues, M.Schultze, A.J.Verhoef, V.Yakovlev, M.F.Kling, J.Rauschenberger, N.M.Kabachnik, H.Schröder, M.Lezius, K.L.Kompa, H.-G. Muller, M.J.J.Vrakking, S.Hendel, U.Kleineberg, U.Heinzmann, M.Drescher, and F.Krausz. Attosecond real-time observation of electron tunneling in atoms. *Nature*, 446(5), April 2007.

[50] Ron Kemmer. Adaptive räumliche und zeitliche formung von ultrakurzen laserpulsen. Diplomarbeit Universität Würzburg, 2005.

[51] Frank Dimler. Adaptive formung von laserpuls-spektren im mittleren infrarot. Diplomarbeit Universität Würzburg.

[52] A.M.Weiner. Femtosecond pulse shaping using spatial light modulators. *Review of Scientific Instruments*, 71(5):1929–1960, 2000.

[53] K.Yamane, Z.G.Zhang, K.Oka, R.Morita, M.Yamashita, and A.Suguro. Optical pulse compression to 3.4fs in the monocycle region by feedback phase compensation. *Optics Letters*, 2003.

[54] B.Schenkel, J.Biegert, U.Keller, C.Vozzi, M.Nisoli, G.Sansone, S.Stagira, S.DeSilvestri, and O.Svelto. Generation of 3.8-fs pulses from adaptive compression of a cascaded hollow fiber supercontinuum. *Optics Letters*, 2003.

[55] A.Guandalini, P.Eckle, P.Schlup, J.Biegert, and U.Keller. 5.1 fs pulses generated by filamentation and carrier envelope phase stability analysis. *Journal of Physics B*, 39:257–264, 2006.

[56] C.P.Hauri, A.Trisorio, M.Merano, R.B.Lopez-Martens, and G.Mourou. Generation of high-fidelity, down-chirped sub-10 fs mj pulses through filamentation for driving relativistic laser-matter interactions at 1khz. *Applied Physics Letters*, 89(151125), 2006.

[57] A.Zaïr, A.Guandalini, F.Schapper, M.Holler, J.Biegert, L.Gallmann, U.Keller, A.Couairon, M.Franco, and A.Mysyrowicz. Spatio-temporal characterization of few-cycle pulses obtained by filamentation. *Optics Express*, 15(9), 2007.

[58] Sergei A. Trushin, Kyriaki Kosma, Werner Fuß, and Wolfram E. Schmid. Sub-10-fs supercontinuum radiation generated by filamentation of few-cycle 800 nm pulses in argon. *Optics Letters*, 32(16), August 2007.

[59] Xiaowei Chen, Xiaofang Li, Jun Liu, Pengfei Wei, Xiaochun Ge, Ruxin Li, and Zhizhan Xu. Generation of 5 fs, 0.7 mj pulses at 1khz through cascade filamentation. *Optics Letters*, 32(16), August 2007.

[60] Gero Stibenz, Nickolai Zhavoronkov, and Günter Steinmeyer. Self-compression of millijoule pulses to 7.8 fs duration in a white-light filament. *Optics Letters*, 31(2), 2006.

[61] S.A.Trushin, S.Panja, K.Kosma, W.E.Schmid, and W.Fuß. Supercontinuum extending from 1000 to 250nm, generated by focusing ten-fs laser pulses at 805nm into ar. *Applied Physics B*, 80:399–403, 2005.

[62] Hui Yang, Jie Zang, Qiuju Zhang, Zuoqiang Hao, Yutong Li, Zhiyuang Zheng, Zheng Wang, Quanli Dong, Xin Lu, Zhiyi Wei, and Zhengming Sheng. Polarization-dependent supercontinuum generation from light filaments in air. *Optics Letters*, 30:534–536, 2005.

[63] F.Théberge, W.Liu, Q.Luo, and S.L.Chin. Ultrabroadband continuum generated in air (down to 230nm) using ultrashort and intense laser pulses. *Applied Physics B*, 80(2):221–225, 2005.

[64] Lukas Gallmann, T.Pfeifer, P.M.Nagel, M.J.Abel, D.M.Neumark, and S.R.Leone. Comparison of the filamentation and the hollow-core fiber characteristics for pulse compression into the few-cycle regime. *Applied Physics B*, 86:561–566, 2007.

[65] Thomas Pfeifer, Lukas Gallmann, Mark J. Abel, Daniel M. Neumark, and Stephen R. Leone. Circular phase mask for control and stabilization of single optical filaments. *Optics Letters*, 31(15), August 2006.

[66] K. Levenberg. A method for the solution of certain problems in least squares. *Quarterly of Applied Mathematics*, 1944.

[67] D. Marquardt. An algorithm for least-squares estimation of nonlinear parameters. *SIAM Journal of Applied Mathematics*, 1963.

[68] Jens Biegert and Andreas Becker. Salamanca, spain, june 2006 and dresden; germany, august 2007. private communications.

[69] Laurent Moreaux, Olivier Sandre, Serge Charpak, Mireille Blanchard-Desce, and Jerome Mertz. Coherent scattering in multi-harmonic light microscopy. *Biophysical Journal*, 2001.

[70] J.-F. Hergott, M.Kovačev, H.Merdji, C.Hubert, Y.Mairesse, E.Jean, P.Breger, P.Agostini, B.Carré, and P.Salières. Extreme-ultraviolet high-order harmonic pulses in the microjoule range. *Physical Review A*, 2002.

[71] S.Kazamias, D.Douillet, F.Weihe, C.Valentin, A.Rousse, S.Sebban, XXX Grillon, F.Augé, D.Hulin, and P.Balcou. Global optimization of high harmonic generation. *Physical Review Letters*, 2003.

[72] M.Ferray, A.L'Huillier, X.F.Li, L.A.Lompré, G.Mainfray, and C.Manus. Multiple-harmonic conversion of 1064nm radiation in rare gases. *Journal of Physics B*, 1988.

[73] B.Sheely, J.D.D.Martin, L.F.DiMauro, P.Agostini, K.J.Schafer, M.B.Gaarde, and K.C.Kulander. High harmonic generation at long wavelengths. *Physical Review Letters*, 1999.

[74] Thomas Brabec and Ferenc Krausz. Intense few-cycle laser fields: Frontiers of nonlinear optics. *Reviews of Modern Physics*, 72(2):545–590, April 2000.

[75] P.B.Corkum. Plasma perspective on strong-field multiphoton ionization. *Physical Review Letters*, 71(13), September 1993.

[76] S.August, D.D.Meyerhofer, D.Strickland, and S.L.Chin. Laser ionization of noble gases by coulomb-barrier suppression. *Journal of the Optical Society of America B*, 1991.

[77] L.V.Keldysh. Ionization in the field of a strong electromagnetic wave. *Soviet Physics JETP*, 1965.

[78] Kenneth J. Schafer and Kenneth C. Kulander. Phase-dependent effects in multiphoton ionization induced by a laser field and its second harmonic. *Physical Review A*, 1992.

[79] Gennady L. Yudin and Misha Yu Ivanov. Nonadiabatic tunnel ionization: Looking inside a laser cycle. *Physical Review A*, 2001.

[80] Ariel Gordon and Franz X. Kärtner. Quantitative modeling of single atom high harmonic generation. *Physical Review Letters*, 59(223901), November 2005.

[81] Thomas Pfeifer, Lukas Gallmann, Mark J. Abel, Phillip M. Nagel, Daniel M. Neumark, and Stephen R. Leone. Heterodyne mixing of laser fields for temporal gating of high-order harmonic generation. *Physical Review Letters*, 97(163901), October 2006.

[82] M.Lewenstein, Ph.Balcou, M.Yu.Ivanov, Anne L'Huillier, and P.B.Corkum. Theory of high-harmonic generation by low-frequency laser fields. *Physical Review A*, 49(2), March 1994.

[83] K.J.Schafer, B.Yang, L.F.DiMauro, and K.C.Kulander. Above threshold ionization beyond the high harmonic cutoff. *Physical Review Letters*, 1993.

[84] R.Bartels, S.Backus, E.Zeek, L.Misoguti, G.Vdovin, I.P.Christov, M.M.Murnane, and H.C.Kapteyn. Shaped-pulse optimization of coherent emission of high-harmonic soft x-rays. *Nature*, 406:164–166, July 2000.

[85] I.P. Christov, R.Bartels, H.C.Kapteyn, and M.M.Murnane. Attosecond time-scale intra-atomic phase matching of high harmonic generation. *Physical Review Letters*, 2001.

[86] T.Pfeifer, D.Walter, C.Winterfeldt, C.Spielmann, and G.Gerber. Controlling the spectral shape of coherent soft x-rays. *Applied Physics B*, 80:277–280, 2005.

[87] Thomas Pfeifer, Ron Kemmer, Robert Spitzenpfeil, Dominik Walter, Carsten Winterfeldt, Gustav Gerber, and Christian Spielmann. Spatial control of high-harmonic generation in hollow fibers. *Optics Letters*, 30(12), 2005.

[88] Ivan P. Christov, Henry C. Kapteyn, and Margaret M. Murnane. Quasi-phase matching of high-harmonics and second pulses in modulated waveguides. *Optics Express*, 7(11), November 2000.

[89] H.Merdji, M.Kovačev, W.Boutu, P.Salières, F.Vernay, and B.Carré. Macroscopic control of high-order harmonics quantum-paths components for the generation of attosecond pulses. *Physical Review A*, 74(043804), 2006.

[90] P.Sali'ères, B.Carré, L.LeDéroff, F.Grasbon, G.G.Paulus, H.Walther, R.Kopold, W.Becker, D.B.Milosević, A.Sanpera, and M.Lewenstein. Feynman's path-integral approach for intense-laser-atom interactions. *Science*, 2001.

[91] M.B.Gaarde, F.Salin, E.Constant, P.Balcou, K.J.Schafer, K.C.Kulander, and A.L'Huillier. Spatiotemporal separation of high haromnics radiation into two quantum path components. *Physical Review A*, 1999.

[92] P.Balcou, A.S.Dederichs, M.B.Gaarde, and A.L'Huillier. Quantum-path analysis and phase matching of high-order harmonic generation and high-order frequency mixing processes in strong laser fields. *Journal of Physics B*, 1999.

[93] D.G. Lee, J.H.Kim, K.H.Hong, and C.H.Nam. Coherent control of high-order harmonics with chirped femtosecond laser pulses. *Physica Review Letters*, 2001.

[94] H.T.Kim, D.G.Lee, K.H.Hong, J.H.Kim, I.W.Choi, and C.H.Nam. Continuously tunable high-oder haromincs from atoms in an intense femtosecond laser field. *Physical Review A*, 2003.

[95] P.M.Paul, E.S.Toma, P.Breger, G.Mullot, F.Augé, Ph. Balcou, H.G.Muller, and P.Agostini. Observation of a train of attosecond pulses from high harmonic generation. *Science*, 2001.

[96] E.P.Benis, P.Tzallas, L.A.A.Nikopoulos, M.Kovačev, C.Kalpouzos, D.Charalambidis, and G.D.Tsakiris. Frequency-resolved photoelectron spectra of two-photon ionizsation of he by an attosecond pulse train. *New Journal of Physics*, 8(92), 2006.

[97] H.Wabnitz, Y.Mairesse, L.J.Frasinski, M.Stankiewicz, W.Boutu, P.Breger, P.Johnsson, H.Merdji, P.Monchicourt, P.Salières, K.Varjú, M.Vitteau, and B.Carré. Generation of attosecond pulses in molecular nitrogen. *European Physical Journal D*, 40:305–311, 2006.

[98] M.D.Feit, J.A.Fleck Jr., and A.Steiger. Solution of the schrödinger equation by a spectral method. *Journal of Computational Physics*, 1982.

[99] Y.Mairesse, A.de Bohan, L.J.Frasinski, H.Merdji, L.C.Dinu, P.Monchicourt, P.Breger, M.Kovačev, R.Taïeb, B.Carré, H.G.Muller, P.Agostini, and P.Salières1. Attosecond synchronization of high-harmonics soft x-rays. *Science*, 2003.

[100] Rodrigo López-Martenz, Katalin Varju, Per Johnsson, Johan Mauritsson, Yann Mairesse, Pascal Salières, Mette B. Gaarde, Kenneth J. Schafer, Anders Persson, Sune Svanberg, Claes-Göran Wahlström, and Anne L'Huillier. Amplitude and phase control of attosecond light pulses. *Physical Review Letters*, 94(033001), January 2005.

[101] P.B.Corkum, N.H.Burnett, and M.Y.Ivanov. Subfemtosecond pulses. *Optics Letters*, 1994.

[102] Markus Kitzler, Xinhua Xie, Armin Scrinzi, and Andrius Baltuska. Optical attosecond mapping by polarization selective detection. *Physical Review A*, 76(011801), 2007.

[103] Mette B. Gaarde and Kenneth J. Schafer. Generating single attosecond pulses via spatial filtering. *Optics Letters*, 31(21), 2006.

[104] N.Dudovich, O.Smirnova, J.Levesque, Y.Mairesse, M.Yu.Ivanov, D.M.Villeneuve, and P.B.Corkum. Measuring and controlling the birth of attosecond xuv pulses. *Nature Physics*, 2, November 2006.

[105] George D. Tsakiris, Klaus Eidmann, Jürgen Meyer ter Vehn, and Ferenc Krausz. Route to intense single attosecond pulses. *New Journal of Physics*, 2006.

[106] E.M.Kosik, L.Corner, A.S.Wyatt, E.Cormier, I.A.Walmsley, and L.F.DiMauro. Complete characterization of attosecond pulses. *Journal of Modern Optics*, 2005.

[107] J.Itatani, F.Quéré, G.L.Yudin, M.Y.Ivanov, F.Krausz, and P.B.Corkum. Attosecond streak camera. *Physica Review Letters*, 2002.

[108] M. Drescher, M.Hentschel, R.Kienberger, G.Tempea, C.Spielmann, G.A.Reider, P.B.Corkum, and F.Krausz. X-ray pulses approaching the attosecond frontier. *Science.*

[109] Y. Mairesse and F.Quéré. Frequency-resolved optical gating for complete reconstruction of attosecond bursts. *Physical Review A*, 2005.

[110] A.Kosuge, T.Sekikawa, X.Zhou, T.Kanai, S.Adachi, and S.Watanabe. Frequency-resolved optical gating of isolated attosecond pulses in the extreme ultraviolet. *Physical Review Letters*, 97(263901), December 2006.

[111] L.A.A.Nikolopoulos, E.P.Benin, P.Tzallas, D.Charalambidis, K.Witte, and G.D.Tsakiris. Second order autocorrelation of an xuv attosecond pulse train. *Physical Review Letters*, 94(113905), March 2005.

[112] H.G.Muller. Reconstruction of attosecond harmonic beating by interference of two-photon transitions. *Applied Physics B*, 2002.

[113] L.C.Dinu, H.G.Muller, S.Kazamias, G.Mullot, F.Augé, P.Balcou, P.M.Paul, M.Kovačev, P.Breger, and P.Agostini. Measurement of the subcycle timing of attosecond xuv bursts in high-harmonic generation. *Physical Review Letters*, 2003.

[114] Y.Mairesse, O.Gobert, P.Breger, H.Merdji, P.Meynadier, P.Monchicourt, M.Perdrix, P.Salières, and B.Carré. High harmonic xuv spectral phase interferometry for direct electric-field reconstruction. *Physical Review Letters*, 94(173903), 2005.

[115] F.Lindner, M.G.Schätzel, H.Walther, A.Baltuska, E.Goulielmakis, F.Krausz, D.B.Milosevic, D.Bauer, W.Becker, and G.G.Paulus. Attosecond double slit experiment. *Physical Review Letters*, 95(040401), July 2005.

[116] E.Gustafsson, T.Ruchon, M.Swoboda, T.Remetter, E.Pourtal, R.López-Martens, Ph.Balcou, and A.L'Huillier. Broadband attosecond pulse shaping. *Optics Letters*, 32(11), June 2007.

[117] A.Flettner, T.Pfeifer, D.Walter, C.Winterfeldt, C.Spielmann, and G.Gerber. High-harmonic generation and plasma radiation from water microdroplets. *Applied Physics B*, 77:747–751, 2003.

[118] E.A.J.Marcatili and R.A.Schmeltzer. Hollow metallic and dielectric waveguides for long distance optical transmission and lasers. *The Bell System Technical Journal*, 1964.

[119] Arvinder S. Sandhu, Etienne Gagnon, Ariel Paul, Isabell Thomann, Amy Lytle, Tracy Keep, Margaret M. Murnane, and Henry C. Kapteyn. Generation of sub-optical-cycle, carrier-envelope-phase-insensitive, extreme-uv pulses via nonlinear stabilization in a waveguide. *Physical Review A*, 74(061803), 2006.

[120] A.L.Lytle, X.Zhang, J.Peatross, M.M.Murnane, H.C.Kapteyn, and O.Cohen. Probe of high-order harmonic generation in a hollow waveguide geometry using counter-propagating light. *Physical Review Letters*, 98(123904), 2007.

[121] Stefan Eyring. Konstruktion und bau eines spektrometers für den xuv-bereich zur charakterisierung von hohen harmonischen. Diplomarbeit Universität Würzburg.

[122] Lawrence Berkeley National Laboratory. Center for x-ray optics. *http://www.cxro.lbl.gov/*, 2008.

[123] C. Winterfeldt, J. Lohbreier, T.Pfeifer, R.Spitzenpfeil, D.Walter, G.Gerber, and C.Spielmann. Adaptive spatial control of high-harmonic generation. *Ultrafast Phenomena XV - Springer Series in Chemical Physics*, 2006.

[124] J. Hartmann. Bemerkungen ber den bau und die justierung von spektrographen. *Z.Instrumentenk.*, 1900.

[125] F. Zernike. The diffraction theory of abberations. *Journal of the Optical Society of America*, 1952.

[126] M. Schottner. Algorithms for the application of hartmann-shack wavefront sensors in ophtalmology. Dissertation Universität Heidelberg, 2002.

Acknowledgements

At the end of this work I want to thank my professors and colleagues I had the pleasure to work with over the last years. Since my career took place mostly in the Experimental Physics I department at the University of Würzburg, I first want to thank all the people working there. The achievements I wrote about in this thesis would not have been possible without the strong support of the many colleagues who have become good friends of mine. Problem solving, that science very often resembles, is so much easier with a good group that co-operates and tackles almost all challenges together. Since it would be too long to list all members and friends I want to thank for helping me with my work, I want to focus on a few 'celebrities':

At first I want to thank Prof. Dr. Christian Spielmann for granting me the freedom to pursue interesting scientific tracks independently while always providing help and advise whenever needed. The very good personal atmosphere in our 'team', his highly professional expertise and the chance to work with state-of-the-art laser equipment made the time spent in his workgroup very special in the most positive sense.
I want to thank Prof. Dr. Gustav Gerber, the wise man I had the luck to experience as our chair, for his incredible dedication to support us young researchers and to provide the best possible scientific conditions. Also, I greatly appreciated all the insights he delivered when professional and personal topics were discussed in our incredible ski-seminar. Thanks for making this possible!
If there were a person I could refer to as a 'mentor and friend' it would probably be Dr. Dominik Walter who helped me with my first steps in the field of ultrashort laser pulses and with whom I share a dear friendship. I thank you for the great time we had - at the lab and elsewhere!
Speaking of good friends, of course, Stefan Eyring and Robert Spitzenpfeil also helped me a lot with every scientific or other problem and I especially want to thank Robert for his brilliant 'constructive' abilities and Stefan for the 'computer work' he is so very good at. Also my thanks go to Sebastian Jung and Nico Franke from our group for their helpfulness and nice teamwork in and out of the lab and to my office mate Florian Langhojer for being a constant source of information and entertainment (especially together with Frank Dimler).
Some of the work presented in this thesis could not have been done without my diploma students Matthias Weger, Marisa Mäder, and Christian Kern, who challenged our knowledge over and over again and who helped me to understand the difficulties that arise when one looks at ultrashort phenomena for the first time. But not only their engagement but also Ron Kemmer, Thomas Sokollik, and Frank Dimler always had time for fruitful discussions and their diploma work helped a lot to gain insight into the basic facts. I thank you for your contributions!
I do not want to forget our alumni: the inspirating Dr. Thomas Pfeifer, with whom

I could discuss almost everything and come to a useful conclusion, Dr. Carsten Winterfeldt, whose neverending patience whenever a question arose helped to get 'into the matter', and Alexander Paulus, who was the most cheerful and good-humored guy I have seen in this department.
In the background but nevertheless of great importance are our secretaries Monika Seifer, Helga Schwark, and Diep Phan who managed to protect us from too much administrative bureaucracy and thus supported our scientific work in every possible way. Another more abstract but also crucial help did often come from our machine shop that managed to construct much lab equipment in such a good way and sometimes even on a very short time scale. Without your support this work would have been much more strenuous or completely impractical.

In a way, friendship is like physics: it is not one big thing but rather a million little things. Thus, last but not least I want to dearly thank my family and Sabrina Franz for their continuous moral support and inspiration whenever experiments did not work right away or any other setback occurred.